

DIPLOMARBEIT

Selective stripping of AlCrN-coatings from WC-Co cemented carbides.

Ausgeführt zum Zwecke der Erlangung des akademischen Grades eines
Diplom-Ingenieurs (Dipl.-Ing.)

unter der Anleitung von

Associate Prof. Dipl.-Ing. Dr. techn. Andreas Limbeck
und
Univ. Prof. Dipl.-Ing. Dr. mont. Paul Heinz Mayrhofer

eingereicht an der

Technischen Universität Wien
Fakultät für Technische Chemie
Institut für Chemische Technologien und Analytik

durch

Andreas Kretschmer
Matrikelnummer 01126413
Bachgasse 31/3/10
2332 Hennersdorf

Wien, 31. Juli 2018

Associate Prof. Dipl.-Ing.
Dr. techn. Andreas Limbeck

Andreas Kretschmer, BSc.

Vorwort

Mit dem Verfassen dieser Arbeit habe ich die größte Hürde in meiner bisherigen Laufbahn bestritten und es gibt einige Personen, die mich dabei maßgeblich unterstützt haben. Das sind natürlich meine Eltern, die mich immer liebevoll unterstützt und ihre Bildung mit den Kinderschuhen mitgegeben haben. Mein Vater hat unermüdlich mit mir die Unterstufen-Mathematik durchgeschwitzt, die mich sehr gefordert hat, und nun werde ich Diplom-Ingenieur. Auch mein Bruder, immer fleißiger als ich, hat mich jederzeit unterstützt, wenn ich Hilfe brauchte. Meine Mutter hat die Familie durch tausend andere Qualitäten und nicht zuletzt das gute Essen ergänzt.

Da ich so wundervolle Eltern habe, hoffe ich selbst dazugehören zu können. Meine Tochter Livia ist vor etwas über einem Jahr zur Welt gekommen und seitdem ist es vielleicht nicht leichter geworden, aber um vieles schöner. Falls du in vielen Jahren einmal diese Zeilen liest, sollst du wissen, dass dein Lachen mir das höchste Glück schenkt. Ich darf dabei natürlich nicht meine Partnerin Rita vergessen, die mein Leben fast so sehr auf den Kopf gestellt hat wie unser kleiner Schatz. Deine Hingabe zu unserer Tochter ist über alles erhaben und ermöglicht mir noch einen relativ unkomplizierten Abschluss. Ich freue mich jeden Abend darauf, zu euch nach Hause zu kommen.

Diese Diplomarbeit wäre nicht möglich gewesen, wenn sie gar nicht erst angeboten worden wäre. Ich danke Sebastian Benedikt, Vadim Schott und Anders O. Eriksson der Firma Oerlikon Balzers für die Zusammenarbeit und dieses spannende und vielseitige Projekt. In diesem Zuge muss ich natürlich auch Andreas Limbeck erwähnen, dem ich immer für herausfordernde Aufgabenstellungen und ausgezeichnete Betreuung verbunden bin. Dem Rest der Arbeitsgruppe bin ich ebenso für die entspannte und freundliche Atmosphäre und ihre Hilfsbereitschaft verbunden, so macht forschen wirklich Spaß. Paul Heinz Mayrhofer, Vince Jaszfi und den anderen Kollegen vom Institut für Werkstoffwissenschaften und Werkstofftechnologie, die den zweiten Teil dieses Projekts durchgeführt haben, muss ich ebenso für die produktive Zusammenarbeit und spannende Entdeckungen danken. Auch viele andere Arbeitsgruppen, deren zahlreiche Nennungen ich der restlichen Diplomarbeit überlasse, haben wertvolle Erkenntnisse zu dieser Diplomarbeit beigesteuert, auch an euch ein Dankeschön.

Nicht zuletzt konnte ich mich in meiner Freizeit von klein an auf meinen eingeschworenen Freundeskreis verlassen. Wir halten immer zusammen, gemeinsam wird es nie fad.

Danke.

Wien, 31. Juli 2018

Was sagst du dazu, Sancho? Gibt es einen Zauberbann, der wahrem Mute standhielte? Das Glück können die Zauberer mir nehmen, aber Tapferkeit und Kühnheit niemals.

-Don Quijote von der Mancha (Miguel de Cervantes)

Abstract

WC-Co cemented carbides are important high performance materials used in machining and drilling. Because of the high cost of these tools the lifetime is increased by applying hard coatings such as AlCrN deposited by cathodic arc evaporation which is the investigated material system. After some use the coatings are worn-out and need to be replaced. This stripping process is done with 50 % NaOH in water at 140 °C and takes 3 h to complete. Because of the high chemical hazard risk the safety measures in industrial processing are very expensive. The goal of this thesis is to optimize this stripping process while maintaining selectivity by lowering the reaction temperature without time increase to reduce the costs. A principal condition for the hitherto used de-coating process is the sandblasting of the arcing targets with corundum prior to coating. The process creates an interlayer between substrate and coating that enhances the de-coating speed. This sandblasting was done with different corundum particle size classes, and since it is a manual step, it should also be supplanted.

Three different approaches were examined, the first was substitution of NaOH with other strong bases. Then the composition and structure of the interlayer between substrate and coating was changed either by introducing O₂ and Ar instead of N₂ into the PVD chamber, creating oxidic and metallic interlayers. Another method was evaporating an arcing target with a higher Al/Cr ratio (90/10 at% instead of 70/30 at%). Third a two step process was developed where concentrated acids weaken the coating in a kinetically controlled first step with successive stripping in NaOH.

The investigations were aided by several analytical techniques: The de-coated samples were analyzed by Scanning Electron Microscopy and Energy Dispersive X-Ray Analysis (SEM/EDX). The leaching agents were analyzed for their dissolved elements by Inductively Coupled Plasma - Optical Emission Spectroscopy (ICP-OES). Transmission Electron Microscopy (TEM), Secondary Ion Mass Spectrometry (SIMS) and X-Ray Photoelectron Spectroscopy (XPS) were used to characterize the substrate-coating interface.

The search for a better leaching agent was unsuccessful, NaOH exhibited the highest reaction rates. Successes were achieved by changing the interlayer composition, it could be proved that smaller corundum particle sizes increase the de-coating speed compared to larger ones. However sandblasting was rendered superfluous by samples with either metallic or 90/10 interlayer, since they reacted fast enough to reduce the temperature by 30 °C and still be finished within 4 h reaction time. Samples with oxidic interlayer remained inert however. By utilizing the two step process with treatment in either HCl or H₂SO₄ for 2 min at 90 °C the reaction was sped up even more, enabling a complete reaction in 3 h at only 90 °C.

Kurzzusammenfassung

WC-Co Hartmetalle sind wichtige Hochleistungsmaterialien, die in der spangebenden Formgebung eingesetzt werden. Da diese Verbundwerkstoffe sehr teuer sind, wird ihre Lebenszeit erhöht, indem harte Schichten aufgedampft werden. Die in dieser Arbeit untersuchten Materialien waren AlCrN-Schichten, hergestellt mit dem PVD-Prozess "cathodic arc evaporation". Nach einer gewissen Nutzungsdauer sind diese Schichten abgenutzt und verlieren ihre schützende Wirkung, wodurch sie ersetzt werden müssen. Das Ablösen dieser Schichten wird mit 50 % NaOH in Wasser bei 140 °C durchgeführt und benötigt 3 h. Da diese Reaktionsbedingungen sehr aggressiv sind, sind auch die Sicherheitsmaßnahmen im industriellen Prozess sehr kostspielig. Das Ziel dieser Arbeit ist, diesen Entschichtungsprozess unter Beibehaltung der Selektivität zu optimieren, indem durch Temperatursenkung die Kosten gesenkt werden, ohne die Reaktionsdauer signifikant zu erhöhen. Eine grundsätzliche Kondition für das Gelingen im bisherigen Prozess ist das Sandstrahlen der PVD-Kathoden mit Korund vor dem Beschichten. Dabei entsteht eine Zwischenschicht zwischen Substrat und Beschichtung, die das Ablösen beschleunigt. Es wurden verschiedene Korund-Korngrößen eingesetzt, da das Sandstrahlen ein manueller Prozess ist, sollte dieser wenn möglich eingespart werden.

Drei verschiedene Herangehensweisen wurden untersucht, zunächst wurde NaOH mit anderen starken Basen substituiert. Dann wurde die Zusammensetzung und Struktur der Zwischenschicht von Substrat und Beschichtung verändert, zum einen durch Einbringen von O₂ oder Ar statt N₂, womit oxidische und metallische Zwischenschichten geschaffen wurden. Eine weitere Methode war das Verdampfen von Kathoden mit höherem Al/Cr-Verhältnis (90/10 at% statt 70/30 at%). Als drittes wurde ein zweistufiger Prozess entwickelt, bei dem in einem ersten kinetisch kontrollierten Schritt die Schicht durch konzentrierte Säuren angegriffen wird. Im zweiten Schritt wurde dann wieder mit NaOH entschichtet.

Die Untersuchungen wurden unterstützt durch mehrere analytische Techniken: Die entschichteten Proben wurden mit Rasterelektronenmikroskopie und Energiedispersiver Röntgenanalytik (SEM/EDX) analysiert. Die eingesetzten Säuren und Basen wurden hinsichtlich ihrer gelösten Elemente mit Induktiv Gekoppeltem Plasma - Optischer Emissionsspektroskopie (ICP-OES) untersucht. Transmissionselektronenmikroskopie (TEM), Sekundärionenmassenspektrometrie (SIMS) und Röntgenphotoelektronenspektroskopie (XPS) wurden eingesetzt, um die Substrat-Beschichtungs-Grenzfläche zu charakterisieren.

Die Suche nach einer besseren Lauge war nicht erfolgreich, NaOH wies die höchsten Reaktionsraten auf. Erfolge wurden hingegen mit der veränderten Zwischenschichtszusammensetzung erzielt, es konnte gezeigt werden, dass kleinere Korundpartikel die Entschichtungsgeschwindigkeit im Vergleich zu größeren steigern. Allerdings konnte das Sandstrahlen überhaupt erübrigt werden, indem Proben mit metallischen oder 90/10 Zwischenschichten hergestellt wurden. Diese reagierten schnell genug, damit die Reaktionstemperatur von 140 auf 110 °C reduziert werden konnte, ohne über 4 h Reaktionszeit

hinauszukommen. Proben mit oxidischer Zwischenschicht blieben hingegen inert. Durch Einsatz des zweistufigen Prozesses mit Bad in HCl oder H₂SO₄ für 2 min bei 90 °C konnte die Reaktion noch mehr beschleunigt werden, was eine vollständige Entschichtung in 3 h bei nur 90 °C, also 50 °C weniger, ermöglichte.

Contents

1	Introduction	1
2	Theoretical Background	3
2.1	AlCrN	3
2.1.1	Structure of AlCrN	3
2.1.2	Oxidation Behaviour of AlCrN	4
2.1.3	Solubility in the System WC-Co - AlCrN	4
2.2	Cathodic Arc Evaporation	5
2.2.1	The Cathodic Arc	5
2.2.2	Macroparticles	6
2.2.3	Reactive Deposition	7
2.3	ICP-OES	7
2.3.1	Sample Introduction	8
2.3.2	Inductively Coupled Plasma	9
2.3.3	Monochromator System	10
2.3.4	CID Detector	12
2.4	Scanning Electron Microscopy	14
2.4.1	Instrumentation	14
2.4.2	Electron Interaction with the Sample	17
2.4.3	Backscattered Electrons	19
2.4.4	Secondary Electrons	21
2.4.5	Energy Dispersive X-Ray Analysis	24
2.5	Transmission Electron Microscope	31
2.6	Secondary Ion Mass Spectrometry	32
2.7	X-Ray Photoelectron Spectroscopy	33
3	Experimental	36
3.1	Used Chemicals	36
3.2	Stripping Experiment	36
3.2.1	Investigated Samples	36
3.2.2	Sample Pretreatment	37
3.2.3	Chemical Digestion	37
3.3	ICP-OES Analysis	40
3.3.1	ICP-OES Parameters	40
3.3.2	ICP-OES Measurement	40
3.4	SEM Analysis	42
3.5	Interlayer Characterization	42

4	Results	44
4.1	Interlayer Investigation	44
4.2	Investigation of Leaching Agents	49
4.2.1	Alternative Leaching Agents	52
4.2.2	ICP-OES Analysis of Leaching Agents	52
4.3	Influence of Changed Interlayer Composition	55
4.3.1	Sandblasting Particle Size	57
4.3.2	Oxidic Interlayer	57
4.3.3	Metallic Interlayer	58
4.3.4	Hexagonal Interlayer	58
4.4	Two Step Process	60
4.5	Reaction at Reduced Temperature	62
5	Conclusion	66
6	Outlook	68

1 Introduction

The development of technology, that is the foundation of modern life, is closely related to that of production resources and tools. The two main criteria in machining are precision and speed. While precision could be improved through better machines and more sensitive measurement methods, the speed was limited by the material of the cutting tools for a long time. The first carbon steels achieved cutting speeds of only a few m/min in metal cutting, the development of high speed steels (HSS) increased this value to about 20-40 m/min. A drastic improvement was achieved with the development of sintered WC-Co cemented carbides 1926, combining the hardness of WC with the plasticity of the metallic Co. This material (and other cemented carbides) can achieve cutting speeds of well beyond 100 m/min owed to its extremely high hardness and tenacity. The mechanical strength is retained even at high temperatures beyond 600 °C, where all steels fail. [1]

However, the material suffers from a few drawbacks: The manufacturing process is elaborate and costly, since WC can only be synthesized powder-metallurgically. The resources are considered strategic due to their importance in many technological applications. One issue is the world distribution of these metals. In 2017, 83 % of W was mined in China, while 58 % of Co was mined in the Democratic Republic of the Congo. In the recent past, the Chinese Government has been enacting export restrictions, leading to supply risks that endanger industries in other countries. In the Congo, the metals are usually mined without basic safety regulations by the impoverished population. Due to the increasing market of Li-ion-batteries, which contain Co, the price has risen extraordinarily in the last two years. [2–5]

Therefore increasing the lifetime and recycling rate of WC-Co-tools is essential. Since abrasion always starts at the surface of the tool different strategies have been developed to increase the surface hardness. One effective way to do so is employing hard coatings with few μm in thicknesses that protect the valuable material against abrasion and corrosion. These can be applied by Chemical Vapor Deposition (CVD) or Physical Vapor Deposition (PVD). [6]

A PVD method that was also used in this thesis is cathodic arc evaporation, one of the oldest and yet modern technologies. The earliest roots can be traced back to the eighteenth century and the study of cathodic arc processes was often closely related to discoveries in electricity. In the 1950's and 60's cathodic arc deposition emerged as industrial coating process. Its strengths are high deposition rate and flexibility of source materials and have made it one of the most common technologies for protective coatings. An early model coating which has been subject of many studies is the binary TiN. Partial substitution of the transition metal with Al leads to ternary nitrides with improved properties. AlCrN is another ternary nitride, which has become of great industrial importance due to its improved corrosion resistance at elevated temperatures. This material is also the subject of this thesis. [7, 8]

After some use, these coatings are worn-out and lose their protectiveness. By selectively recycling the coating, the lifetime of WC-Co tools can be improved even further. The established stripping process for the given sample types is done with a 50 % NaOH solution in H₂O at 140 °C, which represents both the solubility limit and boiling point of NaOH under ambient pressure [9]. This process takes 3 h and due to the chemical hazard under these conditions the safety measures are very expensive. The first goal of this thesis was therefore the optimization of this recycling process to lower temperatures to make it safer and reduce its costs. The investigated samples were provided by the Institute of Materials Science and Technology (TU Wien) [10] utilizing an Oerlikon Balzers Innova system [11]. The coatings were deposited on cemented carbide substrates for investigation of the dissolution mechanics as well as Si-wafers for analysis with Transmission Electron Microscopy.

Furthermore, the stripping process was only successful, if the evaporation targets were sandblasted with Corundum (Al₂O₃) prior to coating. For this reason the next task was to investigate the mechanism behind this behaviour and find ways to eliminate the need for sandblasting, as is it a manual step that suffers from poor reproducibility. The third goal was to explore alternative de-coating procedures that do not require NaOH at high temperatures.

To achieve these goals, different approaches were tested. First, NaOH was substituted by other bases and salts as reactant. Next, coatings with different substrate-coating interfaces were created. This was done either by altering the corundum particle size used in sandblasting, or substituting the sandblasting process by varying the conditions of the coating process through different gas atmospheres, namely O₂ and Ar, and arcing targets with an Al/Cr ratio of 90/10 at%. Last, an alternative de-coating process was investigated that included a pre-treatment of the samples in concentrated acids prior to the NaOH bath.

These investigations were aided by several analytical techniques: The de-coated samples were analyzed by Scanning Electron Microscopy and Energy Dispersive X-Ray Analysis (SEM/EDX). The leaching agents were analyzed for their dissolved elements by Inductively Coupled Plasma - Optical Emission Spectroscopy (ICP-OES). Transmission Electron Microscopy (TEM), Secondary Ion Mass Spectrometry (SIMS) and X-Ray Photoelectron Spectroscopy (XPS) were used to characterize the sample-coating interface.

2 Theoretical Background

In this chapter the theoretical background of the properties, synthesis and analysis of the AlCrN coatings will be discussed.

2.1 AlCrN

Ternary $\text{Al}_{1-x}\text{Cr}_x\text{N}$ coatings are of increasing industrial importance due to good mechanical properties and excellent corrosion and oxidation resistance at elevated temperatures. They are therefore widely used as protective coatings for forming and machining tools. The coating benefits from the fact, that both Cr and Al form protective oxides, which lead to the formation of protective mixed $\text{Al}_2\text{O}_3 + \text{Cr}_2\text{O}_3$ scales. [8]

2.1.1 Structure of AlCrN

Structurally, AlCrN can form the cubic (fcc) NaCl structure (Space Group $Fm\bar{3}m$) up to a critical AlN mole fraction of about 75 % ($x \approx 0.25$). At higher Al-contents the hexagonal (hcp) Wurtzite structure (Space Group $P6_3mc$) is obtained. Hardness and wear resistance increase with increasing Al-content within the cubic structure but drop in the hexagonal structure when the critical concentration is exceeded. The oxidation behaviour of the hcp structure is also considerably worse. So generally an Al/Cr ratio of 70/30 at% is favourable, which is the composition of the samples investigated in this study. [12]

The film synthesis via physical vapor deposition allows the formation of metastable materials far away from their thermodynamic equilibrium. The energetic particle bombardment during film growth (see 2.2 for details) creates a high defect density through point defects (interstitial atoms or vacancies) and defect clusters, which causes considerable intrinsic compressive stresses. [13] Therefore a large driving force for structural recovery exists (relaxation due to defect annihilation and atomic rearrangement) or recrystallisation, as well as phase separation into stable constituents for supersaturated films. This is also the case for AlCrN. These diffusion-driven processes are activated thermally at elevated temperatures above growth temperature, this is for instance happening during machining. This decline in the number of defects causes the hardness to decrease, as fewer defects obstruct dislocation movements. [13] In the case of metastable supersaturated films this decrease in hardness is counteracted by age-hardening phenomena during the early stages of decomposition. In the case of $\text{Al}_{1-x}\text{Cr}_x\text{N}$, this age-hardening is caused by precipitation of small incoherent hcp AlN particles. They hinder dislocation movement by forcing them to bow and curl around them (Orowan mechanism). [14–16]

For this reason, cubic Al-containing metastable transition metal nitride films generally exhibit superior thermomechanical properties as compared to their

binary counterparts. [...] The formation of hcp-AlN results in an increased hardness as long as the additional phase is small in size, evenly distributed, and of only a small volume fraction. [8]

2.1.2 Oxidation Behaviour of AlCrN

High temperature oxidation resistance is based on the possibility of the reactants, namely the metal (alloy) and the gas, to form an oxide scale that subsequently separates the reactants and thereby retards the transport of the reactants through it. Cr_2O_3 , $\alpha\text{-Al}_2\text{O}_3$ and SiO_2 scales exhibit the smallest relative growth rates [...]. In order for the oxidation reaction to proceed, either neutral atoms or ions and electrons must migrate through the growing scale. Since all metal oxides are of ionic nature, it is reasonable to consider the former case as negligible. Metal cations (M^{n+}) and electrons (e^-) diffuse outward to the scale-gas interface whereas oxygen anions and electron holes (h^+) diffuse inward toward the metal(alloy)-scale interface. [...]

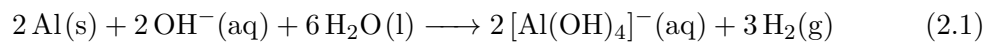
Diffusion data for single crystal Cr_2O_3 reveals that oxygen diffusion is by 3 orders of magnitude smaller than Cr, which strongly indicates predominant cation disorder and furthermore that Cr_2O_3 scales grow primarily via outward cation diffusion. [...] In polycrystalline specimens, both Al and oxygen are found to be mobile. As the oxygen transport is considerably enhanced by smaller grain size, the oxygen inward diffusion along grain boundaries seems to be the dominant transport mechanism. [...]

In principle, the combination of chromia and alumina forming metals offers the advantage of improved self-healing capacity due to the more pronounced contribution of cation outward migration as compared to pure Al_2O_3 . The latter mainly grows by anion inward diffusion [...]. Upon the formation of a crack in the scale, the cation outward migration will overgrow the crack, which is not possible in scales that grow purely by anion inward migration. Of course this is at the expense of slightly increased scale growth rates as compared to pure Al_2O_3 formation. [8]

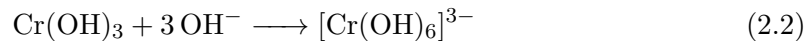
2.1.3 Solubility in the System WC-Co - AlCrN

The goal of this thesis is the selective stripping of AlCrN from WC-Co substrates. Therefore all used reactants must not attack WC or Co. Oxidizing attacks are generally not helpful, since WC-Co is reported to oxidize in O_2 -atmosphere starting at $500\text{ }^\circ\text{C}$ [17] and at rapidly increasing rates above $600\text{ }^\circ\text{C}$ [18], forming the thermodynamically stable WO_3 , while the oxidation of AlCrN is reported to only start at $900\text{ }^\circ\text{C}$ [19]. Therefore non-oxidizing environments are necessary to retain selectivity. The same can be expected for acidic attacks, since the standard electrode potential of W and Co are both below H^+ [20]. W could behave differently as it is present as carbide, but although passivation is possible as well, at least Co is likely to dissolve in acidic environments. The basis of this stripping process is the dissolution of Al since it is the major metallic component of the coating. In alkaline solutions Al reacts to a soluble tetrahydroaluminate-complex, $\text{Al}(\text{OH})_3$

therefore belongs to the amphoteric hydroxides. [21]



Cr(OH)_3 shows the same amphoteric behaviour as Al(OH)_3 . [22]



The established stripping process uses NaOH for this step. However, Equation (2.1)-(2.2) only refer to metallic Al and Cr(OH)_3 . A Diploma thesis from 2005 showed that the following chemicals are not suited for selective de-coating of CrN and AlCrN, either because they did not react at all or with the substrate as well [23]:

- Citric Acid
- K-Citrate
- NaCl
- NaOCl
- NaOH
- Deconex-mixture (cleaning agent)
- KNO_3
- KNaCO_3
- KMnO_4
- H_2SO_4

This means that Al and Cr are not soluble as nitrides even for the established process with NaOH, which explains the need for sandblasting. Thus the alteration of the chemical composition of the arcing target seems to be the key for a successful de-coating. One focus of the investigation was the effect of this changed composition.

2.2 Cathodic Arc Evaporation

Cathodic arc evaporation belongs to the physical vapor deposition (PVD) techniques featuring high deposition rates. The operating principle is a high current low voltage arc discharge between two electrodes, creating tiny, mobile spots on the cathode surface. In these "cathode spots" ions of the cathode material are produced, creating a dense plasma region with high pressure. The mechanism is still not fully understood but a widely accepted theory states that the evaporation happens by explosive electron emission. Thus the cathode (or "target") material is eroded, fully ionized and accelerated to a substrate where the ions impact and form a dense layer. On landing the ions are cooled down with great rates allowing the deposition of metastable coatings like cubic AlCrN (see subsection 2.1.1). The biggest drawback of this technique is the formation of so called macroparticles in the plasma, that are detrimental to the coatings properties. Methods to eliminate this problem are discussed in the following subsections. [7, 24]

2.2.1 The Cathodic Arc

The arc can be operated either in continuous or in pulsed mode. Continuous direct current (DC) is characterized by a high deposition rate and relatively low equipment cost and

therefore widely used. Typical arc currents are 40-150 A, the lower limit is determined by arc chopping (i.e. spontaneous extinguishing of the arc discharge). Higher currents are principally possible, leading to higher deposition rates, but equipment cost rises significantly because of cooling, increased power supply and also a higher macroparticle content in the coating.

The cathodic arc seems to be moving in a random manner around the surface. This motion is in fact a sequence of ignition and extinction of electron and plasma emission centers. Once an emission center is ignited, the conditions for electronic emission, plasma generation, and current transfer between cathode bulk and the plasma very quickly deteriorates. First the resistance of the metallic cathode bulk directly under the cathode spot is more resistive than all other areas of the cathode because it is heated up. Second the emission center builds a highly resistive barrier. In the explosive state the cathode matter transitions from solid directly into the plasma phase but with time electron emission declines but significant evaporation may still take place in the hot crater left. The rising vapor is extremely resistive and "chokes" the flow of electricity. These effects are confined very locally so that in close vicinity areas with high conductivity remain, causing the electric flow to take the path of lower resistance. Therefore a microexplosion is started at a new site.

The random "motion" of the arc can be left alone or "steered" by magnetic fields, giving it a preferred direction. Most commercial setups use a steering method because the macroparticle count is decreased due to lower plasma dwell time. The magnetic field is usually applied by the presence of permanent magnets or magnetic field coils. This apparent spot motion shows an odd behaviour: The spot tends to move in the direction of $-\mathbf{j} \times \mathbf{B}$, where \mathbf{j} is the vector of current density and \mathbf{B} is the vector of the magnetic induction. This is the opposite of the $\mathbf{j} \times \mathbf{B}$ direction one would expect if the Lorentz force was responsible for the motion. This behaviour has been the subject of intensive research and different explanations have been postulated. [7]

2.2.2 Macroparticles

Parallel to the generation of electrons and ions, macroparticles, also called "droplets", are formed. They are liquid or solid debris particles produced at cathode spots and considerably larger than the evaporated ions. Since they are generally detrimental to a coatings properties, special measures need to be taken to reduce their impact. Macroparticles are related to the formation of a pool of liquid cathode material as a result of thermal load. In a thin transition zone between the dense plasma with temperatures of a few 10 000 K and the cooler metal the cathode exists in liquid state. This liquid metal is subject to the time-varying plasma pressure, causing a complex motion. During this motion unevaporated droplets are ejected from the liquid and travel through the arcing chamber. Macroparticles show a distinct angular distribution with a emission maximum in the range of 10-30° from the cathode surface, but there is also a large fraction ejected close to the surface normal. This distribution is owed to the liquid movement. They can then bounce off several times before finally landing on a surface that can be part of the chamber wall or the substrate. Macroparticle generation can be influenced by the arc mode (continuous-pulsed, random-steered, current) but there are also filters that utilize

curved geometries. The plasma can be guided electromagnetically to a substrate that is out of line of sight with the cathode while large droplets cannot follow it. [7]

2.2.3 Reactive Deposition

By introducing different gases to the deposition chamber the composition of the coating can be changed. The gas pressure can reach from 10^{-2} mbar to atmospheric pressures. The reactive gas is activated in the plasma and reacts with the evaporated ions on their way to the substrate. For example a N_2 -atmosphere leads to the formation of nitrides like AlCrN, O_2 can be used to create oxidic layers. If no reaction is desired, inert gases like Ar can be introduced to flush out residual gases to produce metallic coatings. [7]

2.3 ICP-OES

Inductively Coupled Plasma-Optical Emission Spectroscopy (ICP-OES) is a powerful analytical technique for qualitative and quantitative measurements of elements in a sample. The instrumental setup is displayed in Figure 2.1.

The technique is based upon the spontaneous emission of photons from atoms and ions that have been excited in a RF discharge. Liquid and gas samples may be injected directly into the instrument, while solid samples require extraction or acid digestion so that the analytes will be present in a solution. The sample solution is converted to an aerosol and directed into the central channel of the plasma. At its core the inductively coupled plasma (ICP) sustains a temperature of approximately 10 000 K, so the aerosol is quickly vaporized. [25]

Consequently the vaporised matter is dissociated by additional energy input, leading to free atoms in the gaseous state.

Further collisional excitation within the plasma imparts additional energy to the atoms, promoting them to excited states. Sufficient energy is often available to convert the atoms to ions and subsequently promote the ions to excited states. Both the atomic and ionic excited state species may then relax to the ground state via the emission of a photon. These photons have characteristic energies that are determined by the quantized energy level structure for the atoms or ions. Thus the wavelength of the photons can be used to identify the elements from which they originated. The total number of photons is directly proportional to the concentration of the originating element in the sample. [25]

The large amount of energy states yields many emission lines even for a single element. This means that a sample can emit hundreds or even thousands of lines. Correct measurement requires a separation of these lines to avoid coincidences. This is done by a monochromator that disperses the photons as a function of their energy. The radiation is then guided onto a detector that measures the count rate either sequentially or simultaneously.

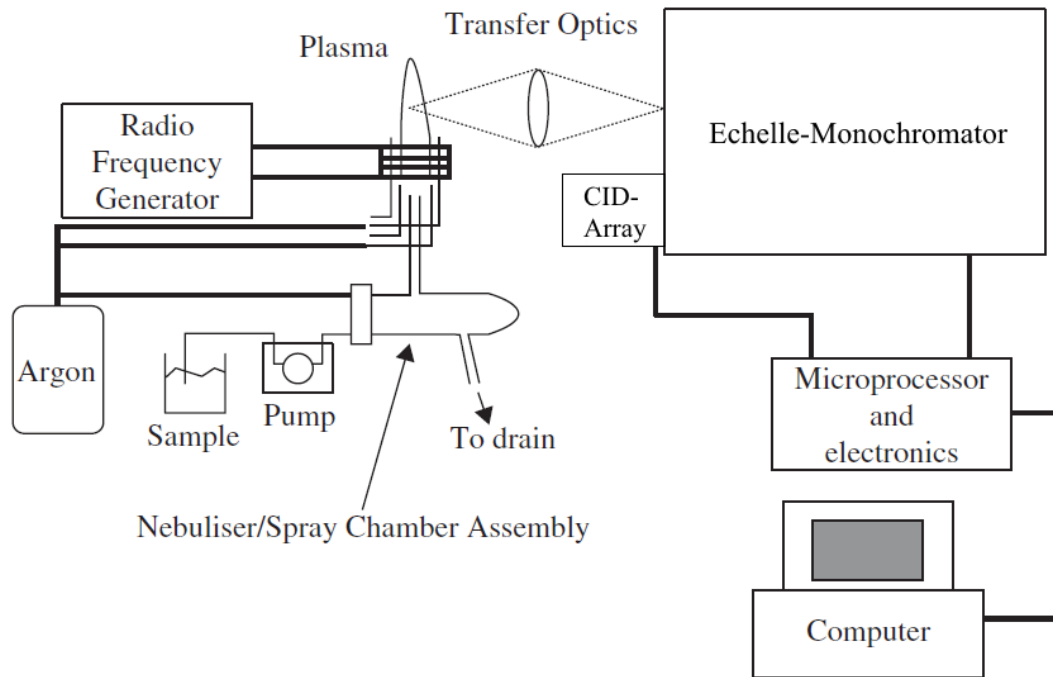


Figure 2.1: Schematic overview of the Inductively Coupled Plasma - Optical Emission Spectroscopy with a liquid sampling system, an Echelle-monochromator and a CID-Array detector. Adapted from [26]

The spectral region that is usually analysed extends from 160-800 nm, Alkali elements generally emit at higher wavelengths above 500 nm whereas halogen lines lie below 190 nm. There are several criteria for selecting wavelengths: The wavelength needs to be accessible both by the dispersive system and the detector, it must exhibit signal levels appropriate to the elements concentration and it must be free from spectral interference. The number of elements that can be analysed with ICP-OES is often more than 70 out of the 92 naturally occurring elements. Those that cannot be analysed are usually trace contaminants of the Ar gas (C from CO₂), constituents of the solvent (C, O, H), contaminants from the atmosphere (N, O, H, C) and short lived radioactive elements. Elements with high excitation energies like the halogens can be measured but with poor sensitivity. The limit of detection (LOD) is generally in the µg/L or parts-per-billion (ppb) region. The LOD is defined as analyte concentration that produces a signal equivalent to three times the standard deviation of a blank. [25]

2.3.1 Sample Introduction

Inductively coupled plasmas can be used with different methods of sample introductions, either in solid, liquid or gaseous state. Since in this thesis only liquids were analysed, this chapter is dedicated to liquid sample introduction.

Generally all samples are transported into the plasma by an Ar-gas flow, be it as an

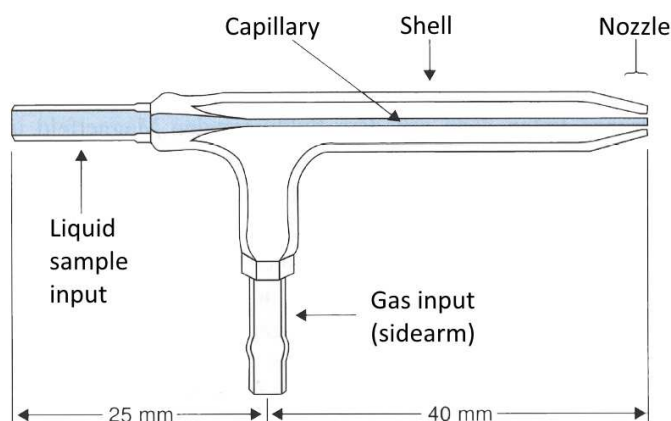


Figure 2.2: Schematic of a Meinhard-nebuliser. Adapted from [27]

aerosol, a vapor or fine particles. Liquid samples usually consist of a great majority of solvent in which only small amounts or even traces of analytes are dissolved. The ICP runs at a limited power, meaning that the evaporation of large amounts of solvent would cool the plasma down or even extinguish it, leaving too little energy for analytes to be evaporated, atomized and excited. Therefore liquids have to be pre-treated to reduce the amount of solvent. This is done by nebulising and separation in a cyclone spray-chamber. In Figure 2.2 a schematic of the most common nebuliser type, the Meinhard-nebuliser is displayed. The liquid sample flows in from the side through a capillary while a carrier gas flows concentrically around this capillary, creating a low pressure region in front of the nozzle. The pressure difference pulls the liquid out of the capillary where it is dispersed into a fine vapor by the high velocity gas stream. This vapor consists of fine droplets of varying size. The larger fractions of this vapor still carry too much solvent and have to be separated from the rest. This is done in the spray-chamber (see Figure 2.3). The gas stream carrying the vapor is introduced in a tangential direction, the carrier gas then flows in a spiralling motion to the top and into the plasma torch. Small droplets with particle sizes $\leq 1 \mu\text{m}$ can follow the gas stream and are introduced into the plasma, while larger droplets possess too high inertia, consequently they impact the chamber wall and exit on the bottom into the waste. The sample introduction efficiency is usually only about 1-2%. [26, 27]

2.3.2 Inductively Coupled Plasma

In Figure 2.4 the schematic of an ICP-torch can be seen. The torch consists of three concentric quartz tubes through which Ar is flowing. The outermost tube is about 2.5 cm in diameter and contains the coolant gas. In it a tangential Ar flow of typically $11\text{-}14 \text{ Lmin}^{-1}$ cools the outermost tube to isolate it thermally from the excessive heat of the plasma. The tangential flow also centres the plasma radially. The second tube conveys the auxiliary gas with a flow rate of $0.5\text{-}2 \text{ Lmin}^{-1}$. Its purpose is to lift the plasma away from the ends of the auxiliary and injector tubes, preventing them from melting. In the innermost tube the nebuliser gas with the sample flows with a rate of $1.5\text{-}1.5 \text{ Lmin}^{-1}$. In the upper part



Figure 2.3: A cyclone spray chamber. The vapor enters from the side, the top exit leads to the torch, the bottom exit into the waste. [26]

of the tube a water-cooled coil is situated that is powered by a radio-frequency generator. The power required for optical emission spectroscopy lies in the range of 600-1800 W, but typical operational powers for aqueous solutions are 950-1400 W. Two frequencies are in use, 27.12 MHz and 40.68 MHz, though nowadays most instruments use the latter frequency because it offers improved coupling efficiency. An alternating current oscillates inside the coil at a rate corresponding to the frequency of the radio-frequency generator. The ignition takes place by a spark from a Tesla coil. The created ions and electrons are then influenced by the fluctuating magnetic field of the coils, forcing them on closed circular paths (see the magnetic field lines in Figure 2.4) in an oscillating manner. Through this motion the charged particles collide with other atoms and create even more ions and electrons in a chain reaction. The collisions cause the Ohmic heating of the plasma to temperatures of up to 10 000 K in its core. Adding energy to the plasma by radio-frequency induced collisions is called inductive coupling thus naming the phenomenon "inductively coupled plasma". The plasma plume cools off with increasing distance to its core, dividing it into zones with different temperatures. Measurement can be done in axial or radial mode. For axial alignment the detection system lies on the direct path of the gas flow, so that emission from the whole plasma is recorded, providing the highest possible sensitivity. In radial mode the detection system is rotated by 90° to the side, allowing the detection from a certain plasma region. The benefit of this alignment is the reduced interference from recombining species that form in cooler regions of the plasma. [25–27]

2.3.3 Monochromator System

Since detectors such as photomultipliers (PMT) and charge injection devices (CID) cannot distinguish photons of different energies and wavelengths, they have to be separated beforehand. This is task of optical devices called monochromators. In principle they consist of the following parts: Entrance slit, a collimator, creating a parallel beam, a

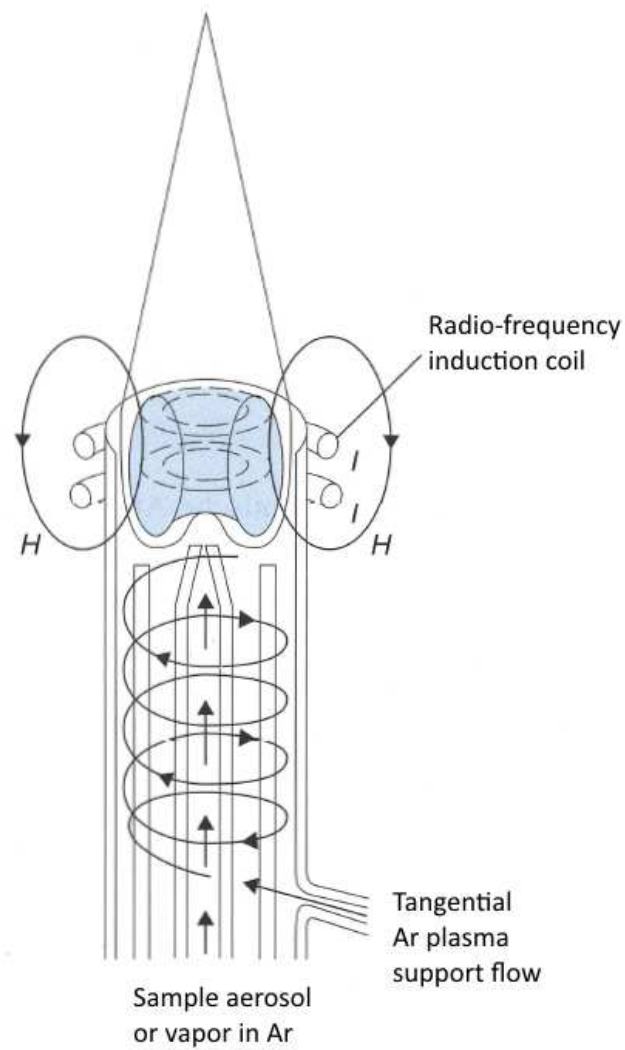


Figure 2.4: Schematic of an ICP-torch. H signifies the magnetic field lines. Adapted from [27]

dispersive element, a focussing element and an exit slit in its focal plane. The exit slit can also be replaced by a detector array that detects different wavelengths laterally resolved at the same time. There are two different types of dispersive elements: prisms and gratings. The dispersion of a prism is based on the different optical refraction that each wavelength suffers on transition from gas to the prism and back. Shorter wavelengths (higher energy) are deviated stronger than longer wavelengths, creating angle dependent dispersion. A dispersion grating consists of closely spaced parallel surfaces that reflect light. The schematic can be seen in Figure 2.5. Since the incident light is reflected on a multitude of parallel surfaces, the light is only diffracted in directions of constructive interference. The condition can be expressed mathematically:

$$\mathbf{n}\lambda = d(\sin \alpha + \sin \beta) \quad (2.3)$$

where \mathbf{n} is the diffraction order, λ the wavelength, d the gratings spacing, α and β the angles of incident light and diffracted light to the gratings normal. $\mathbf{n}\lambda$ is the optical path difference of rays reflected on separate surfaces. Since all energies land with the same incident angle α , constructive interference for different λ happens in different diffraction angles β , resulting in optical dispersion.

Since optical emission spectroscopy yields very high amounts of elemental lines, a high dispersion is necessary to avoid interferences. A device that achieves one of the highest dispersions is the so called Echelle monochromator. It uses two dispersive elements in succession: First a grating with a very high dispersion and resolution, separating the incident light in many different diffraction orders. Since these orders are partly overlapping, they have to be separated by the second dispersive element, an orthogonally aligned prism. This creates a two-dimensional spectrum that can be projected onto a charge injection device (CID)-Array, allowing short analysis times by simultaneous illumination of the whole spectrum. [27]

2.3.4 CID Detector

In Figure 2.7 the work cycle of the charge induced device (CID) element is displayed. The photo-active material of such a device consists of n-doped Si on a substrate and a thin isolator layer on top. Two electrodes above this layer form one pixel. When the n-doped Si is illuminated with photons, Electrons from the valence band are elevated into the conduction band, creating mobile electrons (e^-) and holes (h^+) in the semiconductor. By applying negative voltages to both capacitors, potential wells are generated below the surface (**a**) that attract the holes. Since the potential of the right electrode is lower, all holes gather on its side. The amount of accumulated charges is measured in **b-c**. In **b** the potential difference of the left capacitor (U_1) is measured after switching off the applied voltage. In **c** the charges are moved from the right to the left potential well by reversing the polarity of the right capacitor. Then the potential difference U_2 on the left capacitor is measured again. The accumulated charge is quantified by the difference $U_1 - U_2$. In **d** The CID is returned into its original state by applying positive voltage to both electrodes, pressing the holes into the substrate. Alternatively the detector can be transformed into state **a** again without destroying the accumulated charges. This

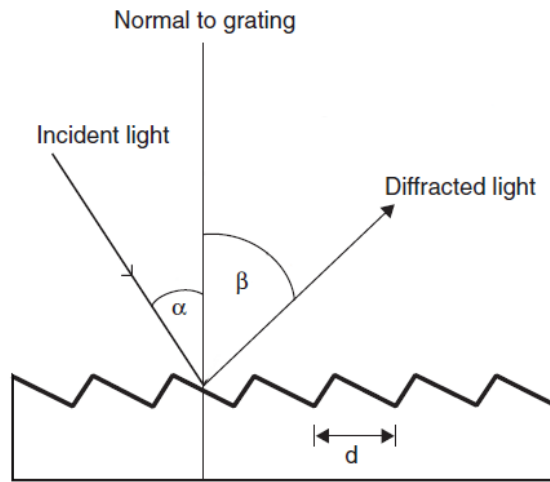


Figure 2.5: Schematic of an optical grating. α and β are the angles of incident and diffracted light to the gratings perpendicular, d is the gratings spacing. Adapted from [26]

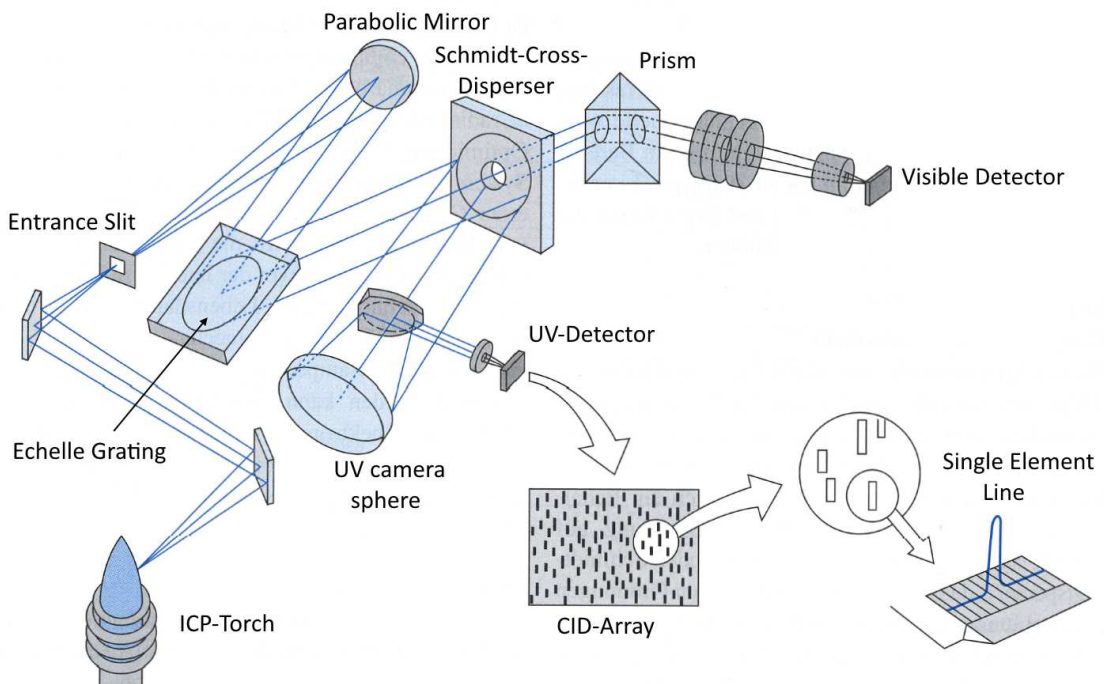


Figure 2.6: Schematic of an Echelle monochromator. In this setup a Schmidt-Cross-disperser replaces the prism for UV light to improve UV-transmission. Adapted from [27]

non-destructive readout mode is a great advantage of CID over charge coupled devices (CCD) because measurements can be done while accumulating charges. [27]

2.4 Scanning Electron Microscopy

The scanning electron microscope (SEM) is an instrument that creates magnified images which reveal microscopic-scale information on the size, shape, composition, crystallography, and other physical and chemical properties of a specimen. [...] The basic operating principle of the SEM involves the creation of a finely focused beam of energetic electrons by means of emission from an electron source. The energy of the electrons in this beam, E_0 , is typically selected in the range from $E_0 = 0.1$ to 30 keV. After emission from the source and acceleration to high energy, the electron beam is modified by apertures, magnetic and/or electrostatic lenses, and electromagnetic coils which act to successively reduce the beam diameter and to scan the focused beam in a raster ($x - y$) pattern to place it sequentially at a series of closely spaced but discrete locations on the specimen. At each one of these discrete locations in the scan pattern, the interaction of the electron beam with the specimen produces two outgoing electron products: backscattered electrons (BSE), which are beam electrons that emerge from the specimen with a large fraction of their incident energy intact after experiencing scattering and deflection by the electric fields of the atoms in the sample; and secondary electrons (SE), which are electrons that escape the specimen surface after beam electrons have ejected them from atoms in the sample. Even though the beam electrons are typically at high energy, these secondary electrons experience low kinetic energy transfer and subsequently escape the specimen surface with very low kinetic energies, in the range 0-50 eV, with the majority below 5 eV in energy. At each beam location, these outgoing electron signals are measured using one or more electron detectors, usually an Everhart-Thornley "secondary electron" detector (which is actually sensitive to both SEs and BSEs) and a "dedicated backscattered electron detector" that is insensitive to SEs. For each of these detectors, the signal measured at each individual raster scan location on the sample is digitized and recorded into computer memory, and is subsequently used to determine the gray level at the corresponding $X - Y$ location of a computer display screen, forming a single picture element (or pixel). [28]

2.4.1 Instrumentation

In Figure 2.8 the cross section of a SEM with the electron-optical column and the specimen chamber is displayed. At the top of the column the electron gun is situated, which emits the electrons either thermoionically from a W- or LaB₆-filament or from a field emission gun using cold-cathodic emission. The instrument used in this thesis, a FEI Quanta 200, featured a W-filament. W-filaments offer reliability and low cost of use but reach poorer resolution than the other emitter types. The emitted electrons are accelerated with a high voltage (see section 2.4) and pass a Wehnelt-cylinder. A condenser lens consisting of

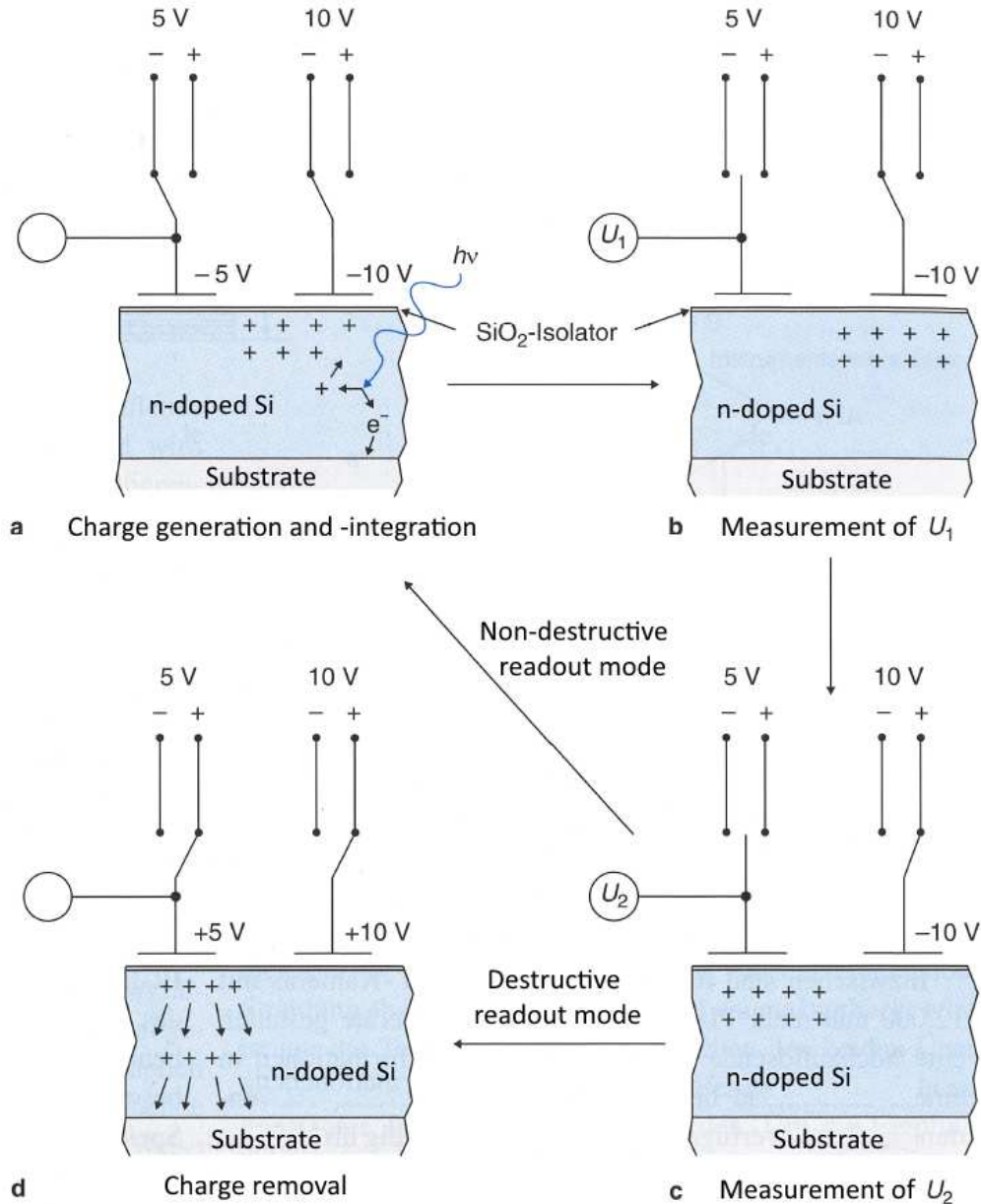


Figure 2.7: Work cycle of a charge induced device. **a** Generation and integration of charges by absorption of photons **b** Measurement of U_1 **c** Measurement of U_2 **d** Charge removal. State **c** can be transformed into state **a** or **d**, allowing destructive or non-destructive measurement. Adapted from [27]

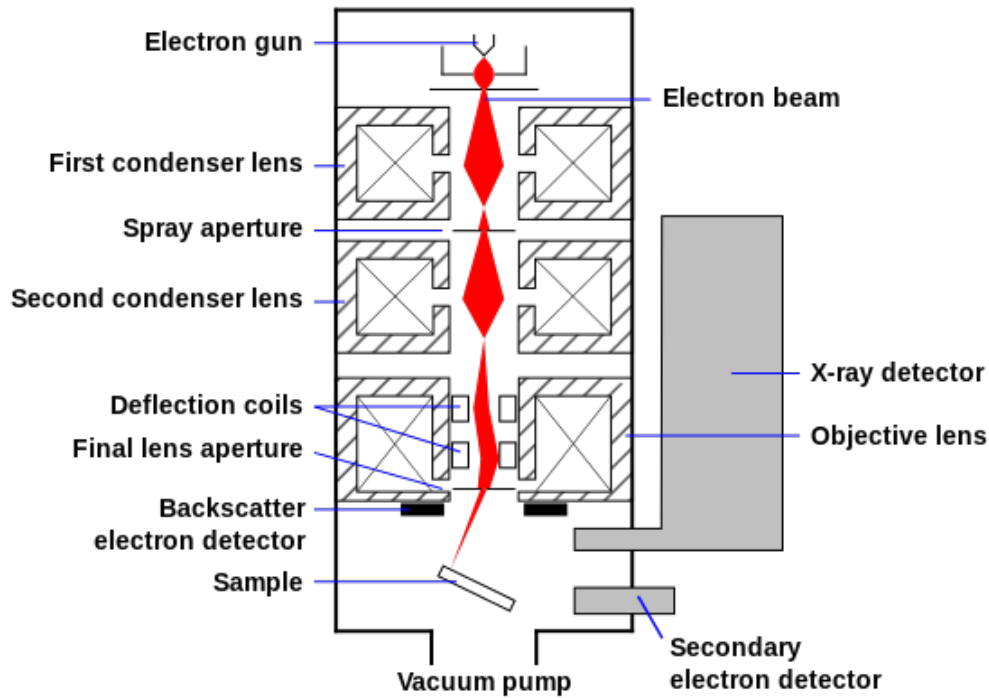


Figure 2.8: Schematic overview of the Scanning Electron Microscope. [30]

copper windings subjected to a current narrows the beam diameter to the desired size. In Figure 2.8 you can see a gap in the lens casing facing the electron beam. The magnetic field inside the gap can be resolved into two components: one along the direction of the optical axis, and one perpendicular to it. An electron entering the lens interacts with both components. The Lorentz-force

$$\mathbf{F} = q\mathbf{E} + q\mathbf{v} \times \mathbf{B} \quad (2.4)$$

describes the interaction, where q is the electrons charge, \mathbf{v} their velocity and \mathbf{E} and \mathbf{B} the electric and magnetic field. The component perpendicular to the optical axis produces a rotational force. This rotational force then interacts with the magnetic component parallel to the optical axis, producing an overall radial force. This radial force causes the electron to curve towards the optical axis in a spiralling motion and to cross it providing the lens with focusing capabilities. A spray aperture blocks off poorly collimated parts of the beam. The beam is then either guided through a second condenser lens or to the objective lens. At the bottom of the column the deflection coils raster the electron beam in the x and y axes on the sample, which is situated in the specimen chamber on a moveable stage. The SEs, BSEs and X-rays gained through the interaction of the electron beam with the sample are captured with their respective detectors. The signals are then processed by a computer to generate an image. [28, 29]

In a conventional-vacuum SEM, the electron-optical column and the specimen chamber must operate under high vacuum conditions ($<10^{-4}$ Pa) to

minimize the unwanted scattering that beam electrons as well as the BSEs and SEs would suffer by encountering atmospheric gases. [28]

Insulating samples cannot conduct the electron current to the grounding and develop surface electrical charges that distort the incoming electron beam. In these cases conductive coatings need to be applied. Imaging in low vacuum modes is also possible, however this was not necessary for the samples studied in this thesis.

The effective position of a detector is specified by two angles. The elevation angle, designated Ψ , is the angle above a horizontal plane perpendicular to the beam axis and the vector that joins the center of the detector to the beam impact position on the specimen [...]. The azimuthal angle, ζ , of the detector is the rotational angle around the beam to the detector line, measured relative to some arbitrary but fixed reference, such as the front face of the specimen chamber [...]. When a SEM image is created, it is critical for the user to understand the relative position of the detector in the scanned image, as given by the azimuthal angle, since the illumination of the image will apparently come from the detector. [...]

The effective size of the detector with an active area A placed at a distance r from the beam impact point on the specimen is given by the solid angle, Ω , which is defined as [28]

$$\Omega = A/r^2 \quad (2.5)$$

Since Ω is strongly dependant on the distance of the detector from the beam impact location on the specimen, detector placement is always a compromise between high collection efficiency and manoeuvring space for large samples, especially when tilted. This overall geometric efficiency, ϵ , can be expressed as the solid angle of the detector compared to the solid angle of the hemisphere (2π sr) into which all electrons leaving a thick target are emitted: [28]

$$\epsilon = \Omega/2\pi \quad (2.6)$$

2.4.2 Electron Interaction with the Sample

Since the microscope is operated in high vacuum the electrons are statistically unlikely to encounter residual gas atoms on their flight path. At the sample surface the atom density rises abruptly to the very high densities of the solid. This causes a series of interactions that can be summarized as scattering events. These can be classified into inelastic scattering (energy loss) and elastic scattering (no energy loss).

Inelastic scattering refers to physical processes that transfer energy from the electron onto the sample atoms. The interaction can happen with loosely-bound valence electrons and tightly bound inner-shell electrons. In the former case, secondary electrons with energies of a few eV are ejected. In the latter case the ejection of electrons with energies of hundreds to thousands of eV leads to the emission of characteristic X-rays by relaxation of electrons in upper shells. The difference in binding energy of the two states is emitted as a photon with a wavelength that is characteristic of the element. Additionally the deceleration of the primary electrons in the electrical field of the atoms produces the so

called "Bremsstrahlung", an unspecific continuum over the whole energy range up to the beam's landing energy E_0 . Additionally waves in the free electron gas of conducting metal solids (plasmons) and heating of the sample can be generated.

While the inelastic scattering causes electrons to deviate only slightly from their current path, the energy loss sets a limit on how far the beam can travel in the sample before it is absorbed. Bethe [31] was able to estimate the rate of energy loss by the "continuous energy loss approximation":

$$dE/ds = -7.85(Z\rho/AE) \ln(1.166E/J) \quad (2.7)$$

where E is the beam energy (keV), Z is the atomic number, ρ is the density (g/cm³), A is the atomic weight (g/mol) and J is the "mean ionization potential" (keV) given by

$$J = (9.76Z + 58.5Z^{-0.19}) \times 10^{-3} \quad (2.8)$$

Thus we can state, that the so called "Bethe range" decreases with increasing atomic number and density of the target while it increases with increasing beam energy.

Elastic scattering occurs when the beam electrons are deflected by the electrical field of the sample atoms.

Simultaneously with inelastic scattering, "elastic scattering" events occur when the beam electron is deflected by the electrical field of an atom (the positive nuclear charge as partially shielded by the negative charge of the atom's orbital electrons), causing the beam electron to deviate from its previous path onto a new trajectory [...]. The probability of elastic scattering depends strongly on the nuclear charge (atomic number Z) and the energy of the electron, E (keV) and is expressed mathematically as a cross section, Q :

$$Q_{elastic(>\phi_0)} = 1.62 \times 10^{-20} (Z^2/E^2) \cot^2(\phi_0/2) \quad (2.9)$$

where ϕ_0 is a threshold elastic scattering angle, for example, 2°. Despite the angular deviation, the beam electron energy is effectively unchanged in energy. While the average elastic scattering event causes an angular change of only a few degrees, deviations up to 180° are possible in a single elastic scattering event. Elastic scattering causes beam electrons to deviate out of the narrow angular range of incident trajectories defined by the convergence of the incident beam as controlled by the electron optics.

The frequency of elastic scattering events can be calculated from Equation (2.9), leading to the mean free path :

$$\lambda_{elastic} = 10^7 A / [N_0 \rho Q_{elastic(>\phi_0)}] \quad (2.10)$$

where $\lambda_{elastic}$ is the mean free path (nm), A is the atomic weight (g/mol), N_0 is Avogadro's number (atoms/mol), and ρ is the density (g/cm³). While inelastic scattering limits the total distance travelled by the beam electron to ranges of about 1-5 μm , $\lambda_{elastic}$ is in the order of a few nm. Thus elastic scattering is likely to occur hundreds or thousands

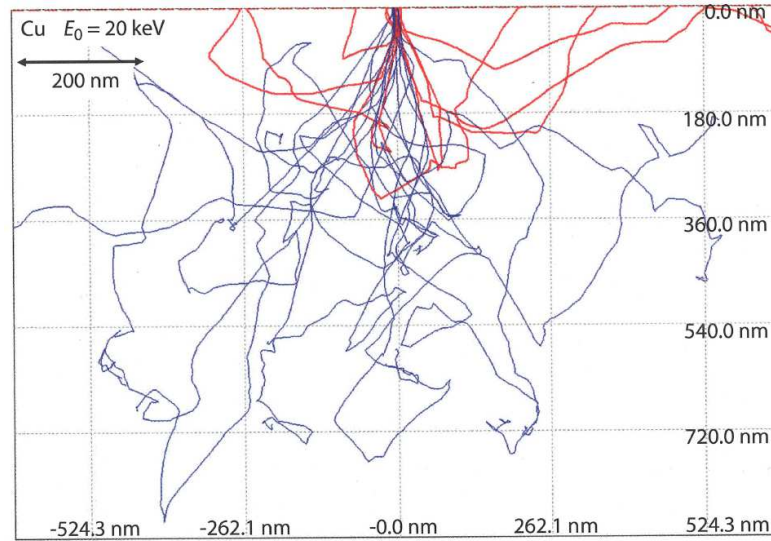


Figure 2.9: Monte Carlo simulation of 25 trajectories in Cu. The blue trajectories are absorbed by the material while the red trajectories leave the sample as backscattered electrons. [28]

of times before the electron is absorbed. The combination of range limit by inelastic scattering and path deviation by elastic scattering leads to a so called interaction volume. Because of the randomness of the scattering events individual trajectories can be calculated with the "Monte Carlo electron trajectory simulation". Such trajectories are displayed in Figure 2.9. The signals collected by the detectors always come from this interaction volume. Therefore the achievable resolution of a SEM is not solely dependent on the beam diameter and energy E_0 but highly influenced by the samples properties such as the mean atomic number Z , the density ρ and its electrical conductivity. This resolution limit is circumvented in Transmission electron microscopy where samples are thinned to less than 100 nm thickness, thus preventing the evolution of the plume-shaped interaction volume. [28]

2.4.3 Backscattered Electrons

A fraction of the incident electrons undergo sufficient scattering to reverse their initial direction causing them to return to the sample surface and to leave it. These electrons are called backscattered electrons (BSE) and contain information about specimen composition, topography, mass thickness and crystallography.

Backscattered electrons are quantified with the "backscattered electron coefficient" η , defined as

$$\eta = N_{BSE}/N_B \quad (2.11)$$

where N_B is the number of beam electrons that enter the specimen and N_{BSE} is the number of those electrons that subsequently emerge as backscattered electrons.

Experimental measurements showed that η increases monotonic with increasing Z . Reuter [32] developed a mathematical fit for 20 keV data:

$$\eta = -0.0254 + 0.016Z - 1.86 \times 10^{-4}Z^2 + 8.3 \times 10^{-7}Z^3 \quad (2.12)$$

This fit is displayed in Figure 2.10. The monotonic behaviour of η vs. Z is the basis of the so-called "atomic number contrast" or abbreviated " Z -contrast". When a BSE image from a flat specimen is recorded, the local differences in composition yield different BSE intensities. Translated into a grey-scale the chemical composition in this image can be easily interpreted.

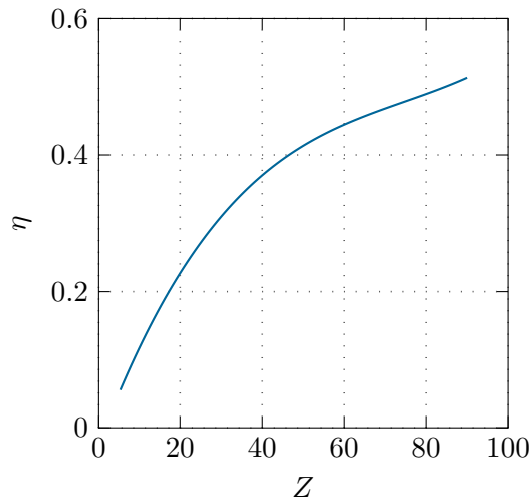


Figure 2.10: Fit of Backscatter coefficient η as a function of atomic number Z (Equation (2.12)). [32]

When measuring with a surface tilt θ the backscattering is increased in a forward direction. Since the backscatter coefficient η rises with increasing surface tilt θ , the relative number of backscattered electrons depend on local surface inclinations. This can be used to image the topographic contrast of the sample. A higher inclination of the surface to the incident beam leads to a higher signal, making the surface appear bright.

Elastic scattering causes the incident electrons to spread significantly in the sample, increasing their lateral distribution by more than an order-of-magnitude as can be seen in Figure 2.9. Heavier elements that are strong scatterers suffer a lower relative spread compared to lighter elements. The impact is always significant however. This influences the spatial resolution of BSE images heavily. Thus, images with the highest spatial resolution can be obtained with secondary electrons.

The FEI Quanta 200 used in this thesis features a Semiconductor BSE Detector. A schematic can be seen in Figure 2.11. The detector is mounted directly above the sample to obtain a large collection area. When highly energetic BSE impact on the detector, they transfer their energy and elevate loosely bound valence shell electrons of the semiconductor from the valence band into the conduction band. This creates mobile charges in the conduction band (e^-) and leaves holes in the valence band (h^+). These charges can

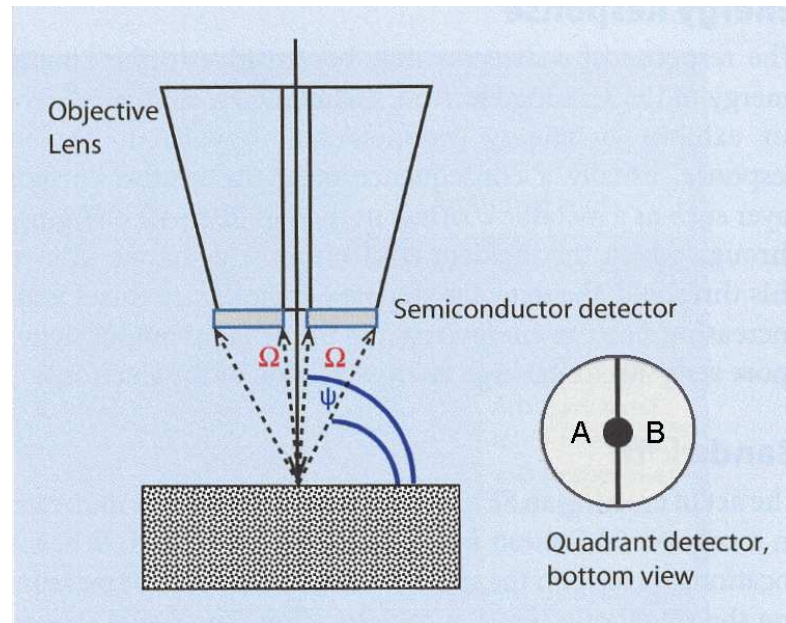


Figure 2.11: BSE detector schematic. The dotted lines mark the solid angle Ω , the blue lines the elevation angle Ψ . Adapted from [28]

move freely according to an applied bias voltage. The free electrons are collected at a surface electrode and measured. In Si the excitation requires 3.6 eV, so a BSE with 15 keV generates about 4000 free electrons. The energy threshold of the semiconductor BSE detector lies in the range of 1-3 keV, making it inaccessible for low energy secondary electrons. Above the threshold the response rises linearly with increasing electron energy, rendering the detector especially sensitive to the high energy fraction of BSE. The detector utilizes a segmented design, where the signal of both segments can either be added to gain images with elemental contrast or subtracted to highlight topographic features. [28]

2.4.4 Secondary Electrons

Secondary Electrons (SE) are created when inelastic scattering of beam electrons ejects weakly bound valence electrons from the sample.

They are quantified by the parameter δ , the secondary electron coefficient, which is the ratio of secondary electrons emitted from the specimen, N_{SE} , to the number of incident beam (primary) electrons, N_B :

$$\delta = N_{SE}/N_B \quad (2.13)$$

The most important characteristic of SE is their extremely low kinetic energy. Because of the large mismatch in relative velocities between the primary beam electron (incident energy 1-30 keV) and the weakly bound atomic electrons (1-15 eV ionization energy), the transfer of kinetic energy from the primary electron to the SE is relatively small, and as a result, the SE are ejected

with low kinetic energy. After ejection, the SE must propagate through the specimen while undergoing inelastic scattering, which further decreases their kinetic energy. SE are generated along the complete trajectory of the beam electron within the specimen, but only a very small fraction of SE reach the surface with sufficient kinetic energy to exceed the surface energy barrier and escape. The energy spectrum of the secondary electrons that escape is peaked at only a few eV, as shown in Figure 2.12 [...]. Above this peak, the intensity falls rapidly at higher kinetic energy. [...]

The kinetic energy of SE is so low that it has a strong influence on the depth from which SE can escape from the specimen. While some inelastic scattering processes are absent because of the low kinetic energy of SE, nevertheless SE suffer rapid energy loss with distance travelled, limiting the range of an SE to a few nanometers rather than the hundreds to thousands of nanometers for the energetic beam electrons and BSE. Thus, although SE are generated along the entire trajectory of a beam electron scattering in the target, only those SE generated close to a surface have a significant chance to escape. The probability of escape depends on the initial kinetic energy, the depth of generation, and the nature of the host material. Since there is a spectrum of initial kinetic energies, each energy represents a different escape probability and depth sensitivity. This complex behaviour is difficult to measure directly, and instead researchers have made use of the Monte Carlo simulation to characterize the escape depth.

The dependency of the secondary electron coefficient as a function of atomic number yields seemingly chaotic and inconsistent behaviour when comparing different sources. Oddly, these measurements may still be "correct", meaning measured in a valid, reproducible way. The reason behind this is that a representative measurement of properties from electrons generated within a very shallow area below the surface is hardly possible. Since all surfaces measured in normal electron microscopes reside at pressures of as low as 10^{-4} Pa they are always covered with complex mixtures of oxygen, water, hydrocarbons and other contaminants. Therefore measurements from such surfaces will always result in values of δ that are different from an ideal clean surface as it does not exist under normal conditions.

Thus, while compositionally dependent secondary electron signals may be occasionally observed, they are generally not predictable and reproducible, which is the critical basis for establishing a useful contrast mechanism such as that found for backscattered electrons as a function of atomic number.

Instead, SE show a significant contrast behaviour regarding specimen tilt. When measuring a sample with a tilt angle $\theta \neq 0$, a monotonic increase with tilt can be observed. This behaviour can be explained geometrically as shown in Figure 2.13. As the primary beam enters the specimen the SE production remains effectively constant for the shallow depth from which SE can leave the specimen because the primary electrons scatter insufficiently on this short path to modify their energies and trajectories. The length of the primary beam path within the depth of escape, s_{esc} , increases as the secant of the tilt angle. Rough surfaces will therefore look brighter at the edges and darker at

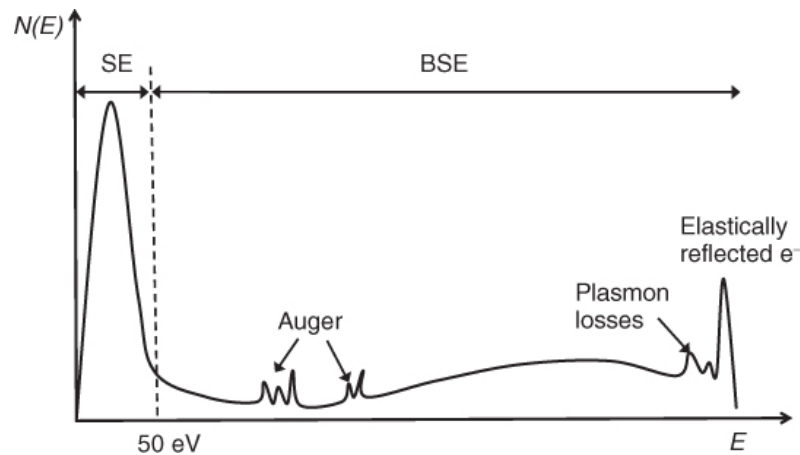


Figure 2.12: Energy distribution of emitted electrons. In a SEM the SE and BSE fraction can be measured. [33]

surfaces perpendicular to the primary beam. This plays an important role in producing topographic contrast that reveals the shape of an object.

Secondary electrons are measured with an Everhart-Thornley detector. A schematic can be seen in Figure 2.14.

Everhart and Thornley (1957) solved the problem of detecting very low energy electrons by using a scintillator with a thin metal coating to which a large positive potential, 10 kV or higher, is applied. This post-specimen acceleration of the secondary electrons raises their kinetic energy to a sufficient level to cause scintillation in an appropriate material (typically plastic or glass doped with an optically active compound) after penetrating through the thin metallization layer that is applied to discharge the insulating scintillator. To protect the primary electron beam from any degradation due to encountering this large positive potential asymmetrically placed in the specimen chamber, the scintillator is surrounded by an electrically isolated "Faraday cage" to which is applied a modest positive potential of a few hundred volts [...]. The primary beam is negligibly affected by exposure to this much lower potential, but the secondary electrons can still be collected with great efficiency to the vicinity of the Faraday cage, where they are then accelerated by the much higher positive potential applied to the scintillator.

While the E-T detector does indeed detect the secondary electrons emitted by the sample, the nature of the total collected signal is actually quite complicated because of the different sources of secondary electrons [...].

In Figure 2.15 the different SE sources are displayed. SE_1 generated within the landing area of the primary beam on the specimen cannot be distinguished from SE_2 created by exiting BSE, since they are produced spatially close, have the same energy and the same angular distribution. Moreover BSE are so highly energetic that their trajectory is not influenced by the low Faraday cage potential. Eventually they hit the pole piece, stage

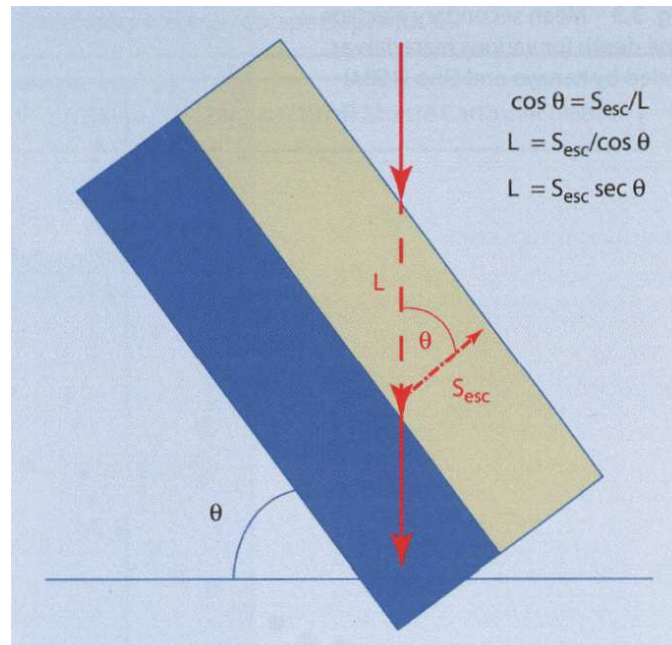


Figure 2.13: Geometric explanation of the secondary electron yield increase with increasing tilt angle θ . The yellow area signifies the region within the escape depth s_{esc} . [28]

components or other parts of the specimen chamber where they generate SE_3 as well. These are located several cm away from the beam impact, but they are still collected with a high efficiency by the Faraday cage potential. Since the production of these SE depend on BSE, they carry BSE information ("indirect BSE"). Additionally BSE emitted into the solid angle defined by the E-T scintillator disk are detected as well ("direct BSE"). Thus the recorded signal represents a mixture of sources which is of high importance for the "secondary electron image". [28]

2.4.5 Energy Dispersive X-Ray Analysis

Apart from SE and BSE, another type of response can be measured with a SEM: X-Ray emission. When a beam electron with higher energy than the "critical ionization energy" E_c scatters inelastically with a sample electron, "characteristic" X-rays can be emitted. These can be used to identify the atomic species present in the sample. Simultaneously, decelerating beam electrons generate Bremsstrahlung which creates a continuous spectral background, whose energies fill the range from the lower limit up to E_0 . X-rays are generated throughout a large fraction of the interaction volume.

The process of generating X-rays is illustrated for a carbon atom in Figure 2.16. In the initial ground state, the carbon atom has two electrons in the K-shell bound to the nucleus of the atom with an ionization energy E_c [...] of 284 eV and four electrons in the L-shell, two each in the L_1 and L_2 subshells

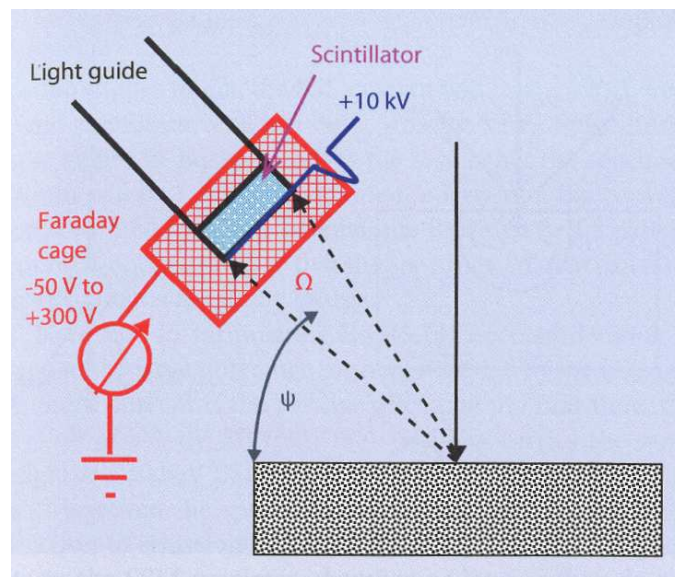


Figure 2.14: ETD-Detector schematic. The dotted lines mark the solid angle Ω , the blue line the elevation angle Ψ . [28]

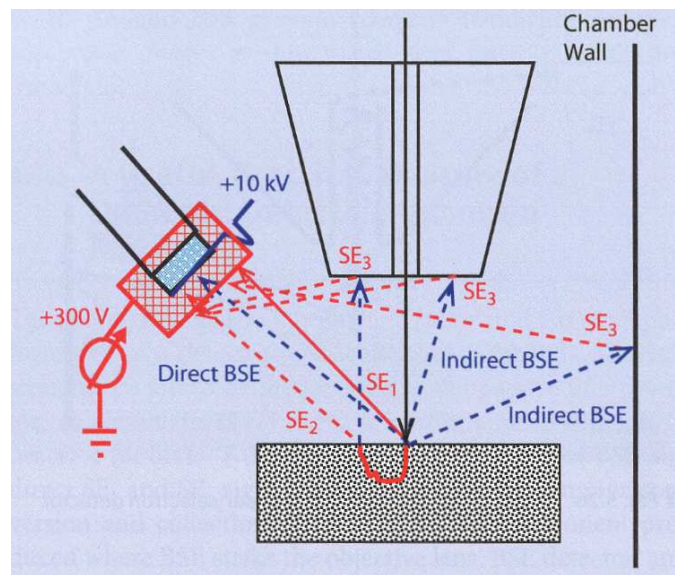


Figure 2.15: Different sources of SE, that contribute to the ETD-image. Red lines represent SE-trajectories, blue lines BSE-trajectories. SE_1 are generated directly at the beam impact, SE_2 are generated by exiting BSE further away, SE_3 are generated by BSE when hitting parts of the specimen chamber. [28]

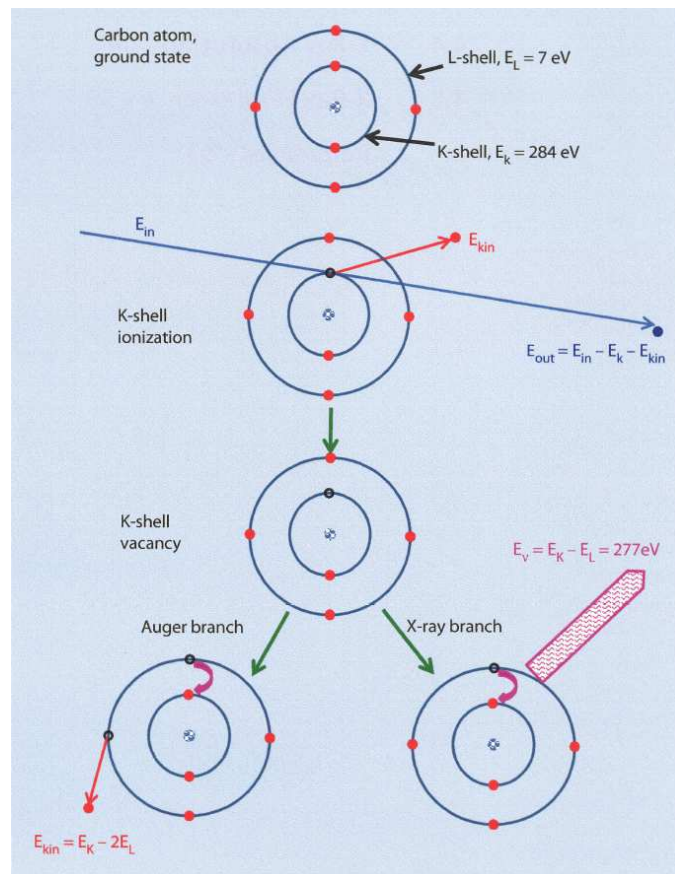


Figure 2.16: Schematic diagram of the process of X-ray generation. [28]

bound to the atom, with an ionization energy of 7 eV. An incident energetic beam electron having initial kinetic energy $E_{in} > E_c$ can scatter inelastically with a K-shell atomic electron and cause its ejection from the atom, providing the beam electron transfers to the atomic electron kinetic energy at least equal to the ionization energy, which is the minimum energy necessary to promote the atomic electron out of the K-shell beyond the effective influence of the positive nuclear charge. The total kinetic energy transferred to the K-shell atomic electron can range up to half the energy of the incident electron. The outgoing beam electron thus suffers energy loss corresponding to the carbon K-shell ionization energy $E_K = 284$ eV plus whatever additional kinetic energy is imparted:

$$E_{out} = E_{in} - E_K - E_{kin} \quad (2.14)$$

The ionized carbon atom is left with a vacancy in the K-shell which places it in a raised energy state that can be lowered through the transition of an electron from the L-shell to fill the K-vacancy. The difference in energy between these shells must be expressed through one of two possible routes:

1. The left branch in Figure 2.16 involves the transfer of this K-L inter shell transition energy difference to another L-shell electron, which is then ejected from the atom with a specific kinetic energy:

$$E_{kin} = E_K - E_L - E_L = 270 \text{ eV} \quad (2.15)$$

This process leaves the atom with two L-shells vacancies for subsequent vacancy-filling transitions. This ejected electron is known as an "Auger electron", and measurement of its characteristic kinetic energy can identify the atom species of its origin, forming the physical basis for "Auger electron spectroscopy".

2. The right branch in Figure 2.16 involves the creation of an X-ray photon to carry off the inter-shell transition energy:

$$E_\nu = E_K - E_L = 277 \text{ eV} \quad (2.16)$$

Because the energies of the atomic shells of an element are sharply defined, the shell difference is also a sharply defined quantity, so that the resulting X-ray photon has an energy that is characteristic of the particular atom species and the shells involved and is thus designated as a "characteristic X-ray". Characteristic X-rays are emitted uniformly in all directions over the full unit sphere with 4π steradians solid angle. [...] The characteristic X-ray photon has a very narrow range of just a few eV depending on atomic number [...].

The two branches are not equally probable. Instead the probability for X-ray emission is expressed by the "fluorescence yield" ω , which is displayed in Figure 2.17 for the K- and L-shell. This means that heavier elements are much more sensitive to X-ray analysis than for example C. For elements that can be analysed by different shells, the fluorescence yields decline from the K to the M shell: $\omega_K > \omega_L > \omega_M$.

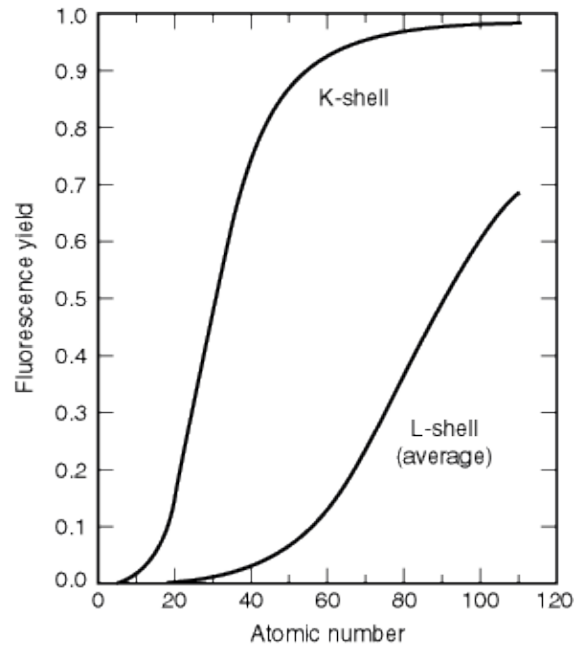


Figure 2.17: Fluorescence yield versus atomic number. The displayed L line represents the average of the L_1 , L_2 and L_3 lines, which differ by less than 10% over most of the periodic table. [34]

Two systems are in use for designating X-rays. The traditional but now archaic Siegbahn system lists the shell where the original ionization occurs followed by a Greek letter or other symbol that suggests the order of the family members by their relative intensity, $\alpha > \beta > \gamma > \eta > \zeta$. For closely related members, numbers are also attached, for example, $L\beta_1$ through $L\beta_5$. [...] The Siegbahn system has been officially replaced by the International Union of Pure and Applied Chemistry (IUPAC) labeling protocol in which the first term denotes the shell or subshell where the original ionization occurs while the second term indicates the subshell from which the electron transition occurs to fill the vacancy; for example, $K\alpha_1$ is replaced by $K-L_3$ for a K-shell ionization filled from the L_3 subshell.

However, since the Siegbahn system is still widely used in literature and also in commercial X-ray analysis software systems, it is used in this thesis. The principle of energy dispersive X-ray spectroscopy is the similar to BSE detection. X-rays are absorbed in the active volume of a Si semiconductor.

The entire energy of the photon is transferred to a bound inner shell atomic electron, which is ejected with kinetic energy equal to the photon energy minus the shell ionization energy, 1.838 keV for the Si K-shell and 0.098 keV for the Si L-shell. The ejected photoelectron undergoes inelastic scattering within the Si crystal. One of the consequences of the energy loss is the

promotion of bound outer shell valence electrons to the conduction band of the semiconductor, leaving behind positively charged "holes" in the valence band. In the conduction band, the free electrons can move in response to a potential applied between the entrance surface electrode and the back surface electrode across the thickness of the Si crystal, while the positive holes in the conduction band drift in the opposite direction, resulting in the collection of electrons at the anode on the back surface of the EDS detector. This charge generation process requires approximately 3.6 eV per electron hole pair, so that the number of charge carriers n is proportional to the original photon energy, E_p :

$$n = E_p/3.6 \text{ eV} \quad (2.17)$$

Since the number of generated free charges rises linearly with photon energy, different energies from approximately 50 eV to 30 keV or more can be distinguished by the succeeding charge in the collection anode. Therefore the detection principle is named "energy dispersive".

Originally Li-drifted Si detectors with a uniform electrode on the front and rear surface were used. These have been replaced over the last few years by Si drift detectors (SDD). A schematic of its design can be seen in Figure 2.18.

The measurement principle is the same as with a uniform front surface electrode, but the rear surface electrode is formed in a pattern of concentric rings (grey) around a central small anode (blue). A field gradient applied to the individual rings creates internal "collection channels", through which the free electrons generated anywhere in the detector volume (light blue) are guided to the central anode for collection. This collected charge is converted into a voltage by the field effect transistor (FET) preamplifier. This voltage signal is the input for the pulse processor for measurement. Each X-ray is represented as a step on a linearly increasing voltage ramp that is reset periodically (see Figure 2.19). The generated EDS spectrum is a histogram with energy bins along the abscissa and the ordinate is the number of photons whose energy fits within the bin value. The width of the peaks is mainly determined by noise and limits the ability to distinguish closely spaced peaks. The energy resolution is expressed by the full peak width at half-maximum height (FWHM). The FWHM is a function of the photon energy, Fiori and Newbury [35] approximated the experimental results:

$$\text{FWHM}(E) = [2.5(E - E_{ref}) + \text{FWHM}_{ref}^2]^{1/2} \quad (2.18)$$

where $\text{FWHM}(E)$, FWHM_{ref} , E and E_{ref} are expressed in eV. The reference values can be taken from the values for Mn $K\alpha$ for a particular EDS system. Generally the FWHM lies in the range of about 100 eV.

The SDD design allows for faster depletion of the anode and thus higher count rates at high energy resolution, speeding up the analysis significantly. This is especially the case for X-ray mapping which has been revolutionized by this new detector. [28, 36]

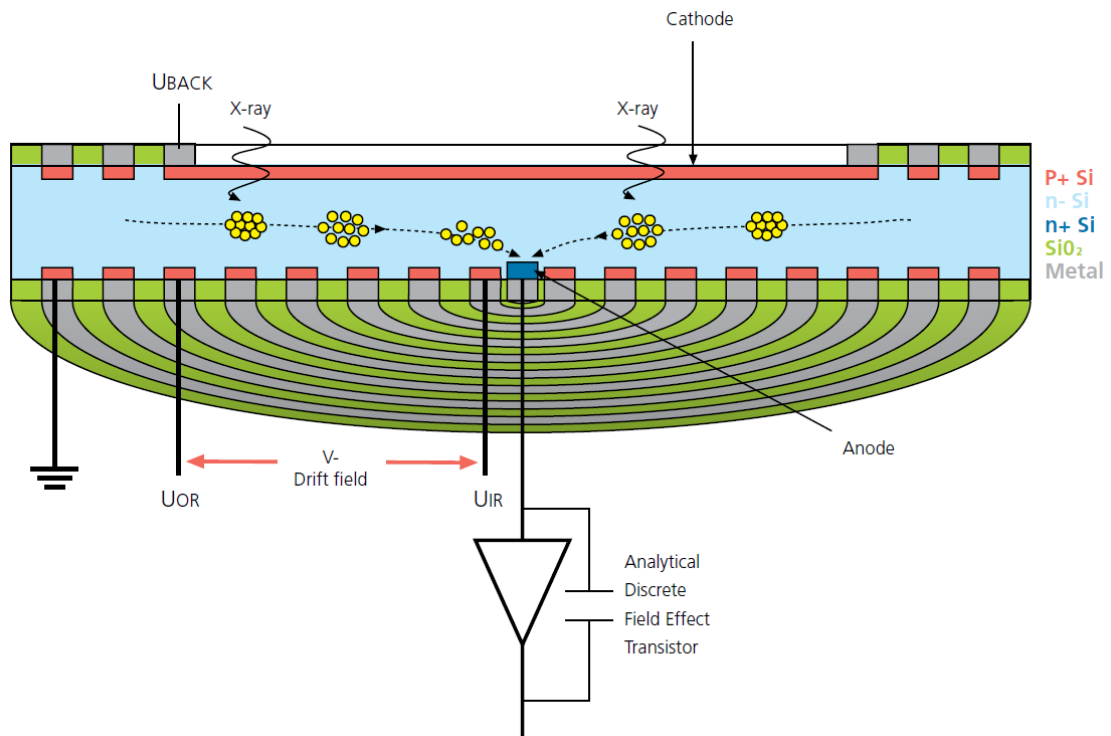


Figure 2.18: Schematic of the silicon drift detector (SDD). A field gradient applied to the electrode rings (grey) "drifts" the free charges generated in the active detector volume (light blue) to the anode (blue) for collection. The charge is converted into a voltage by a field effect transistor (FET). [36]

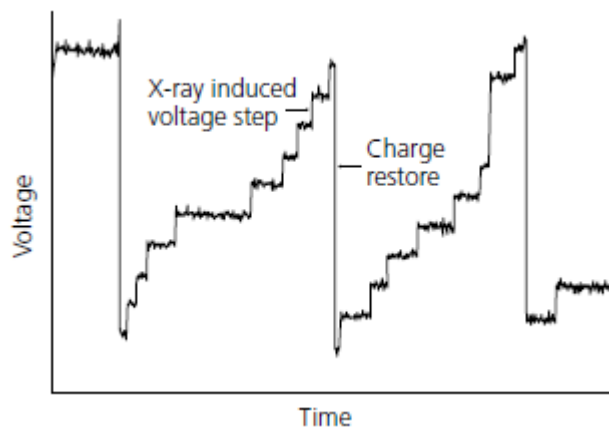


Figure 2.19: Voltage ramp created by the FET preamplifier. X-ray photons appear as steps in the linear ramp that is reset periodically. [36]

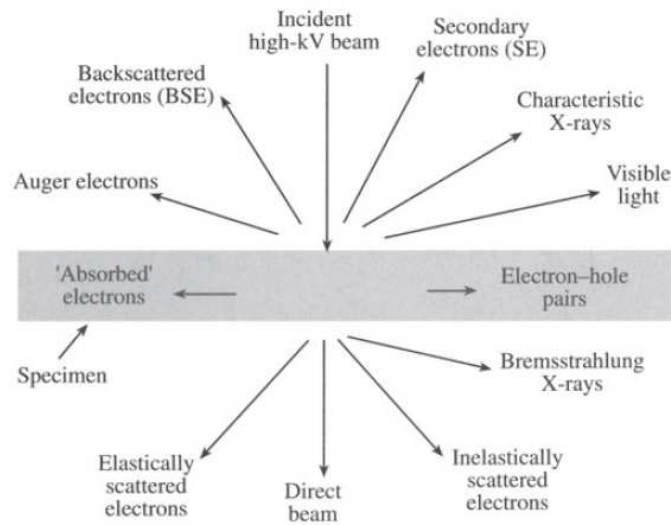


Figure 2.20: Schematic of the possible interactions in a transmission electron microscope. [37]

2.5 Transmission Electron Microscope

The biggest drawback of scanning electron microscopy is that nano-domains are generally not accessible because of the interaction volume. A technique that circumvents this resolution limit is the transmission electron microscope (TEM). Its working principle is similar to the SEM, but with a few alterations. First the energy of the electrons is much higher, a usual accelerating voltage is 200 kV. Second the samples are thinned to less than 100 nm thickness, allowing the electron beam to pass through it without significant scattering. Therefore the interaction volume is much smaller, allowing resolution of even single atoms. During transmission the same interactions occur as in SEM, but a few additional analytical techniques can be employed, a summary of possible interactions is shown in Figure 2.20. The transmitted electrons can be scattered elastically or inelastically, allowing imaging of different properties. For example "electron energy loss spectroscopy" (EELS) yields information of the elemental composition with a high sensitivity to light elements, dark field microscopy allows imaging of Z- and height-contrasts and even diffraction on nanocrystals is possible, containing information of crystal structure and lattice parameters. This makes the TEM a very powerful analytical tool, however there are limitations as always. Buying and operating a TEM is extremely costly, the requirements for sample preparation are very high, since thicknesses of less than 100 nm are necessary. A lot of materials cannot withstand the high energy beam, resulting in radiation damage. Also the sampling area is extremely small, so you always need to know where to look beforehand. For these reasons TEM can only be the pinnacle of analytical tools used in addition to other techniques. [37]

2.6 Secondary Ion Mass Spectrometry

In Figure 2.21 the schematic of a time of flight - secondary ion mass spectrometer is displayed.

The sputtering process central to the SIMS technique can be described as a collision cascade of particles in the sample being analysed. Ions from the primary source impinge upon the sample and set atoms in motion, both by direct collisions between the primary ions and the atoms in the sample or indirectly by collisions of atoms in the sample already in motion with other atoms in the sample (knock-on effects). Typical energies of the primary ions are in the keV range, so the direct collisions between the primary ions and the atoms in the sample are highly energetic compared to bond energies. This results in extensive fragmentation and bond breaking near the collision site, producing essentially only the emission of atomic particles. As the collision cascade moves away from the collision site, the collisions become less energetic. This results in less fragmentation and bond breaking, producing the emission of molecular fragments. Particles produced in approximately the top 2 – 3 monolayers (ML) of the sample have sufficient energy to overcome the surface binding energy and leave the sample. These sputtered particles are ejected as neutral atoms and molecules, electrons, and ions. Only a small fraction of them are charged ($10^{-6} - 10^{-1}$), and their positive or negative state depends on their electron configuration. The mass to charge ratio (m/z) of the species are analysed and yield positive and negative secondary ion mass spectra consisting of the ion m/z versus the number of ions detected at each m/z .

Different mass analysers can be employed to separate the secondary ion, a very potent one is the "Time of Flight" (ToF) analyser. Its attributes are high transmission and parallel detection of all masses, as well as high mass resolution $m/\Delta m$ (often beyond 10 000). The ToF analyser separates secondary ions according to their mass to charge ratio m/z due to the different travel velocities of ions with different masses. The primary ion source must be pulsed with short pulse widths to yield "packages" of secondary ions with minimal time dispersion, and thereby minimal energy spread. Each secondary ion package is extracted by electric fields and thus given the same kinetic energy E_{kin} and travel through a field free flight tube. Because of

$$E_{kin} = \frac{mv^2}{2} = \frac{mL^2}{2zt^2} \quad (2.19)$$

where L is the length of the flight tube, that is about 1 m in length, and t is the flight time. Heavier ions travel slower and reach the detector later than lighter ions, allowing time-resolved analysis of all masses. The reflectron, or ion mirror, consists of a series of electrodes that reverse the ions travel direction, focussing them energetically. Since all ions possess some thermal energy before being sputtering some move faster than others despite the same m/z . The reflectron therefore increases the mass resolution further.

SIMS must be performed under ultra high vacuum (UHV), to prevent contamination and ensure that primary and secondary ions can reach their final destination without collisions from ambient gases, also some of the components require vacuum to operate.

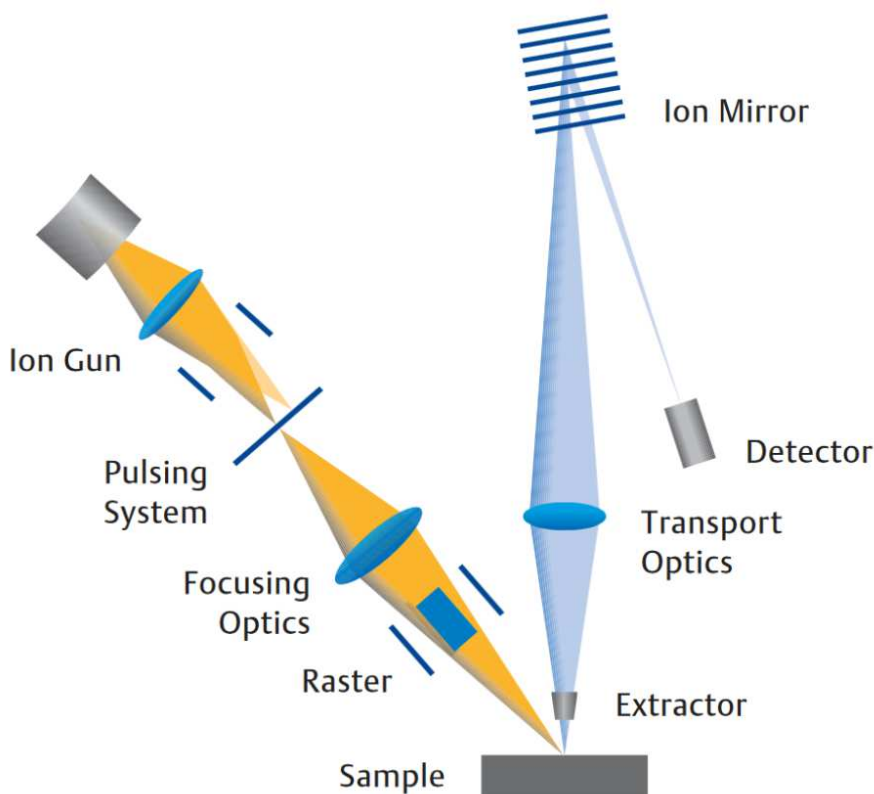


Figure 2.21: Schematic of a time of flight - secondary ion mass spectrometer. [39]

By focussing the primary ion beam diameter to less than 150 nm and subsequent rastering over the sample surface, chemical imaging can be recorded, where each pixel contains a whole mass spectrum. By using a second ion gun a sample layer of few nm can be removed allowing depth profiling. By combination of depth profiles with a x - y raster even full three-dimensional chemical profiles can be recorded. A major drawback of this technique is that direct quantitative analysis is not possible due to heavy influence of matrix effects on ion yields. The cost of acquisition and operation is very high as well. [38]

2.7 X-Ray Photoelectron Spectroscopy

The physical basis of X-Ray Photoelectron Spectroscopy is the photoelectric effect. The general interaction of atoms with X-rays is described in subsection 2.4.5, one particular process is of interest for this technique. If the photon energy is sufficiently high, an electron can absorb it and leave the atom, resulting in a vacancy that can be filled up and lead to characteristic X-Rays or Auger-electrons of the sample atom. The ejected "photoelectron" itself contains elemental information too. By absorbing the photon completely it gains a

kinetic energy E_{kin} , according to:

$$E_{kin} = h\nu - E_B - \Phi \quad (2.20)$$

where h is the Planck's constant, ν the photons frequency, E_B the binding energy of the electron and Φ the work function of the instrument, which represents the minimum energy for an unbound electron to escape the sample. Therefore when $h\nu$ is higher than $E_B + \Phi$, the electron gains enough energy to escape the sample and be detected. The binding energy of the electron is characteristic of the electronic structure. Inner shell states are nearly unaffected by chemical bonding, thus their binding energies are characteristic of the atom's species. For this reason photoelectrons from these inner states allow identification of the samples chemical composition.

A major advantage of XPS is the surface sensitivity. Contrary to characteristic X-rays detected in EDX, photoelectrons interact strongly with solid matter, leading to inelastic scattering after short travel paths. They lose some of their characteristic energy after a few nm, therefore only electrons from typically the top 10 nm of the sample escape with their original energy, contributing to the respective peaks. This allows the analysis of a very shallow surface region. Another benefit is the so called chemical shift. Inner electronic states do not form bands in a solid like valence electrons, however they still experience forces from chemical bonds of compounds. This leads to a slight shift in E_B of usually 1-5 eV and subsequently in E_{kin} , allowing XPS to distinguish photoelectrons from different chemical states.

A schematic of an XPS can be seen in Figure 2.22. The Spectrometer must operate in UHV conditions, one reason for this is to avoid sample contamination, for which this technique is extremely sensitive. The other reason is to increase the mean free flight path of the photoelectrons that need to travel a distance of ≈ 1 m before arriving at the detector. There are two commonly used X-ray sources, Mg and Al, that emit their characteristic Mg $K\alpha$ ($h\nu = 1253.6$ eV) and Al $K\alpha$ ($h\nu = 1486.6$ eV). All elements can be detected with XPS, except for H and He, their photoelectron cross sections are below the detection limit, they also have no core states with characteristic energy. The dispersion of electrons with different kinetic energies is done by one of two designs, the cylindrical mirror analyzer and the concentric hemispherical analyzer. The latter one was applied for this thesis, therefore its principle will be further explained. The photoelectrons pass a focussing electron optic system leading into the hemisphere. specific potentials are applied to the inner and outer shell of this hemisphere, with the positive pole inside and the negative pole outside. The electrostatic field enacts a force on the electrons, bending their flight path. Electrons with different E_{kin} and therefore different velocities follow different flight paths, of which only a small fraction passes through the exit slit to the detector. By scanning the electric field different fractions of the energy can pass to the detector sequentially, allowing the recording of a spectrum. The resulting spectrum lists intensity over E_{kin} , but for easier interpretation the abscissa is usually calculated into E_B , resulting in a reversed scaling. [40–42]

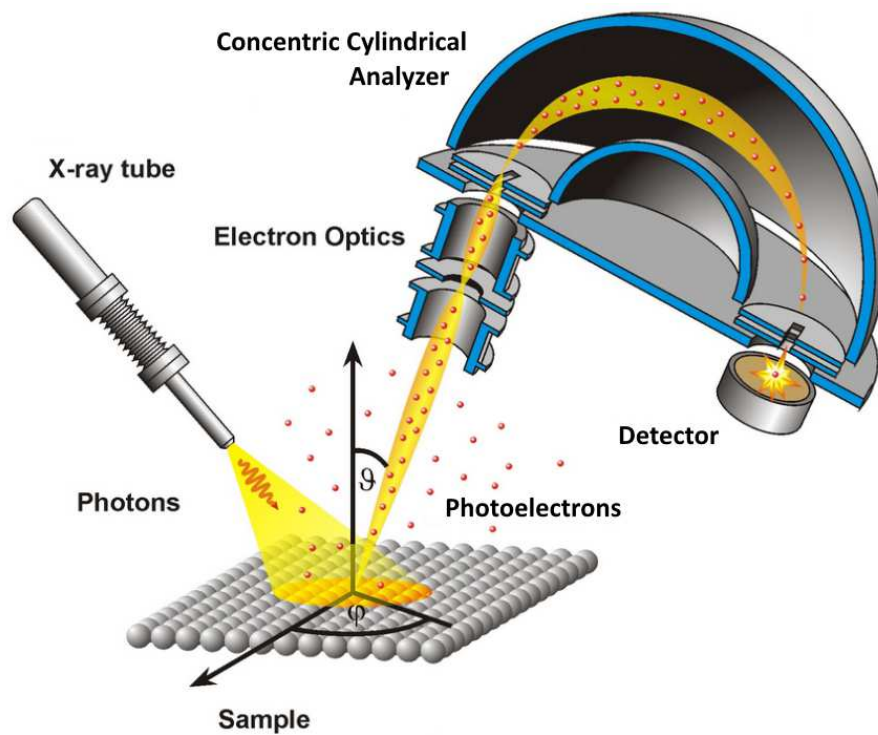


Figure 2.22: Schematic of an x-ray photoelectron spectroscope with concentric hemispherical analyzer. Adapted from [43]

3 Experimental

3.1 Used Chemicals

A variety of different bases and salts were used to de-coat the samples. For a two step procedure acids were also utilized in a kinetically controlled reaction. The list of used chemicals can be seen in Table 3.1. The water used in all experiments was purified by reverse osmosis using a Barnstead EASYPURE II system (Thermo Fisher Scientific), resulting in ultra pure water with a resistivity of $18.2\text{ M}\Omega$. The chemicals were handled in 50 mL PP centrifuge tubes supplied by Brand. The samples investigated by ICP-OES were prepared in 10 mL PP test tubes supplied by Corning Life Sciences with PE plugs supplied by VWR. Eppendorf Reference® 2 Pipettes with epT.I.P.S.® Standard tips were used for pipetting the liquids.

3.2 Stripping Experiment

3.2.1 Investigated Samples

In Table 3.2 a list of all investigated samples can be seen that were created by the Institute of Materials Science and Technology (TU Wien) [10] by placing the cemented carbide substrates in the facility and evaporating a metallic Al/Cr target in a low pressure N_2 -atmosphere. The substrate was WC with 6 % Co for the stripping experiment, Si wafers were coated additionally for interlayer investigations. In all cases. In most samples the arcing target was a metallic disk with an Al/Cr-ratio of 70/30 at%, in some a 90/10 composition was used.

The evaporated atoms were accelerated to the substrate with a bias voltage, which was varied from -40 to -150 V . In customary samples three bias ranges are used, first a sub-layer with -40 V is deposited, which features better adhesion to the substrate. Then the voltage is increased in a short gradient to -150 V . At this bias voltage the especially dense top-layer is formed. Therefore the coating consists of three sub-layers with slightly different properties. At first samples with all of these biases were created, but since they showed no significant differences in stripping behaviour, only samples with -40 V were created subsequently. Since only the interface to the substrate was of interest, which is positioned in this sub-layer, limiting the arcing conditions to this voltage is justifiable. The whole coating process lasted 54 min, resulting in coatings of about $3\text{ }\mu\text{m}$ in thickness. Before the coating process the arcing cathode was sandblasted with corundum in some cases. This removed the nitride layer that formed during the previous deposition. Two different particle size classes, as defined by the "Federation of European Producers of Abrasives" [44], were used for sandblasting : F46 with $300\text{-}425\text{ }\mu\text{m}$ (Coarse) and F150 with $36\text{-}106\text{ }\mu\text{m}$ (Fine). The gas composition was altered as well to create special compositions

Table 3.1: Used Chemicals

Substance	Quality	Supplier
LiOH	98 %	Merck
NaOH	p.a. ≥ 99.0 %	Emsure
KOH	p.a. ≥ 85.0 %	Emsure
CsOH · H ₂ O	96 %, CsCO ₃ <5 %	Alfa Aesar
Ca(OH) ₂	p.a.	Merck
NaCl	p.a. ≥ 99.5 %	Merck
HCl	37 % p.a.	Emsure
HNO ₃	65 % p.a.	Emsure
H ₂ SO ₄	GPR Rectapur 95 %	VWR Chemicals
H ₂ O ₂	30 %	Merck

and properties at the interface of substrate and coating. The standard gas atmosphere was 1000 sccm N₂, creating the wanted nitride. In some samples the gas was changed to Ar or O₂ at different concentrations for the first few s or min, leading to metallic or oxidic interlayers. After this initial time span the atmosphere was switched again to 1000 sccm N₂ to form the nitride coating above.

The sample list can be subdivided into different "sample classes": Samples 701-710 were preliminary samples to investigate the coatings behaviour, the de-coating mechanism, grain size influences and different leaching agents. Samples 718-724 contained an oxidised interlayer, 736 and 740-751 were samples with metallic interlayer, while Sample number 737 was a completely metallic coating. Samples 738-739 were entirely composed of 90/10 Al/Cr ratio, while sample numbers 752-756 were samples with a 90/10 interlayer underneath a 70/30 coating. Interlayer investigations were carried out with a selected few of the samples.

3.2.2 Sample Pretreatment

The cemented carbide samples investigated were plates with dimensions of 12 × 12 × 4 mm³ consisting of WC with 6 % Co. In Figure 3.1 a photo of these samples can be seen. Since only a limited amount of these expensive substrates was available, while a great number of individual stripping experiments needed to be conducted the samples were cut before the reaction in four pieces each. This was done with an Accutom-50 by Struers with a 6" diamond cut-off wheel. This left samples with a coated area of about 5 × 5 mm², sufficient to study de-coating processes while quadrupling the specimen count.

3.2.3 Chemical Digestion

The samples were cleaned with acetone and water after cutting and handled with ceramic prongs to avoid contamination. The digestion was done in 25 mL PFA-tubes heated by a 300 × 200 mm² PFA coated graphite heating plate, the temperature was regulated with a programmable regulator, all purchased by AHF Analysentechnik. However, PFA is a

Table 3.2: Sample list created by cathodic arc evaporation. The Al/Cr ratio, bias voltage, use of sandblasting (fine/coarse sand) and gas atmospheres were varied. Sand particle size classes are: "Fine" = 36-106 μm , "Coarse" = 300-425 μm . Samples with an entry in the column "Time" were first coated with the alternative gas in the list before switching to 1000 sccm N_2 for the rest of the coating procedure. Samples without time entry were coated for the entire duration with the listed gas and concentration.

Sample number	Al/Cr ratio	Bias in V	Sandblasted	Atmosphere		
				Gas	Concentration	Time
701	70/30	-40 to -150	-	N_2	1000 sccm	
702	70/30	-150	-	N_2	1000 sccm	
703	70/30	-40	-	N_2	1000 sccm	
704	70/30	Gradient	-	N_2	1000 sccm	
706	70/30	-40	Fine	N_2	1000 sccm	
707	70/30	-40	Coarse	N_2	1000 sccm	
708	70/30	-40	Coarse	N_2	1000 sccm	
709	70/30	-150	Coarse	N_2	1000 sccm	
710	70/30	-150	Fine	N_2	1000 sccm	
718	70/30	-40	-	O_2	100 sccm	2 min
719	70/30	-40	-	O_2	50 sccm	2 min
722	70/30	-40	-	O_2	200 sccm	2 min
723	70/30	-40	-	O_2	100 sccm	5 min
724	70/30	-40	-	O_2	100 sccm	1 min
736	70/30	-40	-	Ar	300 sccm	5 min
737	70/30	-40	-	Ar	300 sccm	
738	90/10	-40	-	N_2	1000 sccm	
739	90/10	-40	Fine	N_2	1000 sccm	
740	70/30	-40	-	Ar	300 sccm	1 min
741	70/30	-40	Fine	Ar	300 sccm	1 min
742	70/30	-40	-	Ar	300 sccm	20 s
750	70/30	-40	-	Ar	300 sccm	30 s
751	70/30	-40	-	Ar	300 sccm	45 s
752	5 min 90/10 - 70/30	-40	-	N_2	1000 sccm	
753	3 min 90/10 - 70/30	-40	-	N_2	1000 sccm	
756	1 min 90/10 - 70/30	-40	-	N_2	1000 sccm	

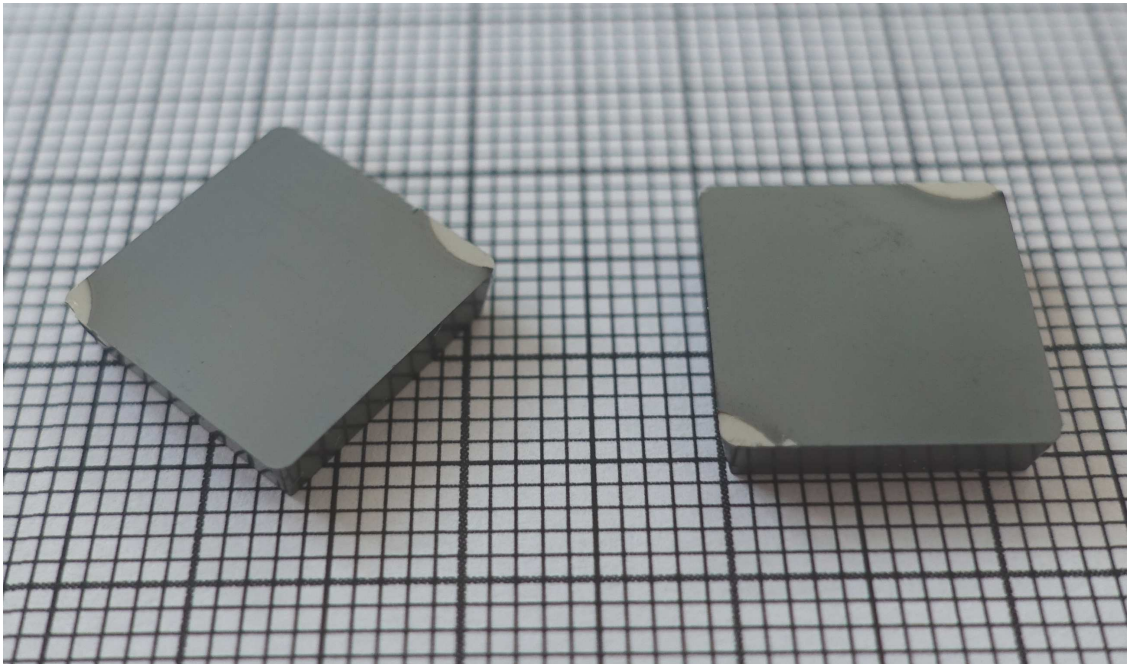


Figure 3.1: Image of two substrate plates. The dark grey area stems from the AlCrN coating, the light grey corners are the cemented carbide substrate that was covered by the substrate holder during coating.

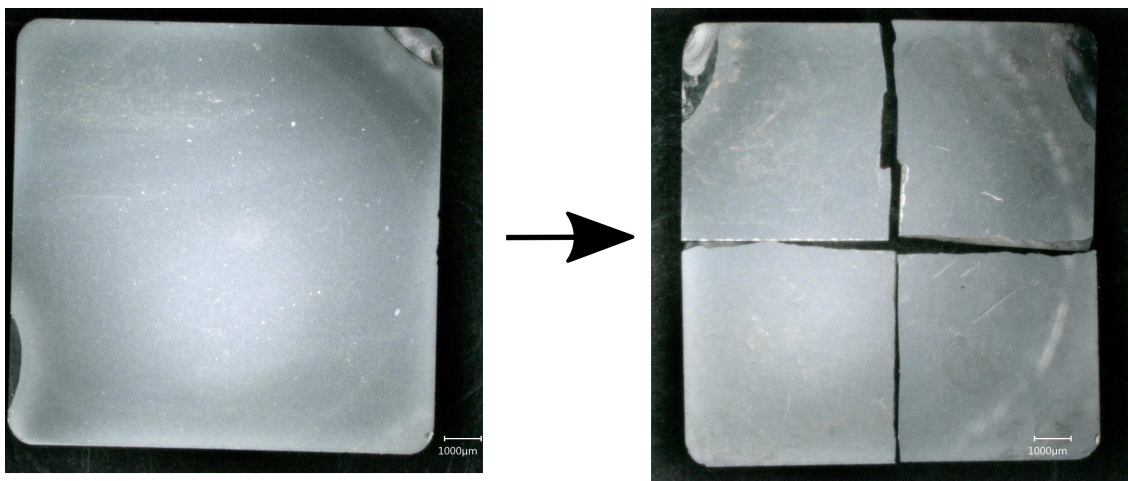


Figure 3.2: Microscopic view of a cemented carbide sample before and after cutting.

poor thermal conductor and the tubes possess a relatively thick ground plate of ≈ 1 mm thickness. Therefore the real temperature inside the tubes was calibrated with a P400 thermometer by Dostmann electronic GMBH to adjust the temperature accordingly. Aside from the basic leaching, a two step process was also tried. The coating system was first weakened in a kinetically controlled reaction using acids and oxidising agents, in the second step 50 % NaOH was used again to spall the coating off. The used chemicals were 1:1 HNO₃:H₂O₂, 1:1 HNO₃:H₂SO₄ and pure HCl, HNO₃ and H₂SO₄. For the digestion 5 mL of base or acid were pipetted into a tube and then put on the hot heating plate. This amount ensured that the samples were always covered by liquid while refluxing. After half an hour, when the reactant reached the desired temperature of up to 140 °C, the tubes were screwed open and the sample put inside. After closing the tube again the timer was set for the desired duration. The reaction was stopped by removing the sample from the tube and instantly quenching it with water. This also washed off any splinters that laid on the sample. Before and after the experiment each sample was weighted to measure the mass difference. However, since the mass loss was very low, only about 1 mg, this parameter could only be used qualitatively to determine if an attack had happened or not. The samples were afterwards analysed with SEM, the leaching agent by ICP-OES.

3.3 ICP-OES Analysis

3.3.1 ICP-OES Parameters

The used ICP-OES was a Thermo Fisher Scientific iCAP 6500 radial with a ASX-520 autosampler by CETAC Technologies. The liquids were introduced by a high solid sample introduction kit with a quartz concentric nebuliser and a quartz cyclone spray chamber without ascension tube. A quartz plasma torch with inner diameter of 1.5 mm was used. Data acquisition and evaluation was done by Qtegra software, provided by the manufacturer of the instrument. The operational parameters are listed in Table 3.3, the used ICP standards were purchased by Merck, which are listed in Table 3.4. In was measured as internal standard, however all signals were stable during the measurement, rendering the internal standard superfluous.

3.3.2 ICP-OES Measurement

For quantification an external calibration with the standards listed in Table 3.4 was utilized. The mass loss of a completely de-coated sample was usually only ≈ 1 mg and only a small fraction of this amount was actually dissolved metal (the few nm of soluble interlayer), the majority of the coating broke off in splinters. These splinters had to be separated from the solution because they were not the object of interest and would plug the nebulising system of the ICP-OES. This was done by centrifuging the suspension at 10 000 g for 10 min, afterwards 900 μ L of the clear solution were pipetted into 10 ml autosampler tubes. The sample was then diluted with 6.2 ml H₂O and 1.9 ml concentrated HNO₃. The large amount of HNO₃ was needed to acidify the concentrated NaOH to a pH of $\approx 0 - 1$. Care had to be taken to always pipette the water first, since the concentrated acid and base react vigorously in direct contact, leading to instant boiling. Even with the

Table 3.3: List of used OES parameters.

Parameter	Value	Unit
RF power	1200	W
Purge pump rate	1.6	mL/min
Analysis pump rate	0.8	mL/min
Viewing height	12	mm
Coolant gas flow	12	l/min
Nebuliser gas flow	1	l/min
Auxiliary gas flow	0.8	l/min
Exposure time	10	s
Replicates	3	
Analytical Wavelength		
Al	396.152	nm
Cr	283.563	nm
Co	238.892	nm
W	239.709	nm
In	325.609	nm

Table 3.4: List of used OES Standards.

Element	Standard	Product Number	c in mg/L
Al	Certipur® Multi-element VIII	1094920100	98 ± 3
Cr	Certipur® Multi-element VIII	1094920100	100 ± 3
Co	Certipur® Multi-element VIII	1094920100	99 ± 3
W	Certipur® Single W	1703640100	999 ± 5
In	Certipur® Single In	1703240100	985 ± 5

water as a buffer the resulting solution heated up to a degree that the tubes could only be held at the edges while wearing gloves. HCl was avoided as acid because it forms the non-volatile NaCl with the sample which contaminates the instrument.

This resulted in a dilution of 1:10, meaning that there was still a lot of Na⁺ present. However higher dilutions were not possible because of the low concentration of the metals that should be detected. Matrix matching of the standards with pure NaOH was necessary for two reasons: First, the high amount of Na⁺ can shift the temperature of the plasma and the ionization probabilities of the analytes. Second, even the p.a. quality of NaOH contains relatively large amounts of impurities that produce background signals that need to be considered. The standards were therefore prepared by diluting the corresponding amounts of the stock solutions with the blank solution that was created from 5.0 mL 50 % NaOH, 34.5 mL H₂O and 10.5 mL HNO₃. Six concentration levels were used: 10, 5, 1, 0.5 and 0.1 ppm and the blank solution. The internal standards was added last to achieve a concentration of 1 mg/L In.

During the investigation samples were treated with acids as well. One acid of special interest was HCl, to determine the dissolved metal content in it, the concentrated HCl was diluted to the fitting pH by pipetting 243 μ L of the acid and 8.76 mL of H₂O together. This sample was then measured in a series with regular NaOH bath samples. This means that the standards were created with HNO₃ and NaOH, therefore only a semi-quantitative conclusion can be drawn from this sample's results.

3.4 SEM Analysis

The used electron microscope was a FEI Quanta 200 MK 2 (Thermo Fisher Scientific), featuring a W-filament as emitter. The samples were prepared for measurement by fixating them on the sample stage with graphite tape. The measurements were conducted in high vacuum, most images were recorded with 20 kV at a working distance of \approx 10 mm, though lower voltages were applied for higher magnification of details. EDX spectra were recorded and evaluated using EDAX software to determine the chemical composition of features.

3.5 Interlayer Characterization

The interlayer was investigated with SIMS, TEM and XPS. The respective measurements were provided by the following divisions. SIMS depth profiles were recorded with an IONTOF TOF.SIMS 5 by Lukas Volgger (Institute of Chemical Technologies and Analytics, TU Wien) in negative ion mode, using Bi as primary ions and Cs for sputtering. Sample preparation was done by Philip Kutrowatz (USTEM, TU Wien) and Jakob Gruber (USTEM, TU Wien), TEM measurements were recorded by Tomasz Wojcik (USTEM, TU Wien) with a FEI TECNAI F20 (Thermo Fisher Scientific) (60-200 kV, FEG emitter). XPS analysis was performed by Markus Sauer (Analytical Instrumentation Center, TU Wien) using a SPECS u-Focus XPS/UPS System with an Al X-ray source.

The samples for TEM investigation were Si-wafers coated in the same manner as the cemented carbide plates. These could easily be broken and prepared to the right dimensions, whereas WC-Co would require vastly increased effort to produce TEM-suitable

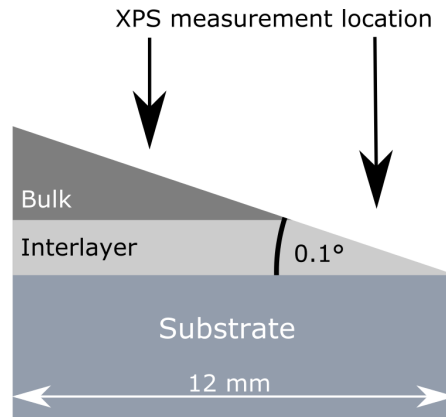


Figure 3.3: Schematic of the sample preparation method for XPS analysis.

samples due to its sturdiness, and even then the image quality would likely be inferior to Si samples.

The sample preparation for XPS analysis was an elaborate process. Since XPS is surface sensitive and the interlayer in a depth of $3\ \mu\text{m}$ should be detected, the coating needed be removed partially. The XPS system possesses an Ar sputter gun used for surface cleaning, however its erosion rate is very slow because a large area needs to be sputtered. This process could not have been done in an acceptable time span. Therefore the samples needed to be thinned mechanically. To fulfill the high precision requirements of this step, an inclined cut was tested. A schematic can be seen in Figure 3.3. Utilizing a very small angle, a slight slope of less than a μm over the 12 mm specimen length can be achieved. This leaves a stripe on the sample of matching coating thickness, where the sputter gun performed a surface cleaning with an acceleration voltage of 3 kV prior to measurement. Unfortunately only one of four test samples could be prepared successfully. The very high hardness of the coating and extremely small angle put the cutting machine to its limits, causing the desired slope to be achieved only on a sample with 90/10 interlayer underneath a 70/30 coating.

4 Results

4.1 Interlayer Investigation

In the following section the analysis of the solid samples by SEM/TEM, SIMS and XPS is described to characterize the interlayer and its influence on dissolution behaviour. In Figure 4.1 tilted SE images of two partly de-coated samples are depicted. The lower half of the images is occupied by the substrate, the receding coating takes place in the upper half. Both coatings show a large amount of surface droplets as they are generated during cathodic arc evaporation. In Figure 4.1(a) a coating consisting of all three bias ranges can be seen, while the coating in Figure 4.1(b) was created with just -40 V bias. In the left image the subdivision of the -40 and -150 V sub-layers is visible. The density and mechanical properties deviate from each other, therefore both sub-layers break off the surface individually. In the right image only a homogeneous layer is present that shows spallation from the substrate on the left edge. Thus the proposed stripping mechanism can be easily followed. The NaOH undercuts the coating either from the side, where uncoated substrate remains, or directly through the coating by assumed defects and cracks, though investigation of this path is not possible with SEM. By dissolving the adhering interlayer the coating loses contact with the substrate and splinters off. The straight lines on the substrate are grooves stemming from the grinding of the substrate prior to coating.

The stripping progress of a sample can be spotted by comparing the change in the coated area. The coating and substrate possess a similar grey tone, therefore distinguishing the phases by light microscopy is difficult. In SEM the Z-contrast can be used as well as EDX to circumvent the problem. A BSE image with higher magnification is displayed in Figure 4.2. Whenever both coating and substrate are present on a sample the high Z-contrast allows for easy and quick determination of the coated area. When a sample is either completely covered or uncovered, EDX is necessary to identify the phase. This qualitative analysis is quick and simple as shown with the two exemplary spectra.

In Figure 4.3 SIMS depth profiles of two samples are displayed. One of them was created with a sandblasted cathode and one without. The coating was penetrated after about 2500 s, indicated by the rise of the C^{2-} - and W^- -signals and decline of all other signals. C^{2-} , O^- and AlO^- rise at at the surface due to surface contaminations. Figure 4.3(b) shows a significant rise around 2500 s, meaning that the interlayer can be detected by SIMS. The O^- - and AlO^- -signals indicate that an increased O-content improves the solubility. Therefore the samples with oxidic interlayer were created in succession. However the measurement of a sample with metallic interlayer revealed the same rise in the signals, where no increased O-content should be present. Therefore caution has to be exercised when interpreting SIMS data, since the quantitative ion count is highly matrix-dependent.

Since the interlayer ranges in thickness from $\approx 10\text{-}100\text{ nm}$, it cannot be accessed with SEM. With TEM the interlayer can be investigated directly, Figure 4.4 shows four images.

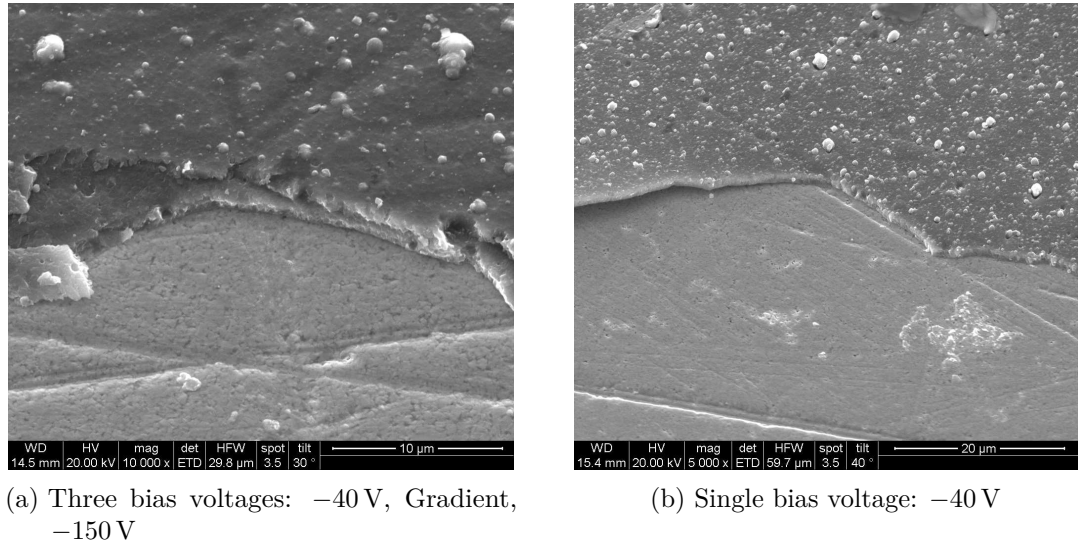


Figure 4.1: SE images of two partly de-coated samples, one with all three bias voltages and one with only -40 V. In (a) the two sublayers corresponding to the -40 V and -150 V bias voltage are visible. When using only -40 V, this subdivision does not exist. Also, in (b) the spallation of the coating from the substrate can be seen.

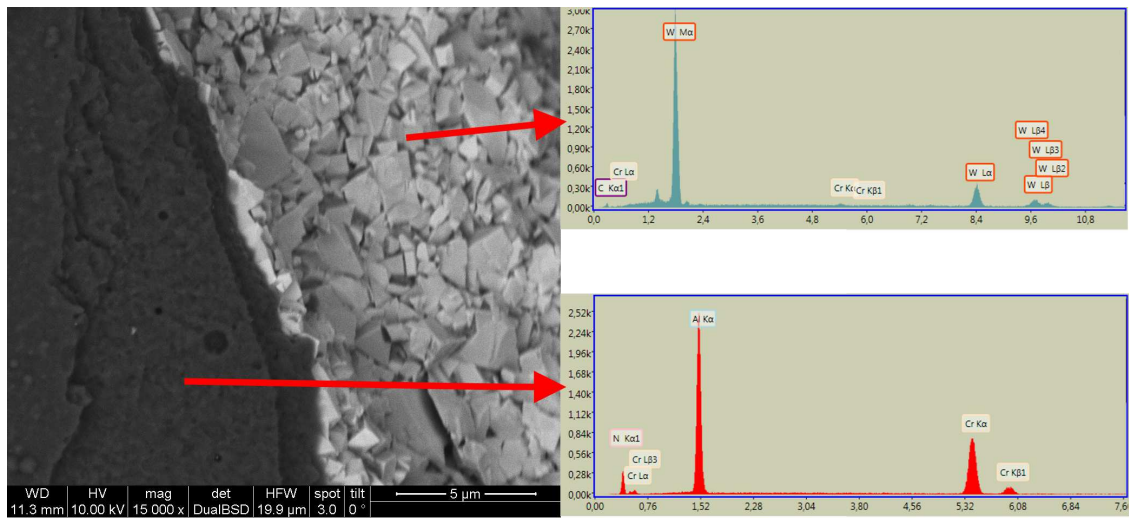
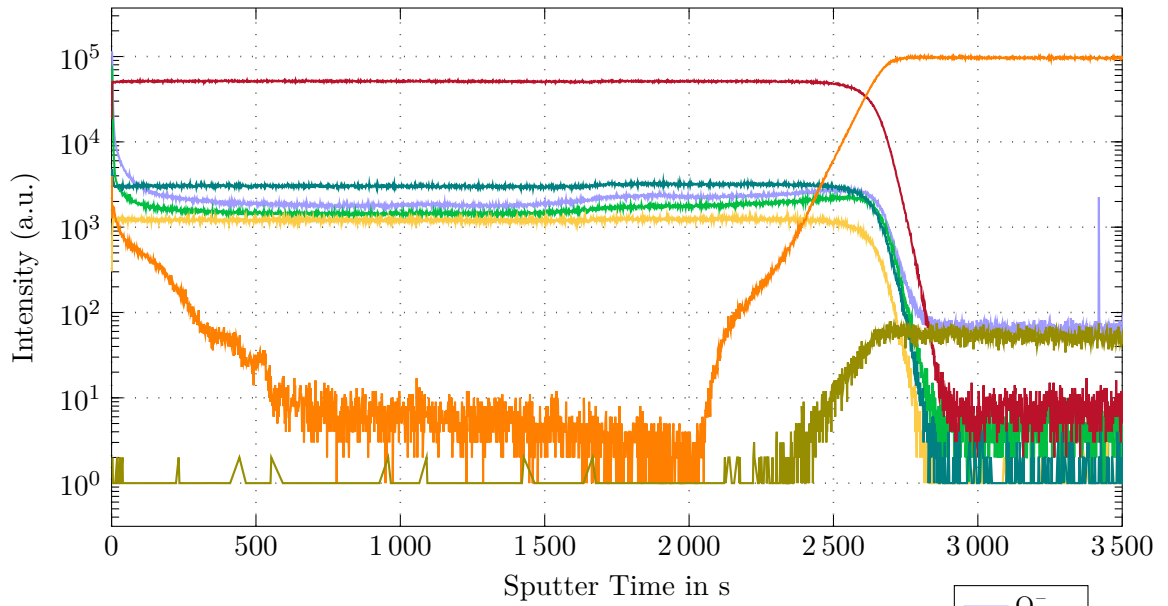
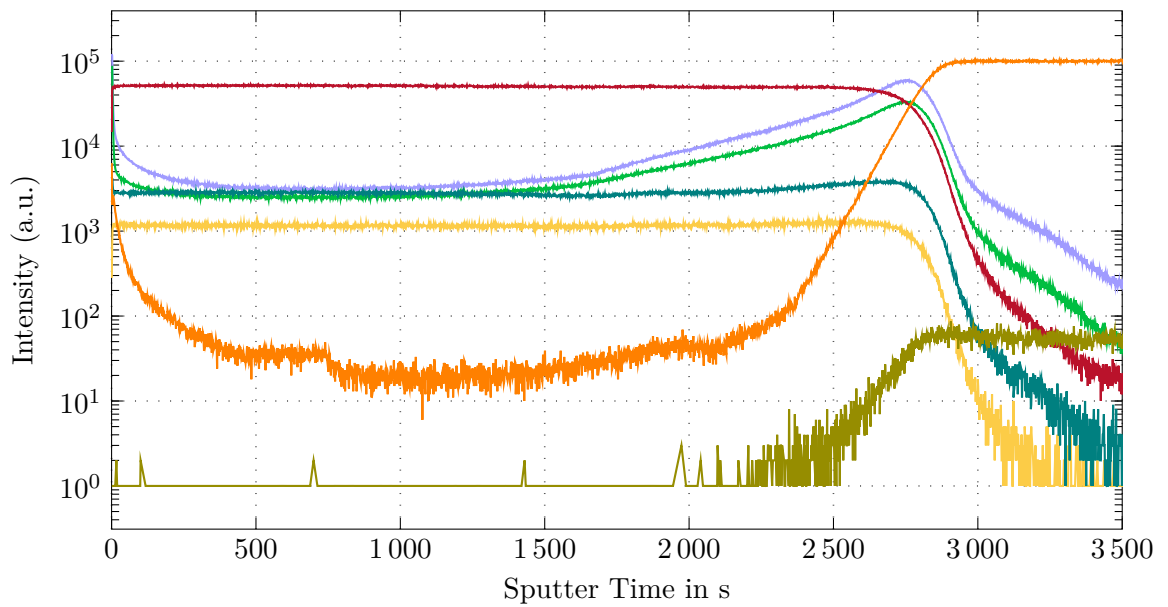


Figure 4.2: The coating system investigated by SEM/EDX. The BSE image shows the transition from the coating (dark) to the substrate (light), exemplary EDX-spectra of both phases are displayed in addition. The ordinate depicts the count rate, the abscissa the photon energy in keV. Only the most important W peaks are labeled.



(a) Not Sandblasted target



(b) Sandblasted target

Figure 4.3: SIMS depth profiles for samples with and without sandblasted cathodes.

In Figure 4.4(a) a HR-TEM image of the interlayer is seen, where single atoms can be distinguished. The interlayer is about 12 nm thick in this case. In the coating region the atoms show a very regular pattern where ordered atom rows can be seen. This is due to the ceramic nature of the material. The atoms in the substrate (Si) on the other side are placed in a seemingly random manner. The interlayer adopts this structure partially. On the side facing the coating the interlayer atoms continue the rows and somewhere in between this order is broken into the more random pattern of the substrate. On the lower right corner a small droplet with different atomic spacing can be seen. Figure 4.4(b)-(c) show larger cross sections of samples without sandblasted cathodes and with sandblasted cathodes. The coating represents the bright area and the substrate the dark edge. In Figure 4.4(b) a layered structure of the coating is visible, this is due to the arcing process. The doubled rotation of the whole carousel and each individual sample holder causes the samples to move to and from the target source away. These phases are visible in the cross section. The prominent feature of Figure 4.4(c), large droplets, could not be seen in the sample without sandblasted cathode. The different dissolution behaviour could therefore be explained by the presence of these. Figure 4.4(d) shows an EDX line-scan from the coating into a droplet. The distinct decline in the N- and the rise in the Al-signal reveal a mostly metallic composition in the droplet. This result gave the incentive to produce samples with a metallic interlayer.

XPS analysis allows the identification of chemical bonding states in a shallow surface region. As stated in section 3.5 the sample preparation was only successful for one sample with a 90/10 interlayer underneath a 70/30 coating. A bulk and a surface region were measured to compare the chemical states. In Figure 4.5 the survey scans of the two regions can be seen. Five different peaks could be distinguished, Cr 2p, O 1s, N 1s, Al 2p and W 4f. The presence of the small W 4f-peak shows that the interface region was measured correctly. In Figure 4.6 the integrated peaks of the metals and N are displayed. For easier visual comparison these spectra have been normalized to their strongest signals. From the spectra the peak areas can be used to quantify the elemental composition, the chemical shift gives information about the bonding quality. However in none of the peaks a significant shift can be seen, meaning that the interlayer with an Al/Cr ratio of 90/10 possesses the same ceramic bonding characteristics as the 70/30 composition. The integration of the peaks yields the composition listed in Table 4.1. Aside from the small amount of W in the interface region the composition varies distinctly as expected. The O-concentration falls from the interlayer into the bulk. A possible explanation is the input from either residual O₂ from the gas phase inside the coating chamber or from surface oxides on the arcing target. Since both should decrease with time the decline during growing coating thickness is plausible. The N-signal is rising in almost the same amount. Since N₂ is always at a surplus during coating this change can be understood accounting the O-content. Together, N and O form 52.10 (bulk) and 51.35 at% (interlayer) of the coating, which is almost the same total count. Therefore a mechanism, where O is initially implanted in the coating and complemented by the continuous N supply, seems likely. Since no O₂ was introduced for this sample as well this gradient can help understand the SIMS depth profiles. The Al/Cr ratio shows also a difference between the two regions as expected. In the bulk a ratio of 66.5/33.5 is obtained, in the interface it is 70.8/29.2, so not nearly as high as the nominal 90/10 ratio. This can be explained

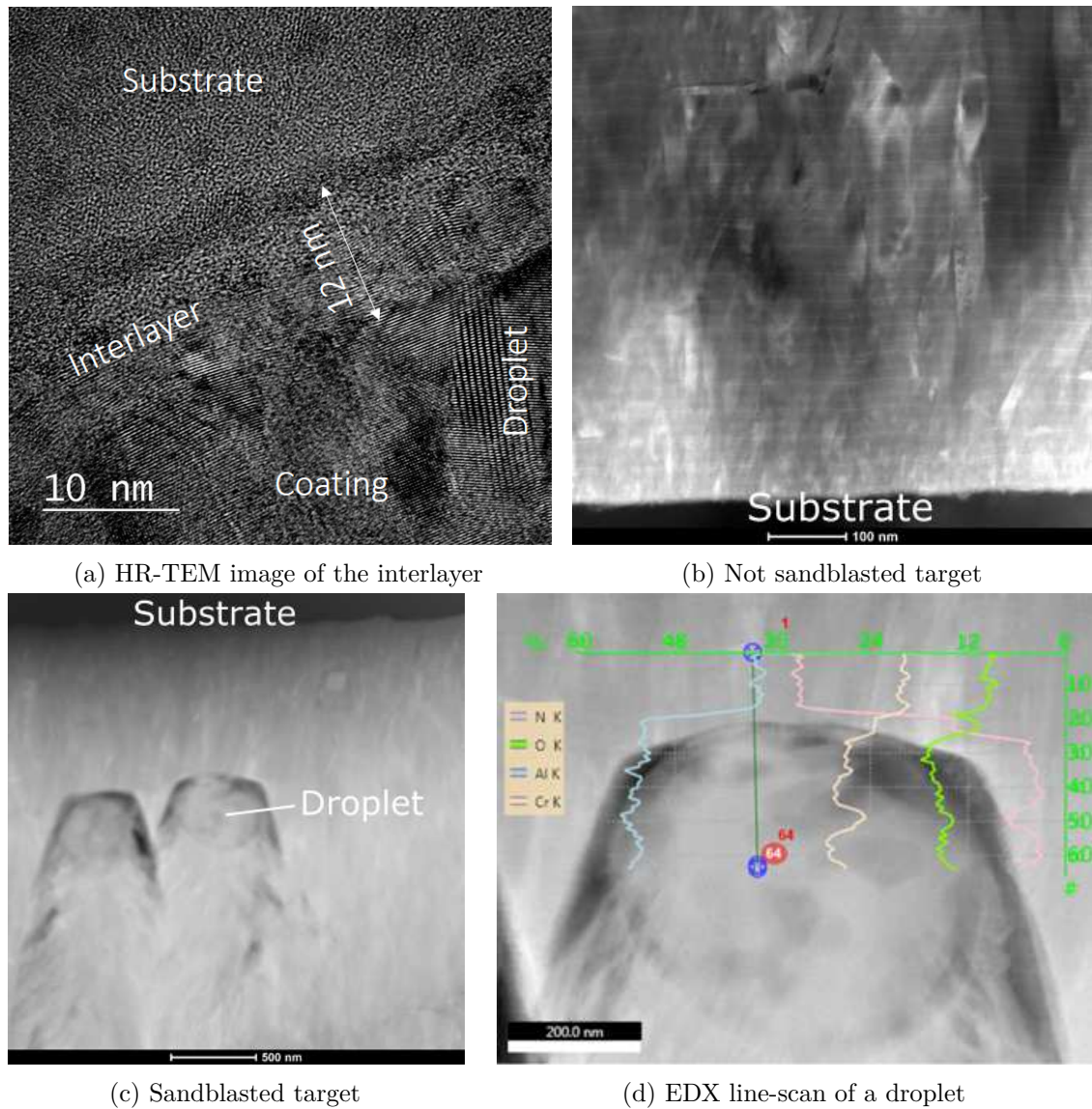


Figure 4.4: TEM analysis of the interlayer. A HR-TEM image of an interlayer can be seen in (a). (b) and (c) show samples without and with sandblasted cathodes. An EDX line-scan of a droplet is shown in (d).

Table 4.1: Quantitative XPS results.

Bulk region			
Element	BE (eV)	Area	at%
Cr 2p	575.5	2698.98	16.02
O 1s	532.0	511.69	12.10
N 1s	397.0	1039.34	40.00
Al 2p	74.5	247.11	31.87
Interface region			
Element	BE (eV)	Area	at%
Cr 2p	575.5	623.28	13.95
O 1s	532.0	195.68	17.44
N 1s	397.0	233.71	33.91
Al 2p	74.5	69.43	33.67
W 4f	32.0	35.43	0.94

with the sample preparation method. The samples were cut at a very low angle of 0.1° , still the X-ray beam was about $400\ \mu\text{m}$ in diameter. From the geometric relations in the triangle of the sample cross section a much larger depth than just the interlayer was measured. Therefore the results are "diluted" by the surrounding top-layer. Apart from these considerations the sputter gun itself can have an influence on the numbers as well. By high energy impact the surface contaminations can be pressed into the material, distorting the real composition. Unfortunately no other samples could be analyzed with XPS, as the comparison of different sample types was desired. This would probably have shed more light on the dissolution mechanics, the current findings remain very limited.

4.2 Investigation of Leaching Agents

Different leaching agents were tested for their ability to replace NaOH. ICP-OES analysis of NaOH was conducted to analyse dissolved metal concentrations.

In subsection 2.1.3 the solubility problems of AlCrN were discussed. To find optimal leaching agents, some limitations need to be considered: Al, the main metallic component in the coating, creates soluble species in strong acidic or strong basic conditions. The substrate cannot be expected to withstand acids for a prolonged time at elevated temperatures, therefore strong bases are needed. For sufficient reaction speed these need also to possess high solubility and chemical stability in water. From an economical viewpoint it also has to be relatively cheap because of the large amount needed in industrial processing. This limits the possible range of substances to the alkali hydroxides: LiOH ($pK_B = 0.18$), NaOH ($pK_B = -0.56$), KOH ($pK_B = -1.10$), CsOH ($pK_B = -1.76$). Other bases are either only weakly basic (like NH_3), possess too little solubility (like earth alkaline hydroxides) or are not sufficiently chemically stable (like many organic ions). Therefore

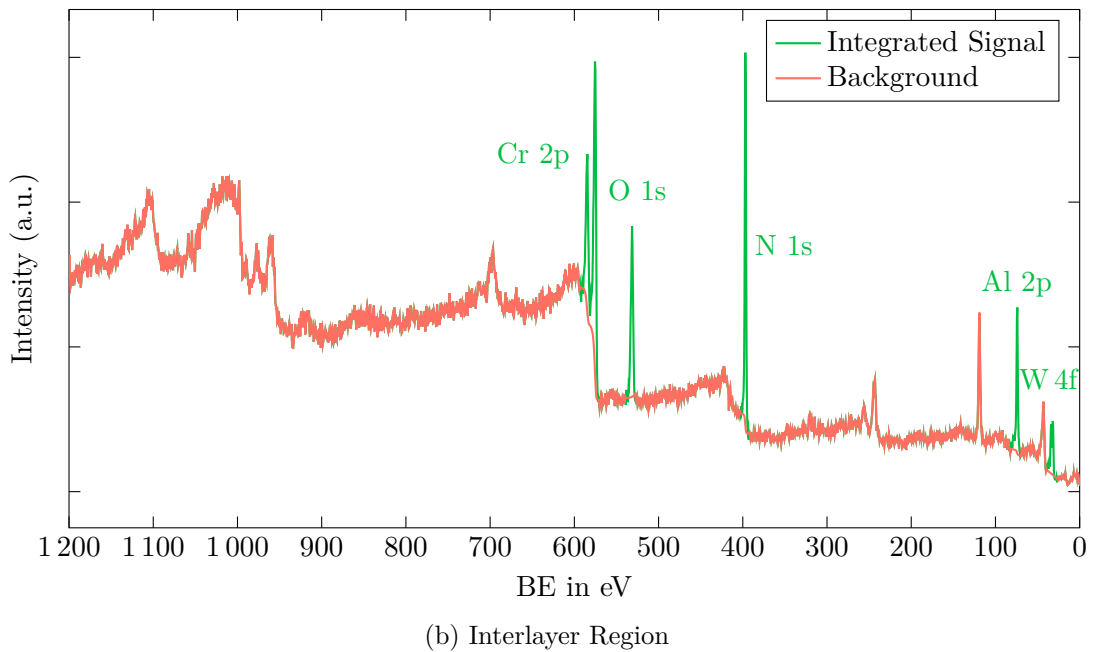
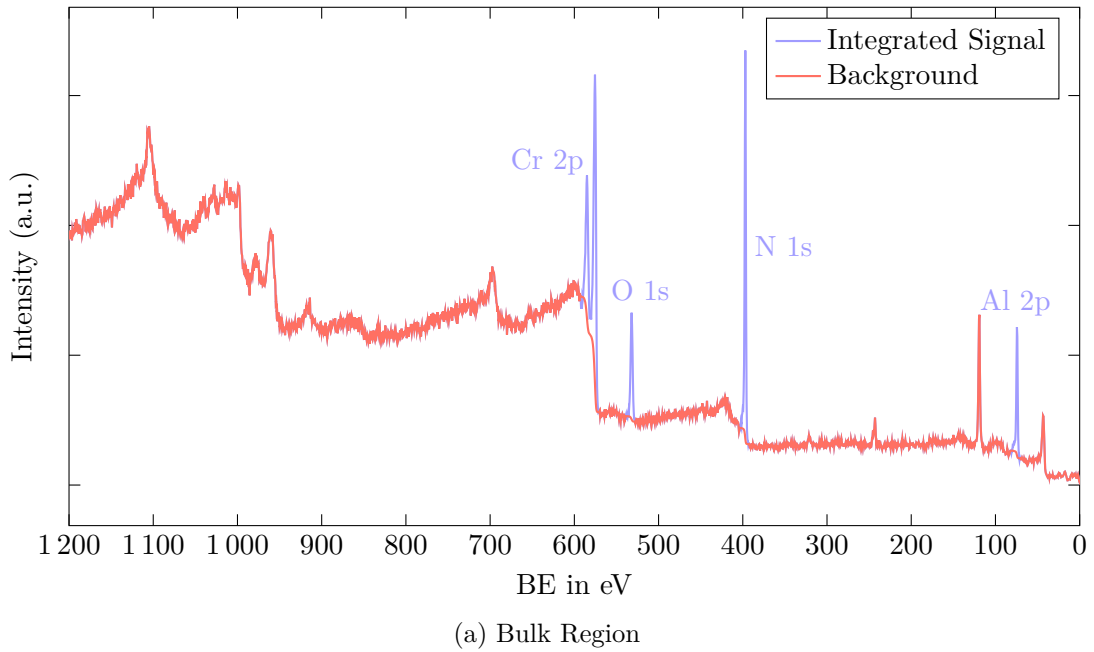


Figure 4.5: XPS Survey Scans of a sample with 70/30 coating and 90/10 interlayer. Both the bulk and interface region are displayed. The integrated peaks are from left to right: Cr 2p, O 1s, N 1s, Al 2p and W 4f (only visible in the interlayer region).

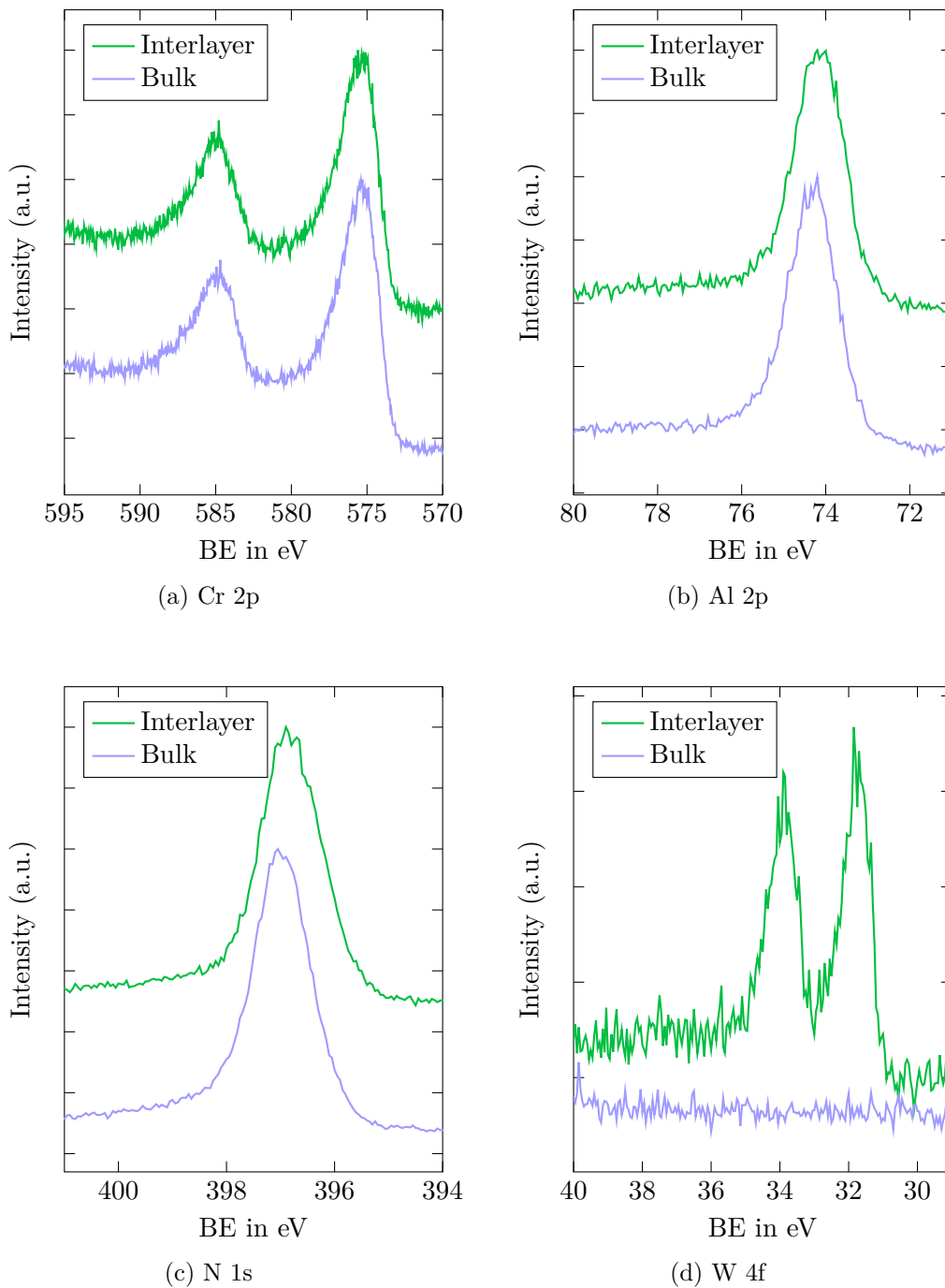


Figure 4.6: XPS region details for Cr, Al, N and W. All spectra have been normalized to their strongest signals.

the investigation was restricted to these four bases.

4.2.1 Alternative Leaching Agents

In Figure 4.7 BSE images of samples treated with different bases can be seen. The light areas are the WC-Co substrate, the dark areas the AlCrN coating (Z-contrast). A preliminary test showed that a 30 % NaOH solution reacts slower than a 50 % (saturated) solution. Therefore each base was deployed in saturated state to ensure the highest possible reaction speed. The de-coating times varied from 1-3 h. The displayed images were chosen in regard to the highest visual acuity to present the success of each base clearly. The expectation was an increase in de-coating speed from LiOH to CsOH according to their rising alkalinity. The results are differing greatly from this expectation. LiOH and CsOH did not react at all while NaOH and KOH are closely matched. In the case of KOH a larger area seems to be de-coated compared to NaOH, but it has to be noted that the reaction time for this sample was 50 % longer than for NaOH, which does not show in the additionally uncovered area. A comparable sample treated in NaOH for the same time was almost completely de-coated. Even if both bases worked equally well, Na^+ is the lighter counter ion and NaOH the cheaper substance overall, which is also important for the scale of an industrial process. The case of LiOH can be explained with the much lower solubility (≈ 5 mol/L) compared to NaOH (≈ 27 mol/L). However KOH and CsOH possess similar high solubilities (≈ 20 mol/L each) [20]. Furthermore CsOH showed no reaction even after 3 h despite similar solubility and higher alkalinity than KOH. Therefore the alkalinity cannot be the dominating requirement for the process. Instead, the ionic radii can explain the behaviour, which are 76 pm for Li^+ , 102 pm for Na^+ , 138 pm for K^+ and 167 pm for Cs^+ [45]. Radnai [46] showed that in concentrated $\text{Na}[\text{Al}(\text{OH})_4]$ solutions barely enough water exists to hydrate any ion, thus contact ion pairs are enforced, where each ion is partly hydrated and partly in contact with each other. In this constellation the ion size plays an important role in stabilizing dissolved Al-ions. Knowing this the performance of KOH and CsOH can be understood.

In light of these results a different approach was tried, namely mixtures of NaOH, KOH and NaCl in varying ratios. The idea was to combine the higher alkalinity of KOH with the presence of Na^+ ions to stabilize formed $[\text{Al}(\text{OH})_4]^-$ ions. A representative survey of the results can be seen in Figure 4.8. Pure NaOH was the reference again, which is showed in Figure 4.8(b). None of these mixtures performed comparably to pure NaOH, therefore the search for a better leaching agent failed. Again a possible explanation can be the solubility competition at high concentrations.

4.2.2 ICP-OES Analysis of Leaching Agents

Since NaOH was the only successful base the analysis with ICP-OES was constrained to it. In Figure 4.9 the linear calibration functions can be seen for the four analyzed elements. The signals were all normalized to the internal standard In. The correlation coefficient is excellent for all lines and the axis offset and the spread of blank signal are very small, resulting in low limits of detection (LOD). All four elements could be detected in the samples, but OES measurement of W is difficult under the chosen conditions which

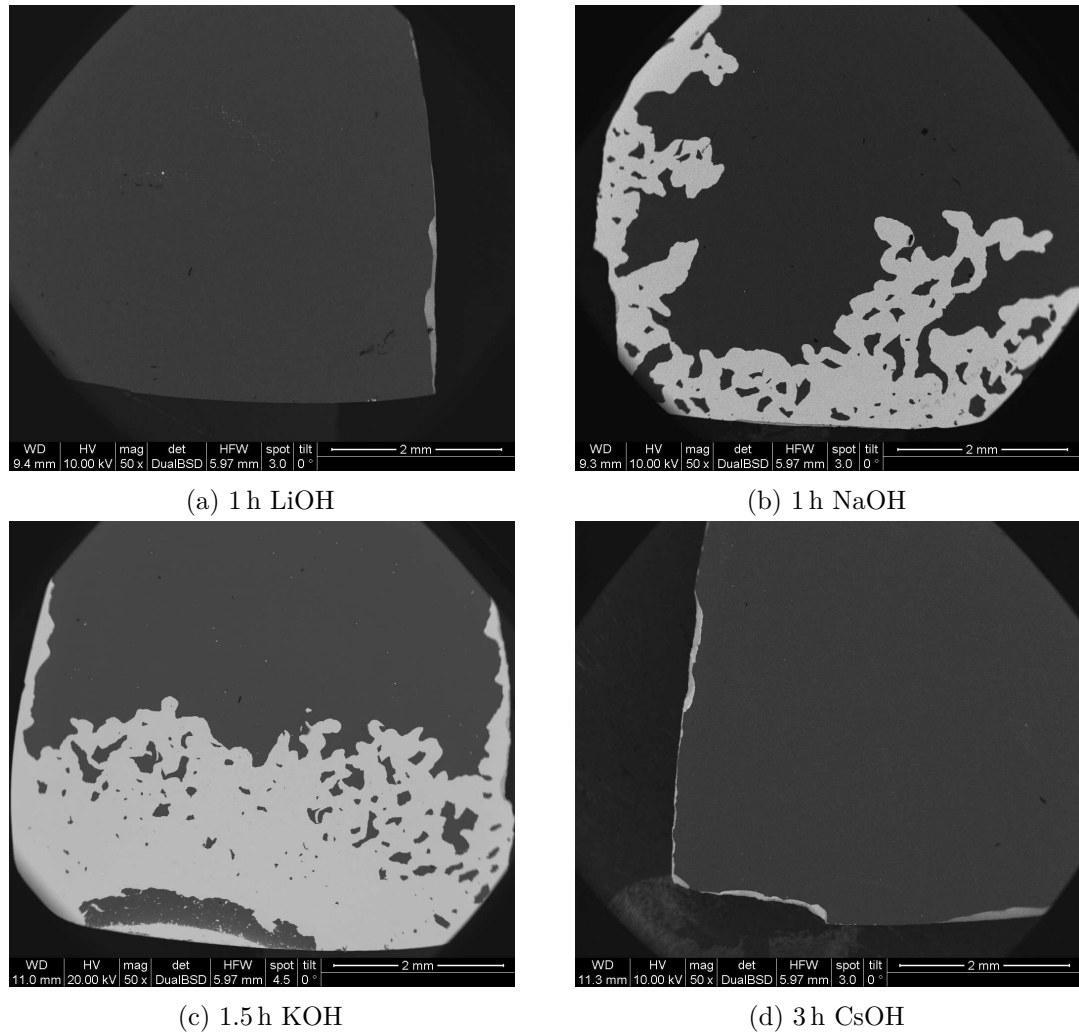


Figure 4.7: Comparison of different saturated bases regarding de-coating capability. The reaction was carried out at 140 °C for different times. Representative samples have been selected to show that no base works faster and cheaper than NaOH.

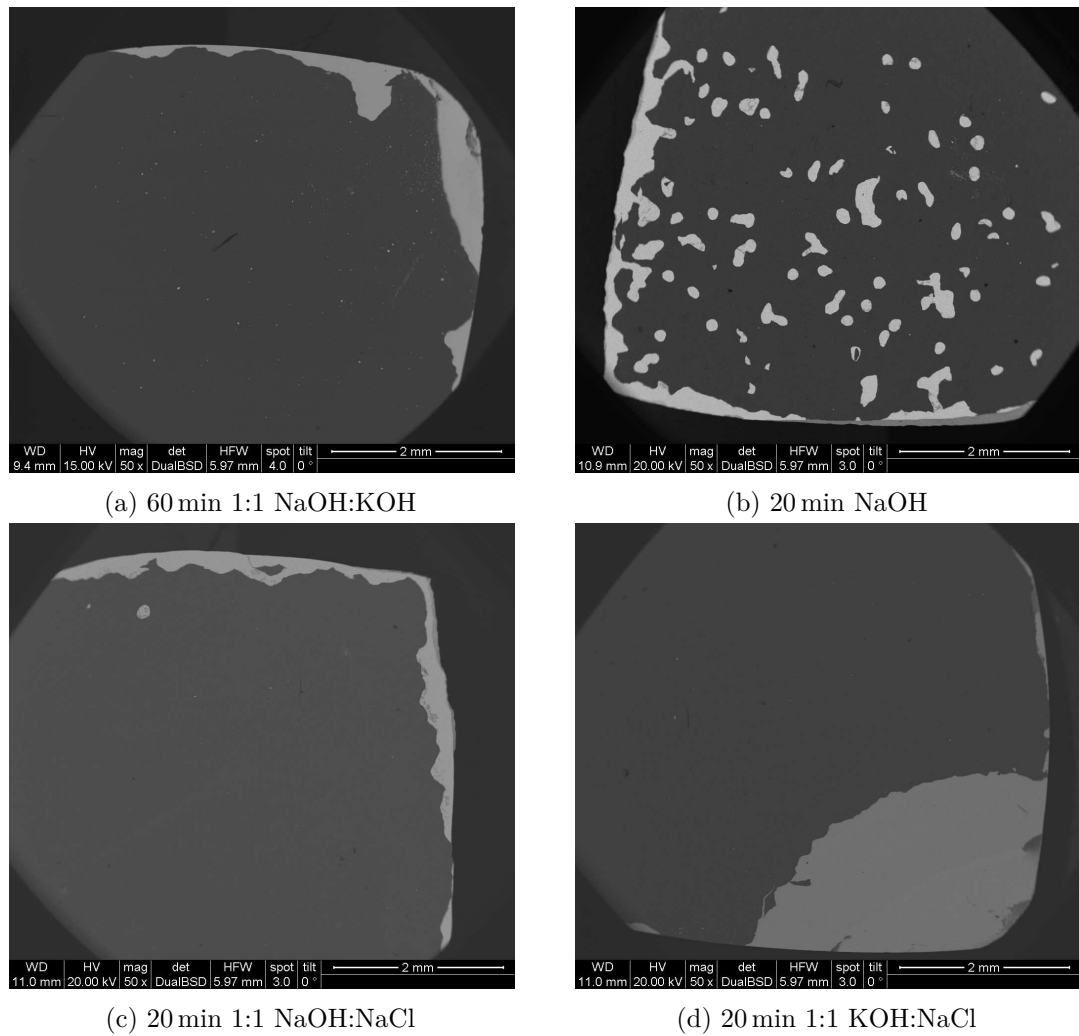


Figure 4.8: Comparison of base and salt mixtures with NaOH regarding de-coating capability. The reaction was carried out at 140 °C for different times. A part of the uncovered area in (d) was shielded during the coating process by the sample holder. None of these mixtures show comparable results to pure NaOH.

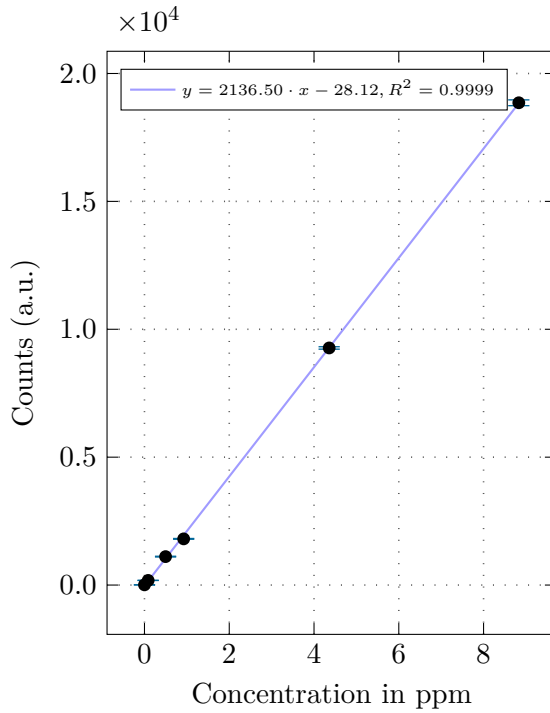
Table 4.2: Quantitative OES results for selected samples after 20 min de-coating time in NaOH. Sample 737 is a purely metallic coating (70/30 Al/Cr ratio), 738 is a pure 90/10 coating, 740 is a sample with metallic interlayer and insoluble coating above. All concentrations are given in ppm (mg/L).

Element	Al (mg/L)	Cr (mg/L)	Co (mg/L)	W (mg/L)	Al/Cr ratio (%)
LOD	0.004	0.028	0.010	0.235	
737	18.7±0.1	15.9±0.5	1.03±0.04	2.7±0.5	69.4/30.6
738	70.3±1.1	20.4±0.4	1.26±0.06	2.0±0.7	86.9/13.1
740	2.10±0.01	1.22±0.06	1.20±0.07	1.7±0.3	76.9/23.1

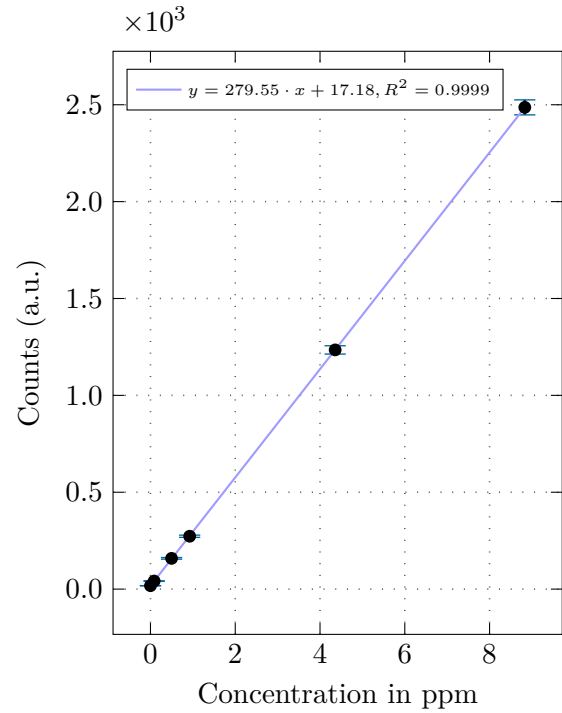
is reflected in the LOD that is two orders of magnitude higher than the LOD of Al. The analysis results for three representative samples are shown in Table 4.2 numerically and in Figure 4.10 graphically. Samples 737 (metallic 70/30 ratio) and 738 (hexagonal, 90/10 ratio) possessed entirely soluble coatings, while sample 740 contained only a soluble metallic interlayer underneath a standard 70/30 ratio ceramic coating. Note that the dissolved amount of Co and W is about the same for all samples, because their substrate amount was similar. All samples were treated for the same time of 20 min and the main difference between them is the amount of dissolved Al. The Al/Cr ratio depicted in Table 4.2 should give the same ratio for the samples 737 and 740, the slight deviation can be explained from two aspects. From the analytical viewpoint the relative standards deviation of 740's Cr signal is high compared to the other values since it is a low signal. This deviation can cause the estimation of dissolved Cr to be too low, affecting the ratio. The other explanation is the coating process by cathodic arc evaporation. Since the evaporation is partly effected through high temperature, the high difference in boiling points for the metals Al and Cr can cause the resulting vapor to be of different composition than the arcing target. This reason can also explain why sample 738 does not show the nominal concentration ratio of 90/10. The Co content is almost negligible, however there is some W dissolved in the NaOH. This is unwanted due to the desired selective nature of the process. W should withstand NaOH chemically, but in mining operations Wolframite ores, (Fe, Mn)WO₄, are treated with NaOH to produce soluble Na₂WO₄ [22]. A dissolution mechanism cannot be cleared here, but it might be possible that small amounts of WC could react with dissolved O₂ and NaOH under these high temperatures. In any case this confirms the need to establish a reaction path under milder conditions.

4.3 Influence of Changed Interlayer Composition

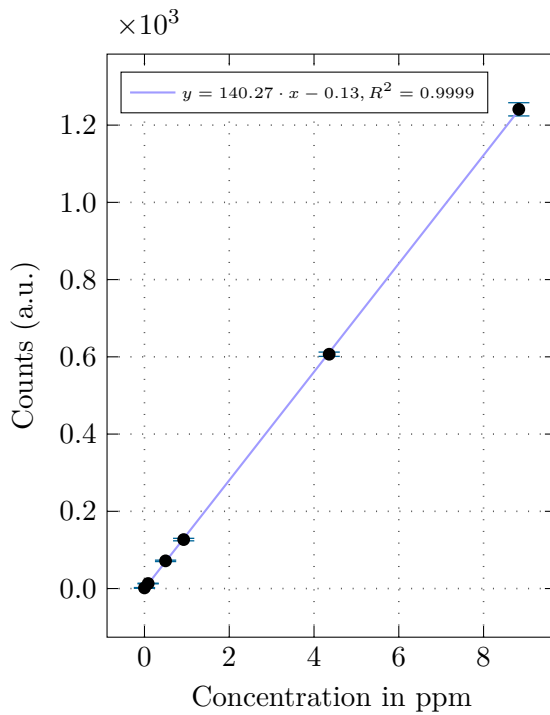
Samples with interlayers of different composition and structure were created to improve the performance compared to samples coated with sandblasted cathodes regarding dissolution speed. Their analysis is discussed in this chapter.



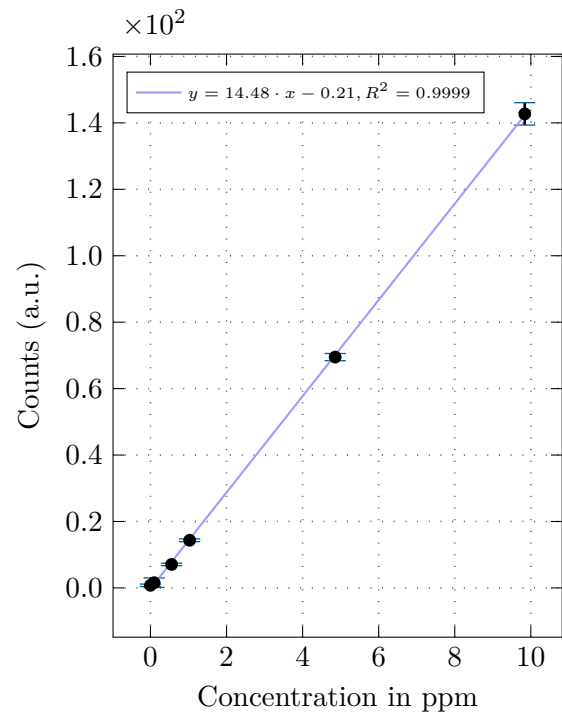
(a) Al at 239.152 nm



(b) Cr at 283.563 nm



(c) Co at 238.892 nm



(d) W at 239.709 nm

Figure 4.9: External ICP-OES calibrations for Al, Cr, Co and W.

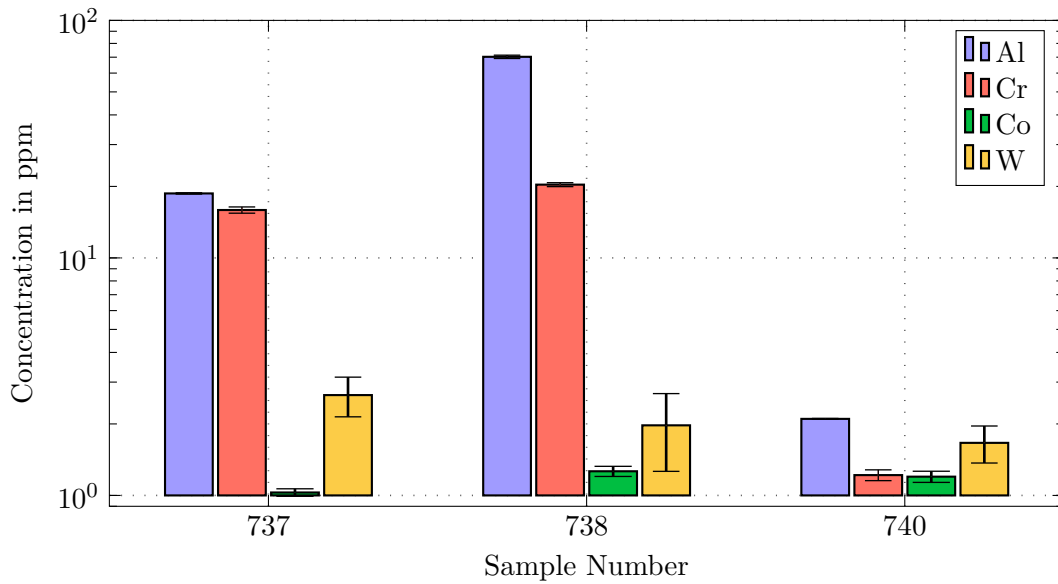


Figure 4.10: Metal concentrations in NaOH baths after 20 min de-coating time. 3 Samples are depicted: 737 is a purely metallic coating (70/30 Al/Cr ratio), 738 is a pure 90/10 coating, 740 is a sample with metallic interlayer and insoluble coating above.

4.3.1 Sandblasting Particle Size

Apart from the principal use of corundum to clean the target surface, the influence of different particle sizes was investigated. Figure 4.11 shows a comparison of samples coated after treating the arcing target with the two size classes "Fine" = 36-106 μm and "Coarse" = 300-425 μm . A possible explanation is the different surface morphology of the cathodes, with fine sand a higher surface area can be achieved. Since generated surface protrusions increase the field strength around them the arcing process can be enhanced. SIMS depth profiles were also measured, but no significant difference in the samples could be detected. Further research would have required investigations of the arcing targets themselves but they were not open for study because they are used frequently for other projects.

4.3.2 Oxidic Interlayer

Since SIMS measurements revealed the presence of oxygen at the interlayer, samples with oxidic interlayer were created by introducing 50-200 sccm O_2 for 1-5 min. However, none of these samples showed signs of de-coating. This does not mean that the SIMS depth profile is wrong, but a few explanations are feasible that limit this techniques usefulness in this case. The quantitative ion count in SIMS is highly dependent on matrix influences, therefore other chemical compositions at the interface can increase the ionization probability of the detected atoms and molecules. Therefore an interlayer composition changed in some specific way can simulate the oxygen presence. The other possibility is that oxygen is actually present after sandblasting the cathodes but takes no

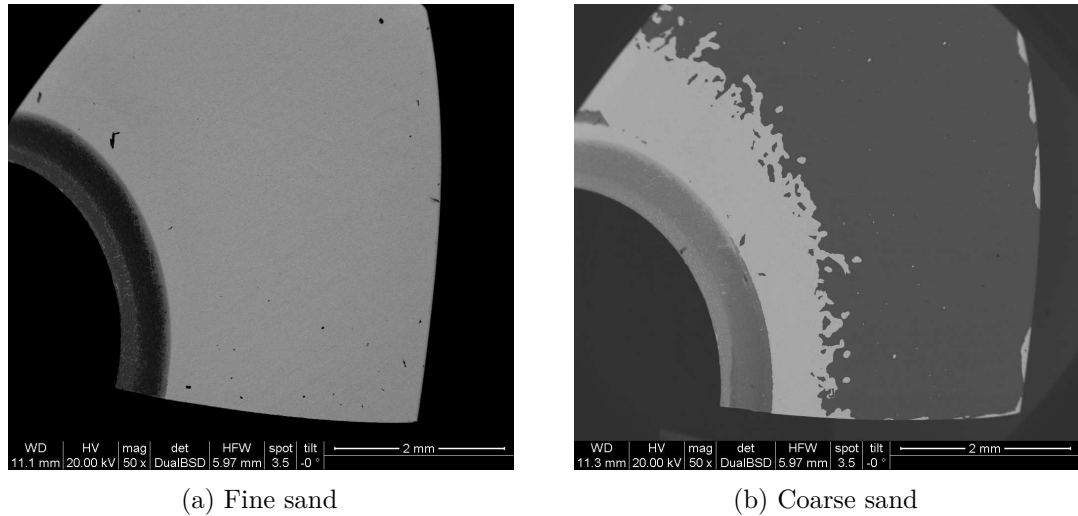


Figure 4.11: BSE images showing the influence of two different corundum particle size classes, "Fine" = 36-106 μm , "Coarse" = 300-425 μm , on de-coating speed.

major part in the stripping process. The samples with oxidic interlayer were therefore not investigated further.

4.3.3 Metallic Interlayer

As stated in subsection 2.1.3 Al is soluble in NaOH in its metallic state. The next step was therefore to create samples with metallic interlayer by introducing an inert Ar partial pressure of 300 sccm for the first 20 s-5 min. These samples exhibited a significantly increased de-coating speed. Since metallic coatings possess good adhesion but low mechanical resistance like hardness and tribological properties the influence of the interlayer on the whole coating needs to be as small as possible, meaning that the interlayer should show a minimal thickness. A too thin interlayer can impede the dissolution speed, likely due to diffusion barriers, therefore an optimum needs to be found. Table 4.12 shows an overview of four different samples with varying Ar durations and therefore interlayer thicknesses. The samples were treated in NaOH at 140 °C for 20, 30 and 45 min, the BSE images show the de-coating progress. It can easily be seen that the sample with 45 s Ar is the fastest in this process, fully stripped after 20 min. It possesses an interlayer thickness of ≈ 50 nm.

4.3.4 Hexagonal Interlayer

Another parameter that can be changed in the coatings is the crystal structure. By evaporating targets with 90/10 composition coatings with higher Al-content and Wurtzite structure can be obtained. The mechanical properties of this structure cannot compete with cubic AlCrN, but a preliminary test showed that this coating is soluble as a whole. Therefore samples with 90/10 interlayer underneath a cubic 70/30 coating were created. Again an optimum needed to be found like in subsection 4.3.3, the results can be seen in Table 4.13. Three Samples with a 90/10 cathode evaporation time of 1-5 min were etched

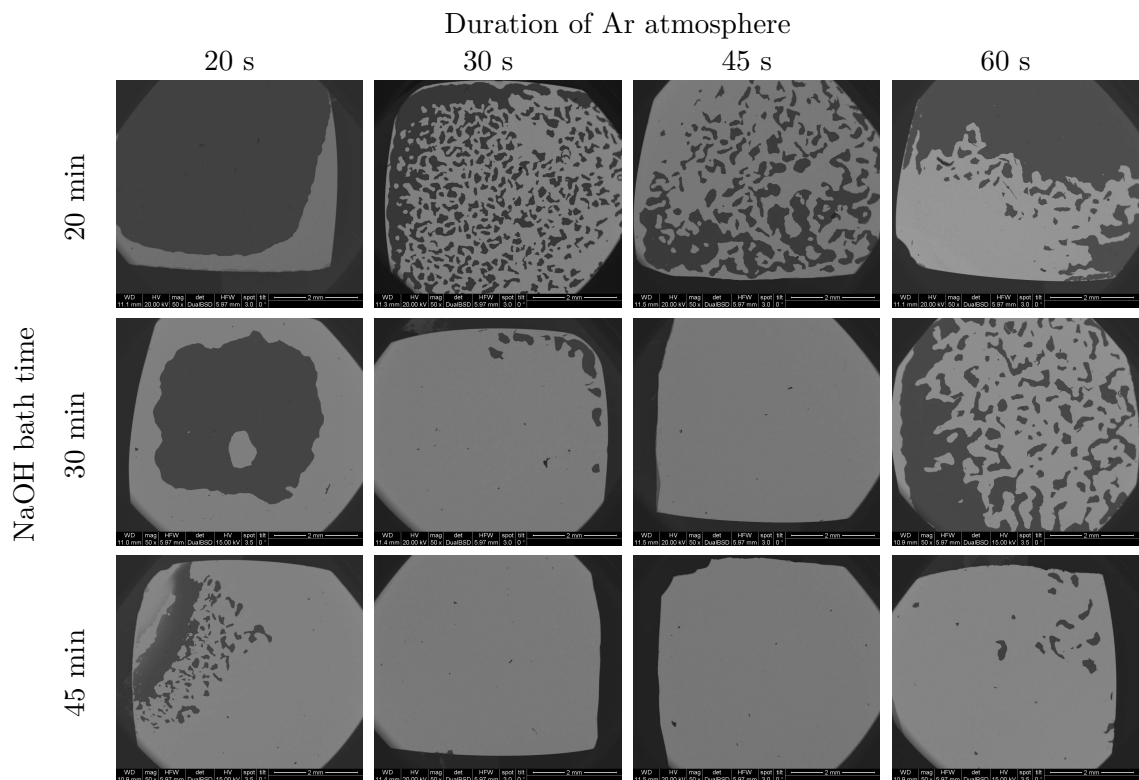


Figure 4.12: BSE images showing a comparison of metallic interlayer thicknesses regarding de-coating speed. The columns show the samples (20-60 s Ar atmosphere), the rows different bath times in 50 % NaOH. The optimal sample treated for 45 s in Ar atmosphere possesses an interlayer thickness of ≈ 50 nm.

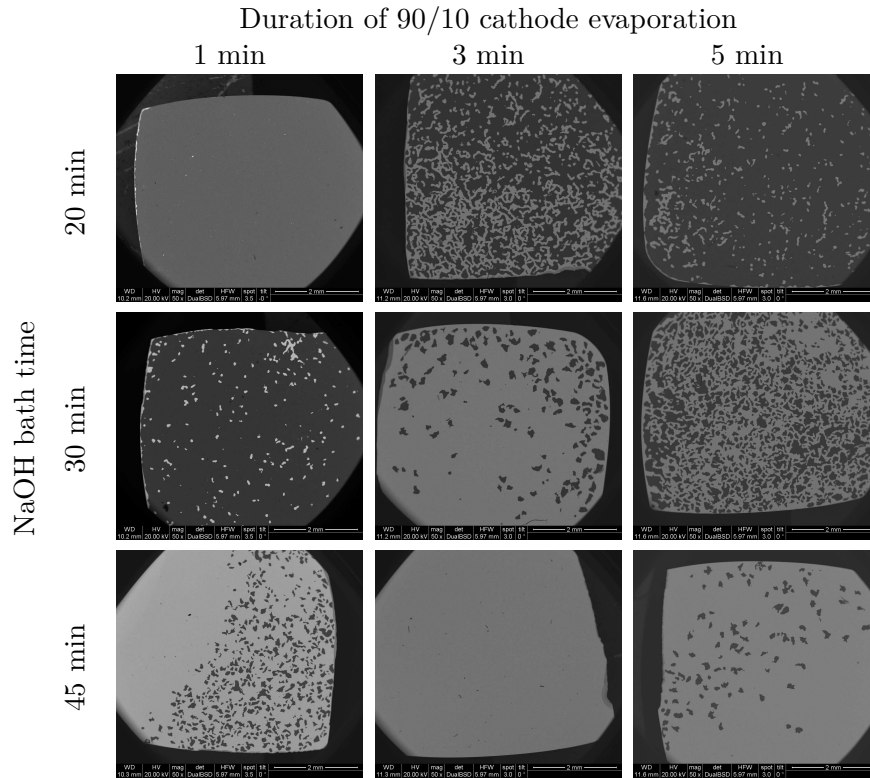


Figure 4.13: BSE images showing a comparison of hexagonal interlayer thicknesses regarding de-coating speed. The columns show the samples (90/10 cathode evaporated for 1-5 min), the rows different bath times in 50 % NaOH. The optimal sample created by evaporating a 90/10 cathode for 3 min possesses an interlayer thickness of ≈ 70 nm.

by NaOH for 20, 30 and 45 min like above. The BSE images show the stripping progress. The sample with 3 min evaporation time is dissolved the fastest, being completed after 45 min. It possesses an interlayer thickness of ≈ 70 nm. The de-coating is therefore a bit slower than with metallic interlayer but still a lot faster than with sandblasted cathodes. The slightly slower speed in comparison can be attributed either to the bonding state (metallic-ceramic) or the total Al concentration which is higher for the metallic (70 at%) than the 90/10 ceramic phase (45 at%). Since two viable paths that improve the de-coating procedure at 140 °C could be established, the next step was to reduce the temperature as low as possible while maintaining an acceptable reaction time. This is discussed in section 4.5.

4.4 Two Step Process

Since the search for a more efficient base was unsuccessful a different approach was tried. Samples with metallic interlayer were used for this step because they showed the fastest

base reaction. The coating system was first weakened in a kinetically controlled reaction using acids and oxidising agents, in the second step 50 % NaOH was used again to spall the coating off. The reaction time in the acid varied from 3-10 min, the temperature was set at 90 °C, to ensure a visible reaction if it is possible at all. The only exception was the 1:1 HNO₃:H₂O₂ mixture because it reacted vigorously even at room temperature, leading to bubble formation. For this reason the sample was also removed after just 3 min.

The stripping progress after the final 20 min in NaOH at 140 °C is displayed in Figure 4.14 for 1:1 HNO₃:H₂O₂, 1:1 HNO₃:H₂SO₄ and pure HCl, HNO₃ and H₂SO₄ compared to a control sample of the same type without acid treatment. The BSE images show a small increase in de-coated area for Figure 4.14(b), while all the other samples were completely de-coated after the 20 min. This is a great increase in speed compared to the sample without acid treatment. However, the HNO₃:H₂O₂ mixture showed that the selectivity of the process is a problem. The mass balance of the sample revealed that about 2.5 mg were lost, while a majority of the coating, which itself weighs only about 1 mg still remained on it. The mass balance of the other mixture, 1:1 HNO₃:H₂SO₄, showed the same problem to a lesser extent. Therefore the selectivity of the acids needed to be investigated. This was done in a long-term acid treatment test of uncoated substrates. A substrate plate was prepared like other samples and left in HCl, HNO₃ and H₂SO₄ for 3 h at 90 °C. The sample in HNO₃ was removed after 1 h because of the evolution of brown nitrous fumes, which indicate oxidation processes, and it had changed considerably. In Figure 4.15 SE and light microscopic images of these samples can be seen, Figure 4.15(c) is immediately striking. The SE image reveals small needles and cracks and the whole sample has gained a yellowish tint. EDX measurement revealed that the needles consist of WO₃, the most stable oxide that possesses this color. The samples treated in HCl and H₂SO₄ are almost unchanged. In the light microscope the samples look just like the untreated sample, the polished surface is reflective as before. Only the SEM reveals some very small pores, less than a μm in size, in the surface that are not present in the untreated plate.

Also the color of the acids changed considerably. A photo of them can be seen in Figure 4.16(b), HCl gained a bright blue color, while H₂SO₄ turned faintly pink. This needed clarification, therefore the HCl was analyzed by ICP-OES. The H₂SO₄ could not be analyzed because the substance is extremely high boiling and would therefore contaminate the instrument. With the expected low concentrations high dilutions were also impossible, however some insight can be gained from complex chemistry. In Figure 4.16(a) the metal analysis of the HCl is displayed. It shows that mainly Co was dissolved, while the other elements were barely present, W even under the detection limit. Since this sample was added to a measurement of bases quantified with HNO₃ standards, larger error margins have to be considered due to poor matrix matching. This Co concentration can also explain the color of the HCl, since it is the color of the [CoCl₄]²⁻ complex. The H₂SO₄ on the other hand is pink, a color corresponding to another Co complex: [Co(H₂O)₆]²⁺ [47]. It is therefore likely that both acids work in the same manner. Two different effects are possible, the acid could attack the defect structure of the coating, simplifying the access of the base in the second step. This process was experimentally not accessible however. Additionally surface Co atoms are dissolved from the substrate, this could weaken the adhesion of the coating and creating space for the NaOH at the same time, again making diffusion easier. In any case, this procedure is not strictly selective, however further tests

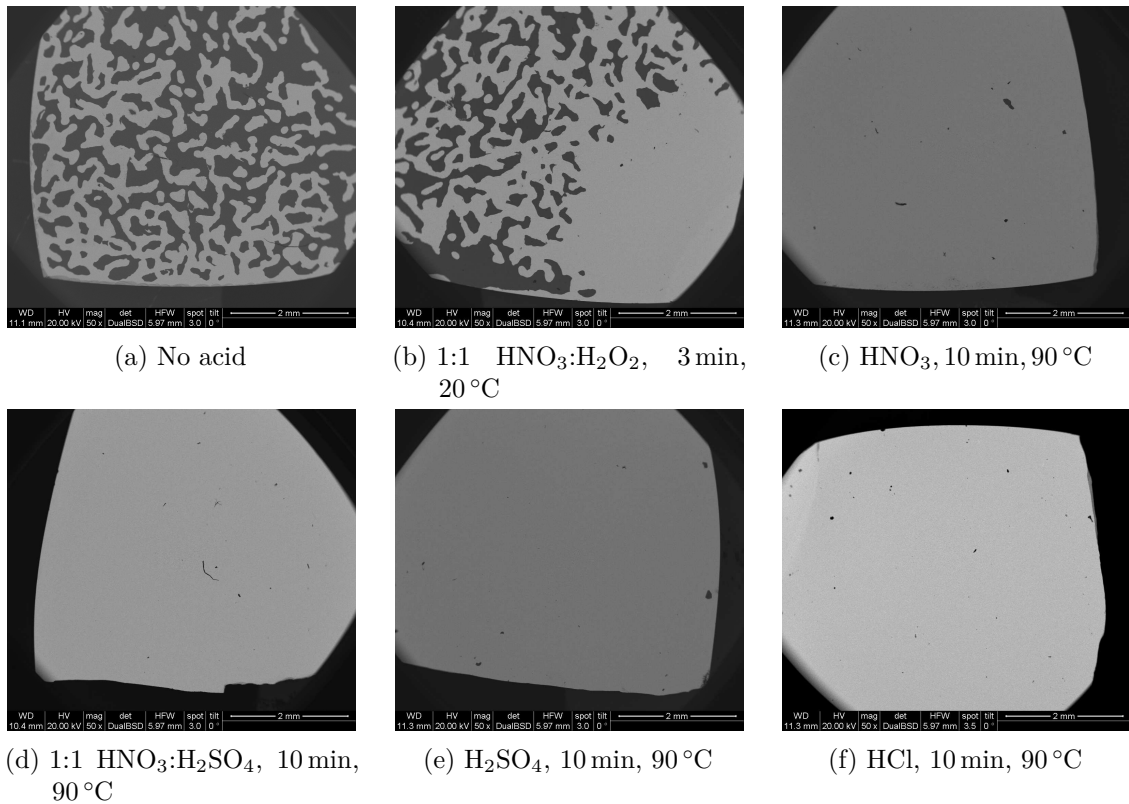


Figure 4.14: BSE images of samples with metallic interlayer after treatment in acid at the given temperature and time and subsequently in NaOH at 140 °C for 20 min. Samples (c)-(f) are completely de-coated.

showed, that the positive effect could be achieved with only 2 min acid treatment. In this short time span no statistically significant mass loss could be detected, it is therefore possible that the substrate attack is sufficiently slow.

Despite the success in reaction speed this procedure is not yet optimized to ensure the longevity of the substrate. Investigation towards the ability to re-coat the stripped substrates needs to be conducted.

4.5 Reaction at Reduced Temperature

Since different sample types showed improved stripping behaviour at the high temperature of 140 °C, reactions at reduced temperature are feasible as well. The size of the temperature-step was estimated with a thumb rule from the Arrhenius theory [48]:

$$k = A * e^{-\frac{E_a}{RT}} \quad (4.1)$$

where k is the rate constant, A the collision factor, E_a the activation energy, R the gas constant and T the temperature. From the exponential term a relationship can be derived,

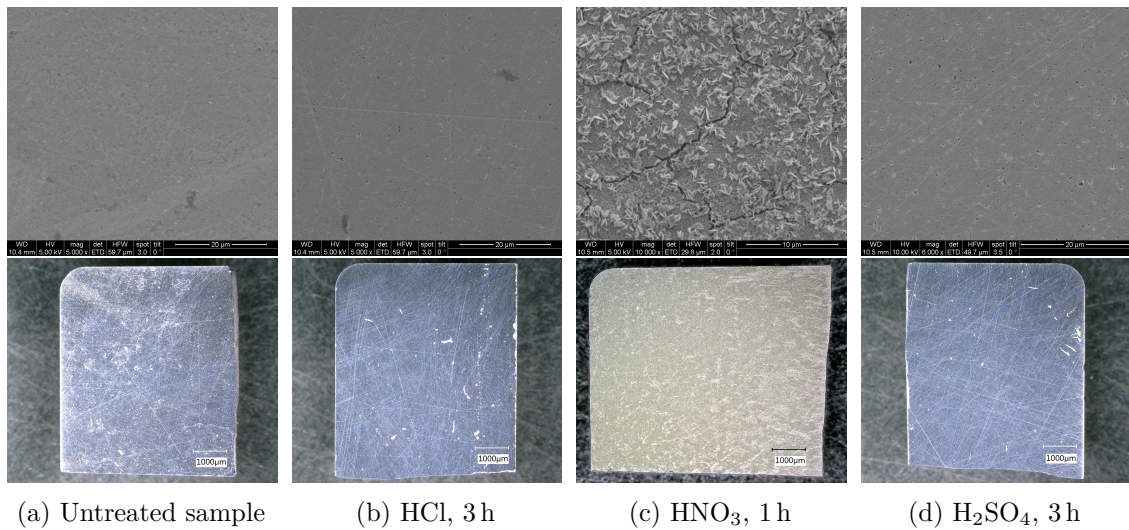
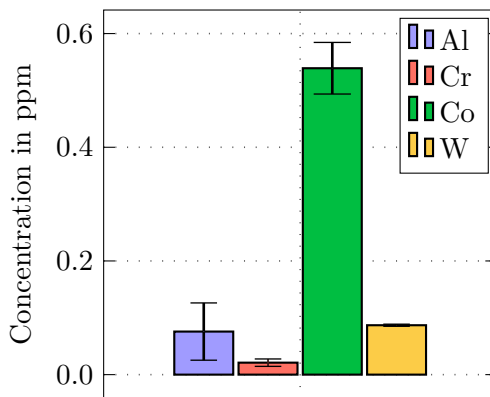
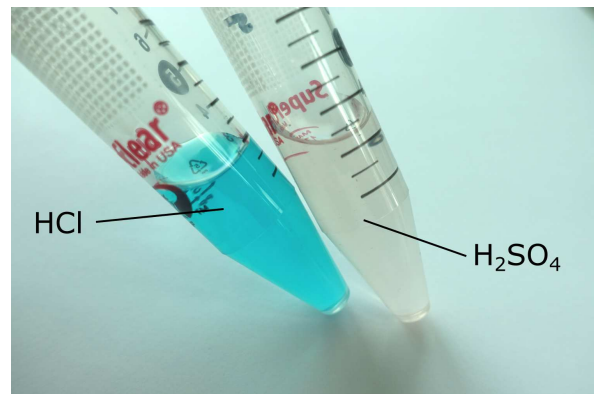


Figure 4.15: SE and light microscopic images of uncoated samples after long-term acid treatment at 90 °C. (b) and (d) show no significant changes on the surface, (c) has oxidized considerably.



(a) Metal concentration in HCl



(b) Photo of two acids after stripping treatment

Figure 4.16: (a) The ICP-OES analysis of HCl after 3 h at 90 °C shows mainly dissolved Co. Because of poor matrix matching with the standards larger error margins have to be considered. (b) The color of the same HCl and H₂SO₄ after 3 h at 90 °C match corresponding Co complexes.

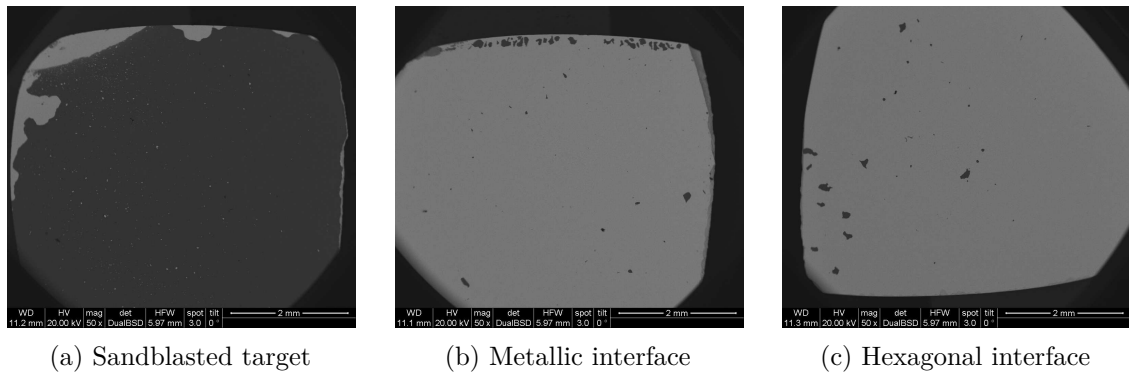


Figure 4.17: BSE images of three different sample types after 4 h reaction time in 50 % NaOH at 110 °C. The metallic and hexagonal interfaces exhibit vastly superior de-coating speed compared to sandblasting the cathode.

that a T -decrease by 10 °C should double the reaction time. By applying this rule to the dissolution optimization from section 4.3, it can be estimated that the de-coating should complete in 4 h at 110 °C, a time that is still acceptable. In Figure 4.17 a comparison of three different sample types can be seen, one each with a metallic and hexagonal interlayer and a control sample with sandblasted target. This makes clear that the new interlayer types are far superior to sandblasting the target.

An even further improvement could be achieved with the two-step process. From the same deliberations a possible T -decrease of 50 °C could be calculated. Table 4.18 shows the comparison of samples with metallic and hexagonal interface treated in HCl or H₂SO₄ for 2 min at 90 °C followed by 3 h in NaOH at the same temperature. This proves again that the metallic interface is dissolved slightly faster and also that the treatment with HCl works faster than with H₂SO₄, a fact that can also be deduced from the intensity of the acids colors.

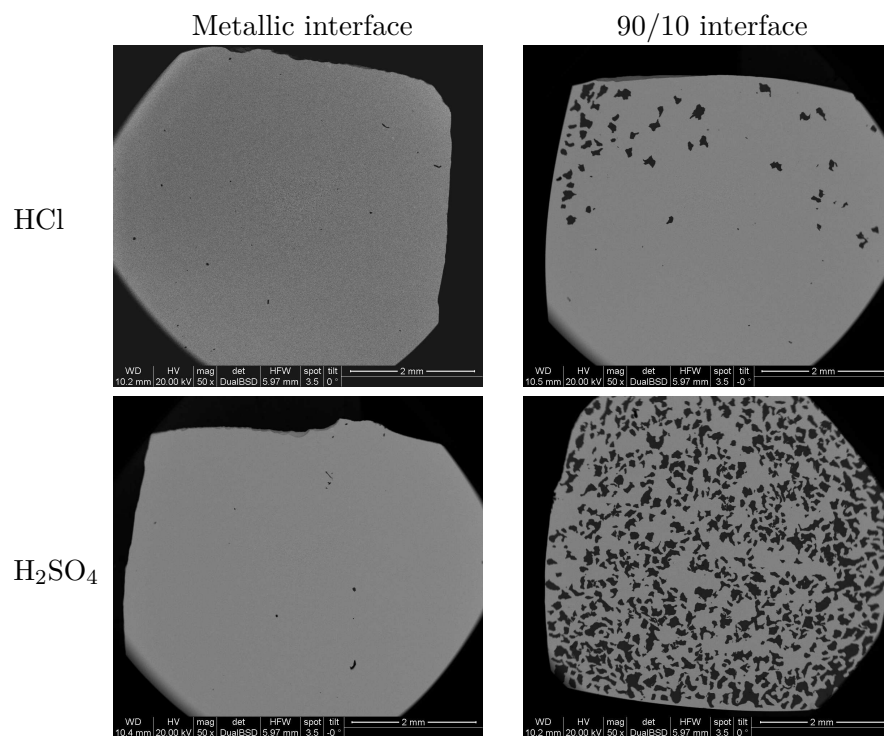


Figure 4.18: BSE images of samples with metallic and hexagonal interlayer after 2 min treatment in either HCl or H₂SO₄ at 90 °C followed by 3 h in 50 % NaOH at 90 °C.

5 Conclusion

To reduce the reaction temperature of the stripping process different paths have been investigated. One of them was the search for a better leaching agent, namely LiOH, KOH and CsOH, either as pure solution or as mixture, however none of them produced the desired results. NaOH was the fastest reactant in all cases. Of the several properties that stabilize Al as $[\text{Al}(\text{OH})_4]^-$ the most important one seems to be the ion radius of the cation that forms contact ion pairs in the concentrated solution. Mixtures of strong bases with other Na^+ containing substances were also unsuccessful, probably because of solubility competition. Lowering the concentration of pure NaOH impaired the reaction speed, therefore lower concentrations of other substances are not promising either.

The leaching agents were analysed with ICP-OES to determine the dissolved metal concentrations. The analysis of NaOH revealed that mainly Al and Cr are dissolved in the same ratio that prevails in the coating, leading to dissolved amounts of about 0.35 mg (Al) and 0.10 mg (Cr) in the case of completely soluble coatings. For samples with only a soluble interlayer the amounts were in the range of 5-10 ng, similar to Co and W in all cases. The Co concentration was always close to the limit of detection (LOD), therefore a selective attack can be assumed in this regard. W on the other hand was dissolved in slightly greater quantity, but these values have to be treated with respect to the sample mass. In the deployed base volume of 5 mL the metals amount to less than 10 ng, relating to the available sample mass of ≈ 1.5 g WC and ≈ 90 mg Co in each sample this is very little. On the other hand about the same mass of Al and Cr is dissolved from the interlayer, which possesses a thickness of only a few nm and therefore a mass in the ng-range. Thus it can be assumed to be completely dissolved. The attack was therefore not strictly selective, but to a tolerable extent. Still, to ensure increased longevity of the expensive tools, milder reaction conditions are desired.

The structure and composition of the interlayer responsible for successful stripping was varied by sandblasting the arcing target with different corundum particle sizes, introducing Ar or O_2 into the coating chamber, or evaporating cathodes with a higher Al content (90/10 instead of 70/30). This resulted in interlayers with increased droplet concentrations, metallic/oxidic composition or hexagonal structure.

The interlayer was investigated with SEM, TEM, SIMS and XPS to understand the dissolution behaviour of the different coating types. This investigation was partly successful. The SEM and TEM images provide valuable insights to the interlayer composition and morphology and allow the understanding of the de-coating process. With HR-TEM the interlayer could be observed directly, allowing structural investigation, while a lower magnification showed large droplets in the interlayer created by sandblasting the arcing target. An EDX line-scan of such a droplet revealed a largely metallic composition, the dissolution speed of metallic interlayers seems to indicate that this is the key to solubility.

SIMS depth profiles were recorded through whole coatings to determine changes in

chemical composition with analyse depth. The method was suitable to detect a change in the interlayer region, however the correct interpretation is difficult since sandblasting the arcing target yielded roughly the same change in signals as a metallic interlayer although they are chemically and structurally different.

The interlayer characterization was also tested with XPS, however the sample preparation method was inadequate. The samples were prepared with an angular cut that should reveal the interlayer and bulk region next to each other. The analysis is incomplete because only one sample could be prepared successfully. The investigation of a sample with 90/10 interlayer revealed no chemical shift and thus the same bonding characteristics between the cubic and hexagonal structure. The quantitative comparison of interlayer and bulk region also suggests an oxygen- and nitrogen-gradient in the interlayer, though careful interpretation is needed, since the sputter preparation can influence the distribution of contaminations. Further studies with a different sample preparation method need to be conducted to gain definite findings, but it could be shown that XPS is a promising candidate for interlayer characterization.

The changed interlayer compositions yielded very promising results. The particle size of corundum used for sandblasting has a major effect on the reaction speed, where small particles are beneficial for dissolution. This is likely due to different created surface roughness that influences the arcing behaviour during deposition.

Samples with oxidic interlayer were not de-coatable despite what SIMS results seem to indicate. The presence of oxygen could be tolerable but it is definitely not the determining component. Caution needs to be advised when interpreting SIMS data.

The samples with metallic and hexagonal interlayer were a full success. Not only do they make the manual sandblasting superfluous but they also exhibit much faster dissolution speeds. The metallic interlayer was dissolved in a shorter time but both routes are viable. The preference can therefore be made dependent on other properties of the interlayer like adhesion or hardness. With these samples the reaction temperature could be decreased by 30 °C while maintaining a stripping time of 4 h.

As an alternative reaction path a two step process was developed, where the samples were first treated in acid, followed by the stripping in NaOH. The establishment of this process was also successful, though some refinement could be favourable. By first treating the samples in HCl or H₂SO₄ for 2 min at 90 °C the reaction temperature in NaOH could be decreased by 50 °C with 3 h reaction time. The mechanism behind this is likely a slight removal of Co from the substrate surface as ICP-OES showed, enabling NaOH easier access to the interlayer. In regard to choosing a suitable acid it could be shown that oxidising agents like HNO₃ are not an option in terms of selectivity.

6 Outlook

There are two points that need further investigation. The XPS study of the interlayer could not be completed since only one of the four samples were prepared successfully. Clarifying the chemical composition and bonding state could help understand the dissolution behaviour of the different interlayer types. The angular cut was problematic since the hard coating made the rigid fixation of the sample while grinding difficult. A planar cut would require very much effort as well since a very thin region under a relatively large coating needs to be found precisely. Also because of the limited sample number this was not tried. Instead a repeated research would require new samples that consist of the interlayer and a thin coating of maximal 100 nm on top of it to protect the thin interlayer from contamination and also to measure differences between bulk and interlayer material.

The other procedure that needs optimization is the two step process. While a significant increase in reaction speed could be achieved in this thesis there might be other options that are even more beneficial. Next to a greater variety of acids and other substances different temperature levels and times should be tested to ensure minimal substrate attack. Also investigating the ability to re-coat these substrates has not been conducted and should be clarified.

Bibliography

- [1] R. Kieffer and F. Benesovsky, *Hartmetalle*. Springer-Verlag, 2013.
- [2] J. A. Ober, *Mineral commodity summaries 2018*, Mar. 10, 2018. [Online]. Available: <https://minerals.usgs.gov/minerals/pubs/mcs/2017/mcs2017.pdf>.
- [3] (Mar. 2014), European Commission, [Online]. Available: <http://trade.ec.europa.eu/doclib/press/index.cfm?id=1050>.
- [4] (Sep. 2016), [Online]. Available: <https://www.washingtonpost.com/graphics/business/batteries/congo-cobalt-mining-for-lithium-ion-battery/?noredirect=on>.
- [5] (May 2018), [Online]. Available: <https://tradingeconomics.com/commodity/cobalt>.
- [6] W. Schedler, *Hartmetall für den Praktiker. Aufbau, Herstellung, Eigenschaften und industrielle Anwendung einer modernen Werkstoffgruppe*. VDI-Verlag Düsseldorf, 1988, ISBN: 3-18-400803-7.
- [7] A. Anders, *Cathodic Arcs*. Springer-Verlag GmbH, Sep. 23, 2008, ISBN: 978-0-387-79107-4.
- [8] P. Mayrhofer, R. Rachbauer, D. Holec, F. Rovere, and J. Schneider, “Protective transition metal nitride coatings,” in *Comprehensive Materials Processing*, 14, vol. 4, Elsevier, 2014, pp. 355–388.
- [9] (Jun. 2018), [Online]. Available: [http://gestis-en.itrust.de/nxt/gateway.dll/gestis_en/000000.xml?f=templates\\$fn=default.htm\\$vid=gestiseng:sdbeng\\$3.0](http://gestis-en.itrust.de/nxt/gateway.dll/gestis_en/000000.xml?f=templates$fn=default.htm$vid=gestiseng:sdbeng$3.0).
- [10] Institute of Materials Science and Technology, TU Wien, Getreidemarkt 9 | 1060 Wien, <https://www.tuwien.ac.at/EN/>.
- [11] (Jun. 2018), Oerlikon Balzers, [Online]. Available: <https://www.oerlikon.com/balzers/com/en/portfolio/equipment/innoventa-mega-innova-ingenia/innova/>.
- [12] A. Reiter, V. Derflinger, B. Hanselmann, T. Bachmann, and B. Sartory, “Investigation of the properties of all-xCr_xN coatings prepared by cathodic arc evaporation,” *Surface and Coatings Technology*, vol. 200, no. 7, pp. 2114–2122, Dec. 2005.
- [13] P. H. Mayrhofer, C. Mitterer, L. Hultman, and H. Clemens, “Microstructural design of hard coatings,” *Progress in Materials Science*, vol. 51, no. 8, pp. 1032–1114, Nov. 2006.

- [14] H. Willmann, P. Mayrhofer, P. Persson, A. Reiter, L. Hultman, and C. Mitterer, "Thermal stability of al-cr-n hard coatings," *Scripta Materialia*, vol. 54, no. 11, pp. 1847–1851, Jun. 2006.
- [15] H. Willmann, P. H. Mayrhofer, L. Hultman, and C. Mitterer, "Hardness evolution of al-cr-n coatings under thermal load," *Journal of Materials Research*, vol. 23, no. 11, pp. 2880–2885, Nov. 2008.
- [16] E. Arzt, "Size effects in materials due to microstructural and dimensional constraints: A comparative review," *Acta Materialia*, vol. 46, no. 16, pp. 5611–5626, Oct. 1998.
- [17] V. Voitovich, V. Sverdel, R. Voitovich, and E. Golovko, "Oxidation of WC-co, WC-ni and WC-co-ni hard metals in the temperature range 500–800 °c," *International Journal of Refractory Metals and Hard Materials*, vol. 14, no. 4, pp. 289–295, Jan. 1996.
- [18] S. Basu and V. Sarin, "Oxidation behavior of WC-co," *Materials Science and Engineering: A*, vol. 209, no. 1-2, pp. 206–212, May 1996.
- [19] M. Kawate, A. K. Hashimoto, and T. Suzuki, "Oxidation resistance of cr1-XAlXN and ti1-XAlXN films," *Surface and Coatings Technology*, vol. 165, no. 2, pp. 163–167, Feb. 2003.
- [20] W. M. " H. David R. Lide, Ed., *CRC Handbook of Chemistry and Physics*, 90th ed., 35. American Chemical Society, Sep. 2009, vol. 131, pp. 12 862–12 862, ISBN: 978-1-4200-9084-0.
- [21] M. Binnewies, M. Finze, M. Jäckel, P. Schmidt, and H. Willner, *Allgemeine und Anorganische Chemie*. Springer-Verlag GmbH, Dec. 22, 2016, ISBN: 978-3-662-45066-6.
- [22] A. F. Holleman and E. Wiberg, *Lehrbuch Der Anorganischen Chemie, 91-100: Verbesserte Und Stark Erweiterte Auflage Von Nils Wiberg*. De Gruyter, 1984, ISBN: 3-11-007511-3.
- [23] U. Knoblich, "Entfernung von chromnitridschichten von wc-co - hartmetall," Master's thesis, Technische Universität Wien, May 2005.
- [24] D. M. Mattox, *Handbook of Physical Vapor Deposition (PVD) Processing*. William Andrew Publishing, Apr. 29, 2010, 792 pp., ISBN: 978-0-81-552037-5.
- [25] X. Hou and B. T. Jones, "Inductively coupled plasma/optical emission spectrometry," *Encyclopedia of analytical chemistry*,
- [26] S. J. Hill, Ed., *Inductively Coupled Plasma Spectrometry and its Applications*. Wiley-Blackwell, 2007, ISBN: 978-1-4051-3594-8.
- [27] D. A. Skoog, F. J. Holler, and S. R. Crouch, *Instrumentelle Analytik*. Springer-Verlag GmbH, Dec. 6, 2013, ISBN: 978-3-642-38169-0.
- [28] J. Goldstein, D. Newbury, D. Joy, J. Michael, and N. W. M. Ritchie, *Scanning Electron Microscopy and X-Ray Microanalysis*. Springer-Verlag GmbH, Nov. 18, 2017, ISBN: 978-1-4939-6674-5.
- [29] *Quanta training course*, FEI Company, Feb. 2005.

- [30] (Jun. 2018), [Online]. Available: https://upload.wikimedia.org/wikipedia/commons/0/0d/Schema_MEB_%28en%29.svg.
- [31] H. Bethe, “Zur theorie des durchgangs schneller korpuskularstrahlen durch materie,” *Annalen der Physik*, vol. 397, no. 3, pp. 325–400, 1930.
- [32] R. W. “Electron backscattering as a function of atomic number,” in *Proceeding 6th International Cong x-ray optics and microanalysis*. University of Tokyo Press, Tokyo, p 121, Shinoda G, Kohra K, Ichinokawa T, 1972.
- [33] N. E. David Bell, *Low Voltage Electron Microscopy: Principles and Applications*. John Wiley & Sons Inc, Feb. 11, 2013, 218 pp., ISBN: 111997111X.
- [34] (Jun. 2018). X-ray data booklet, Lawrence Berkeley National Laboratory, [Online]. Available: http://xdb.lbl.gov/Section1/Sec_1-3.html.
- [35] C. Fiori and D. Newbury, “Artifacts observed in energy dispersive x-ray spectrometry in the scanning electron microscope,” *Scanning Electron Microscopy*, vol. 1, no. 1978, p. 401, 1978.
- [36] (Jun. 2018), Oxford instruments, [Online]. Available: <https://nano.oxinst.com/>.
- [37] D. B. Williams and C. B. Carter, “The transmission electron microscope,” in *Transmission Electron Microscopy*, Springer US, 1996, pp. 3–17.
- [38] A. M. Belu, D. J. Graham, and D. G. Castner, “Time-of-flight secondary ion mass spectrometry: Techniques and applications for the characterization of biomaterial surfaces,” *Biomaterials*, vol. 24, no. 21, pp. 3635–3653, Sep. 2003.
- [39] (Jun. 2018), [Online]. Available: https://www.iontof.com/download/IONTOF_TOF-SIMS_5_Brochure.pdf.
- [40] P. van der Heide, *X-ray Photoelectron Spectroscopy*. John Wiley & Sons Inc, Jan. 27, 2012, 264 pp., ISBN: 978-1-118-06253-1.
- [41] M. Grasserbauer, H. Dudek, and M. F. Ebel, *Angewandte Oberflächenanalyse mit SIMS Sekundär-Ionen-Massenspektrometrie AES Auger-Elektronen-Spektrometrie XPS Röntgen-Photoelektronen-Spektrometrie (German Edition)*. Springer, 1986, ISBN: 3-540-15050-1.
- [42] J. D. Andrade, “X-ray photoelectron spectroscopy (XPS),” in *Surface and Interfacial Aspects of Biomedical Polymers*, Springer US, 1985, pp. 105–195.
- [43] (Jun. 2018), [Online]. Available: <http://www.rowbo.info/XPS.html>.
- [44] (Jun. 2018), Federation of European Producers of Abrasives, [Online]. Available: <https://www.fepa-abrasives.com/>.
- [45] R. D. Shannon, “Revised effective ionic radii and systematic studies of interatomic distances in halides and chalcogenides,” *Acta Crystallographica Section A*, vol. 32, no. 5, pp. 751–767, Sep. 1976.
- [46] T. Radnai, P. M. May, G. T. Hefter, and P. Sipos, “Structure of aqueous sodium aluminate solutions: a solution x-ray diffraction study,” *The Journal of Physical Chemistry A*, vol. 102, no. 40, pp. 7841–7850, Oct. 1998.

- [47] J. Clark. (Jun. 2018). The colours of complex metal ions, [Online]. Available: <https://www.chemguide.co.uk/inorganic/complexions/colour.html>.
- [48] G. Wedler, *Lehrbuch der Physikalischen Chemie (German Edition)*. Wiley-VCH, 2005, ISBN: 3-527-31066-5.

List of Figures

2.1	Schematic overview of the Inductively Coupled Plasma - Optical Emission Spectroscopy with a liquid sampling system, an Echelle-monochromator and a CID-Array detector. Adapted from [26]	8
2.2	Schematic of a Meinhard-nebuliser. Adapted from [27]	9
2.3	A cyclone spray chamber. The vapor enters from the side, the top exit leads to the torch, the bottom exit into the waste. [26]	10
2.4	Schematic of an ICP-torch. H signifies the magnetic field lines. Adapted from [27]	11
2.5	Schematic of an optical grating. α and β are the angles of incident and diffracted light to the gratings perpendicular, d is the gratings spacing. Adapted from [26]	13
2.6	Schematic of an Echelle monochromator. In this setup a Schmidt-Cross-disperser replaces the prism for UV light to improve UV-transmission. Adapted from [27]	13
2.7	Work cycle of a charge induced device. a Generation and integration of charges by absorption of photons b Measurement of U_1 c Measurement of U_2 d Charge removal. State c can be transformed into state a or d , allowing destructive or non-destructive measurement. Adapted from [27] .	15
2.8	Schematic overview of the Scanning Electron Microscope. [30]	16
2.9	Monte Carlo simulation of 25 trajectories in Cu. The blue trajectories are absorbed by the material while the red trajectories leave the sample as backscattered electrons. [28]	19
2.10	Fit of Backscatter coefficient η as a function of atomic number Z (Equation (2.12)). [32]	20
2.11	BSE detector schematic. The dotted lines mark the solid angle Ω , the blue lines the elevation angle Ψ . Adapted from [28]	21
2.12	Energy distribution of emitted electrons. In a SEM the SE and BSE fraction can be measured. [33]	23
2.13	Geometric explanation of the secondary electron yield increase with increasing tilt angle θ . The yellow area signifies the region within the escape depth s_{esc} . [28]	24
2.14	ETD-Detector schematic. The dotted lines mark the solid angle Ω , the blue line the elevation angle Ψ . [28]	25
2.15	Different sources of SE, that contribute to the ETD-image. Red lines represent SE-trajectories, blue lines BSE-trajectories. SE_1 are generated directly at the beam impact, SE_2 are generated by exiting BSE further away, SE_3 are generated by BSE when hitting parts of the specimen chamber. [28]	25
2.16	Schematic diagram of the process of X-ray generation. [28]	26

2.17	Fluorescence yield versus atomic number. The displayed L line represents the average of the L ₁ , L ₂ and L ₃ lines, which differ by less than 10 % over most of the periodic table. [34]	28
2.18	Schematic of the silicon drift detector (SDD). A field gradient applied to the electrode rings (grey) "drifts" the free charges generated in the active detector volume (light blue) to the anode (blue) for collection. The charge is converted into a voltage by a field effect transistor (FET). [36]	30
2.19	Voltage ramp created by the FET preamplifier. X-ray photons appear as steps in the linear ramp that is reset periodically. [36]	30
2.20	Schematic of the possible interactions in a transmission electron microscope. [37]	31
2.21	Schematic of a time of flight - secondary ion mass spectrometer. [39]	33
2.22	Schematic of an x-ray photoelectron spectroscope with concentric hemispherical analyzer. Adapted from [43]	35
3.1	Image of two substrate plates. The dark grey area stems from the AlCrN coating, the light grey corners are the cemented carbide substrate that was covered by the substrate holder during coating.	39
3.2	Microscopic view of a cemented carbide sample before and after cutting.	39
3.3	Schematic of the sample preparation method for XPS analysis.	43
4.1	SE images of two partly de-coated samples, one with all three bias voltages and one with only -40 V. In (a) the two sublayers corresponding to the -40 V and -150 V bias voltage are visible. When using only -40 V, this subdivision does not exist. Also, in (b) the spallation of the coating from the substrate can be seen.	45
4.2	The coating system investigated by SEM/EDX. The BSE image shows the transition from the coating (dark) to the substrate (light), exemplary EDX-spectra of both phases are displayed in addition. The ordinate depicts the count rate, the abscissa the photon energy in keV. Only the most important W peaks are labeled.	45
4.3	SIMS depth profiles for samples with and without sandblasted cathodes.	46
4.4	TEM analysis of the interlayer. A HR-TEM image of an interlayer can be seen in (a). (b) and (c) show samples without and with sandblasted cathodes. An EDX line-scan of a droplet is shown in (d).	48
4.5	XPS Survey Scans of a sample with 70/30 coating and 90/10 interlayer. Both the bulk and interface region are displayed. The integrated peaks are from left to right: Cr 2p, O 1s, N 1s, Al 2p and W 4f (only visible in the interlayer region).	50
4.6	XPS region details for Cr, Al, N and W. All spectra have been normalized to their strongest signals.	51
4.7	Comparison of different saturated bases regarding de-coating capability. The reaction was carried out at 140 °C for different times. Representative samples have been selected to show that no base works faster and cheaper than NaOH.	53

4.8	Comparison of base and salt mixtures with NaOH regarding de-coating capability. The reaction was carried out at 140 °C for different times. A part of the uncovered area in (d) was shielded during the coating process by the sample holder. None of these mixtures show comparable results to pure NaOH.	54
4.9	External ICP-OES calibrations for Al, Cr, Co and W.	56
4.10	Metal concentrations in NaOH baths after 20 min de-coating time. 3 Samples are depicted: 737 is a purely metallic coating (70/30 Al/Cr ratio), 738 is a pure 90/10 coating, 740 is a sample with metallic interlayer and insoluble coating above.	57
4.11	BSE images showing the influence of two different corundum particle size classes, "Fine" = 36-106 µm, "Coarse" = 300-425 µm, on de-coating speed.	58
4.12	BSE images showing a comparison of metallic interlayer thicknesses regarding de-coating speed. The columns show the samples (20-60 s Ar atmosphere), the rows different bath times in 50 % NaOH. The optimal sample treated for 45 s in Ar atmosphere possesses an interlayer thickness of ≈50 nm.	59
4.13	BSE images showing a comparison of hexagonal interlayer thicknesses regarding de-coating speed. The columns show the samples (90/10 cathode evaporated for 1-5 min), the rows different bath times in 50 % NaOH. The optimal sample created by evaporating a 90/10 cathode for 3 min possesses an interlayer thickness of ≈70 nm.	60
4.14	BSE images of samples with metallic interlayer after treatment in acid at the given temperature and time and subsequently in NaOH at 140 °C for 20 min. Samples (c)-(f) are completely de-coated.	62
4.15	SE and light microscopic images of uncoated samples after long-term acid treatment at 90 °C. (b) and (d) show no significant changes on the surface, (c) has oxidized considerably.	63
4.16	(a) The ICP-OES analysis of HCl after 3 h at 90 °C shows mainly dissolved Co. Because of poor matrix matching with the standards larger error margins have to be considered. (b) The color of the same HCl and H ₂ SO ₄ after 3 h at 90 °C match corresponding Co complexes.	63
4.17	BSE images of three different sample types after 4 h reaction time in 50 % NaOH at 110 °C. The metallic and hexagonal interfaces exhibit vastly superior de-coating speed compared to sandblasting the cathode.	64
4.18	BSE images of samples with metallic and hexagonal interlayer after 2 min treatment in either HCl or H ₂ SO ₄ at 90 °C followed by 3 h in 50 % NaOH at 90 °C.	65

List of Tables

3.1	Used Chemicals	37
3.2	Sample list created by cathodic arc evaporation. The Al/Cr ratio, bias voltage, use of sandblasting (fine/coarse sand) and gas atmospheres were varied. Sand particle size classes are: "Fine" = 36-106 μm , "Coarse" = 300-425 μm . Samples with an entry in the column "Time" were first coated with the alternative gas in the list before switching to 1000 sccm N_2 for the rest of the coating procedure. Samples without time entry were coated for the entire duration with the listed gas and concentration.	38
3.3	List of used OES parameters.	41
3.4	List of used OES Standards.	41
4.1	Quantitative XPS results.	49
4.2	Quantitative OES results for selected samples after 20 min de-coating time in NaOH. Sample 737 is a purely metallic coating (70/30 Al/Cr ratio), 738 is a pure 90/10 coating, 740 is a sample with metallic interlayer and insoluble coating above. All concentrations are given in ppm (mg/L). . .	55

Eidesstattliche Erklärung

Hiermit erkläre ich, dass die vorliegende Arbeit gemäß dem Code of Conduct – Regeln zur Sicherung guter wissenschaftlicher Praxis (in der aktuellen Fassung des jeweiligen Mitteilungsblattes der TU Wien), insbesondere ohne unzulässige Hilfe Dritter und ohne Benutzung anderer als der angegebenen Hilfsmittel, angefertigt wurde. Die aus anderen Quellen direkt oder indirekt übernommenen Daten und Konzepte sind unter Angabe der Quelle gekennzeichnet. Die Arbeit wurde bisher weder im In- noch im Ausland in gleicher oder in ähnlicher Form in anderen Prüfungsverfahren vorgelegt.

Wien, 31. Juli 2018

Andreas Kretschmer